# HEATSTORE
# Benchmarking and improving models of subsurface heat storage dynamics

Prepared by: Peter Alt-Epping (ed.), University of Bern
Julian Mindel (ed.), ETH Zürich

With contributions from
Virginie Hamm, BRGM
Nicolas Marty, BRGM
Antoine Armandine, BRGM
Charles Maragna, BRGM
Charlotte Rey, Storengy
Marc Perreaux, Storengy
Ruben Vidal, UPC
Maarten Saaltink, UPC
Sebastia Olivella, UPC
Stijn Beernink, KWR
M. Bloemendal, KWR
N. Hartog, KWR
Martin Saar, ETHZ
Daniel Birdsell, ETHZ
Daniela Van den Heuvel, University of Bern
Carsten M. Nielsen, GEUS

Checked by: Thomas Driesner, ETHZ, WP2 lead

Approved by: Holger Cremer, TNO, HEATSTORE coordinator

Please cite this report as: Alt-Epping, P. & Mindel, J., (eds.) 2020: Benchmarking and improving models of subsurface heat storage dynamics, GEOTHERMICA – ERA NET Cofund Geothermal, 104 pp.

This report represents HEATSTORE project deliverable number D2.3

HEATSTORE (170153-4401) is one of nine projects under the GEOTHERMICA – ERA NET Cofund aimed at accelerating the uptake of geothermal energy by 1) advancing and integrating different types of underground thermal energy storage (UTES) in the energy system, 2) providing a means to maximise geothermal heat production and optimise the business case of geothermal heat production doublets, 3) addressing technical, economic, environmental, regulatory and policy aspects that are necessary to support efficient and cost-effective deployment of UTES technologies in Europe.

This project has been subsidized through the ERANET cofund GEOTHERMICA (Project n. 731117), from the European Commission, RVO (the Netherlands), DETEC (Switzerland), FZJ-PtJ (Germany), ADEME (France), EUDP (Denmark), Rannis (Iceland), VEA (Belgium), FRCT (Portugal), and MINECO (Spain).

# About HEATSTORE

**High Temperature Underground Thermal Energy Storage**

The heating and cooling sector is vitally important for the transition to a low-carbon and sustainable energy system. Heating and cooling is responsible for half of all consumed final energy in Europe. The vast majority – 85% - of the demand is fulfilled by fossil fuels, most notably natural gas. Low carbon heat sources (e.g. geothermal, biomass, solar and waste-heat) need to be deployed and heat storage plays a pivotal role in this development. Storage provides the flexibility to manage the variations in supply and demand of heat at different scales, but especially the seasonal dips and peaks in heat demand. Underground Thermal Energy Storage (UTES) technologies need to be further developed and need to become an integral component in the future energy system infrastructure to meet variations in both the availability and demand of energy.

The main objectives of the HEATSTORE project are to lower the cost, reduce risks, improve the performance of high temperature (~25°C to ~90°C) underground thermal energy storage (HT-UTES) technologies and to optimize heat network demand side management (DSM). This is primarily achieved by 6 new demonstration pilots and 8 case studies of existing systems with distinct configurations of heat sources, heat storage and heat utilization. This will advance the commercial viability of HT-UTES technologies and, through an optimized balance between supply, transport, storage and demand, enable that geothermal energy production can reach its maximum deployment potential in the European energy transition.

Furthermore, HEATSTORE also learns from existing UTES facilities and geothermal pilot sites from which the design, operating and monitoring information will be made available to the project by consortium partners.

HEATSTORE is one of nine projects under the GEOTHERMICA – ERA NET Cofund and has the objective of accelerating the uptake of geothermal energy by 1) advancing and integrating different types of underground thermal energy storage (UTES) in the energy system, 2) providing a means to maximize geothermal heat production and optimize the business case of geothermal heat production doublets, 3) addressing technical, economic, environmental, regulatory and policy aspects that are necessary to support efficient and cost-effective deployment of UTES technologies in Europe. The three-year project will stimulate a fast-track market uptake in Europe, promoting development from demonstration phase to commercial deployment within 2 to 5 years, and provide an outlook for utilization potential towards 2030 and 2050.

The 23 contributing partners from 9 countries in HEATSTORE have complementary expertise and roles. The consortium is composed of a mix of scientific research institutes and private companies. The industrial participation is considered a very strong and relevant advantage which is instrumental for success. The combination of leading European research institutes together with small, medium and large industrial enterprises, will ensure that the tested technologies can be brought to market and valorised by the relevant stakeholders.

# Document Change Record

This section shows the historical versions, with a short description of the updates.

| Version | Short description of change |
|---|---|
| 2020.05.31 | First version |
| 2020.06.08 | Final version (formatted) |

# Table of Content

# 1 Introduction

To assess the feasibility and the environmental impact of geotechnical operations for systems such as UTES/ATES, numerical modelling plays an important role. Numerical modelling allows the making of predictions about processes that are rarely accessible to direct observation, well ahead of a project realization. Planners can use simulations to assess the implications of “what-if” scenarios, evaluate risks, and explore the sensitivity of a system to changes in parameters, boundary conditions, and initial conditions.

Any perturbation of an equilibrium state in a subsurface environment sets in motion different processes that feedback on each other. For instance, the operation of a UTES/ATES perturbs the local groundwater flow system and the thermal regime at depth. This in turn induces geochemical disequilibrium as the circulating water changes temperature and pressure and transports dissolved chemical compounds, altering the local fluid composition. Mineral dissolution or precipitation reactions may follow which affect the porosity and permeability of the aquifer and hence its storativity or injectivity. It may also lead to mineral scaling or corrosion within installations. Similarly, the mechanical properties of the aquifer rock may change in response to temperature, pressure and chemical changes potentially affecting the integrity of the system. To assess the implications of a subsurface perturbation, all relevant physico-chemical processes and couplings between them have to be included in numerical simulations of a system.

The most basic coupling in simulations of geothermal systems is that between fluid flow and heat transport. Temperature and pressure affect the density and viscosity of water. Changes in temperature or pressure following a perturbation at depth can induce buoyancy and impact on the mobility of water. Groundwater flow itself is an important heat transport mechanism and can significantly perturb an otherwise conductive temperature regime, as can be seen in many regional groundwater systems (Lachenbruch and Sass (1977)). In systems with a magmatic heat source, it may even completely dominate heat transport.

The earliest thermal-hydraulic “TH” simulators, coupling fluid flow and heat transport date back to the early 1980’s (e.g. Smith and Chapman, 1983). The code HYDROTHERM, the first simulator of liquid- and vapour dominated hydrothermal systems, was developed by Sorey and Ingebritsen (1983) around the same time. HYDROTHERM is still a popular research code and now exists as Version 3.

About ten years later, in the early 1990’s, the first reactive transport codes were developed. Reactive transport codes couple “TH” processes with solute transport and chemical reactions “C”. At that time, several stand-alone batch geochemical simulators existed (e.g. MINTEQ, PHREEQE, EQ3/6). EQ3/6 in particular was later adopted as the “geochemical solver” in reactive transport codes such as ToughReact or OS3D/GIMRT (later Crunch). The motivation for constructing THC models was the fact that many geochemical processes in the subsurface are driven by solute transport. Groundwater carrying dissolved species may be driven across compositional boundaries in the rock, inducing disequilibrium reactions at the boundaries. Groundwater may move along preferential flowpaths, thereby undergoing temperature and pressure changes, leading to mineral precipitation reactions.

The needs of research projects spawned numerous code development initiatives, which in some cases have been ongoing for many years. For instance, one important driver for the development of early THC codes in terms of setting research needs and providing funding was the search for disposal sites for radioactive waste. The code development, consisting of the successive implementation of a specific process model, equation of state or a constitutive relationship, was therefore often linked to a specific research project.

Some codes used in this benchmark project, such as PHREEQC, CSMP, or TOUGH, have a legacy of decades of development. These legacy codes have sometimes been re-engineered, in some cases from the ground up, to keep up with the development of modern computational architectures (e.g. distributed memory parallel systems), programming or numerical methods.

The coupling of “C”, “M” and in few cases of “CM” with “TH” codes was in some instances achieved by running two existing codes in sequence, using an operator splitting approach. Other “fully coupled” codes with native “C” or “M” capabilities typically required a development from scratch. There are advantages and disadvantages to each of these approaches. Coupling existing, well established codes enable the use of the full range of capabilities of each code and, because these codes have been thoroughly tested, the resulting approach is less prone to errors or bugs. In addition, well established codes tend to have a broad user

community such that problem solving is relatively easy. One disadvantage of sequential coupling in THC codes is that there are limits as to the size of the allowable time step, which in turn affects performance. In some cases it may even be impossible to simulate geological time scales. In contrast, fully coupled codes are more flexible in their numerical solution scheme and tend to show better performance. However, these codes tend to be more limited in their capabilities and (partly because of this) in the size of the user community. Tracking down issues in these situations tends to be more tedious.

The purpose of Task2.3 within the HEATSTORE framework was to design a suite of generic benchmark simulation problems to demonstrate that the modelling tools used by the HEATSTORE partners have comparable capabilities and produce comparable results. A general agreement of results from different simulators greatly increases confidence in the simulations and associated predictions. In addition, discrepancies between the results from different codes provide an indication of the uncertainty that is to be expected when numerical output is evaluated. It must be noted that in most benchmarks presented, and unless there was an obvious input or output error, no particular effort was made to track down and correct the precise reason for discrepancies, or motivate code modification that may have improved the agreement or results with other simulators. In most cases, the default version of a simulator was used.

A total of three benchmarks were proposed and are described in this report, consisting of two TH-focused benchmarks and one THC-focused benchmark (Table 1-1). The first TH benchmark (TH1) was proposed by ETH Zürich, and was assimilated by all teams participating in Task 2.3. The proposal consists of a broad range of “TH” test problems, including an analytical transient pressure test, a complex well-testing model test, an experimental heat transport validation test, and a convection test.

**Table 1-1: Overview of all teams participating in Task 2.3 and their simulators. A description of the simulators is presented in sections 2 to 4 of this report.**

| TEAM | CODE | Benchmark | | |
|---|---|---|---|---|
| | | TH1 | TH2 | THC |
| **BRGM (France)** | COMSOL v4.2a | x | | |
| | COMPASS | x | | |
| | MARTHE | x | x | |
| | MARTHE-PHREEQC | | | x |
| **KWR (Holland)** | SEAWAT v4 | x | | |
| **UPC (Spain)** | CodeBright | x | | |
| | RETRASO | | | x |
| **Storengy (France)** | TOUGH3 | x | x | |
| **University of Bern (Switzerland)** | PFLOTRAN | x | | x |
| **GEUS (Denmark)** | ECLIPSE 100 | x | | |
| **ETHZ (Switzerland)** | NEXUS-CSMP++ | x | | |
| | MOOSE | x | | |

The second TH benchmark (TH2), proposed by BRGM, is a joint effort between BRGM and Storengy. The benchmark is part of the GEOSTOCAL research project that assesses the feasibility of a seasonal heat storage system in the Dogger limestone aquifer in the commune of Ivry-sur-Seine (South-East of Paris).

The THC benchmark was proposed by the University of Bern, and is based on the planned HT-ATES at Forsthaus in Bern, Switzerland. In consists of a suite of component benchmarks of increasing complexity. The simulations are aimed at being simple yet representative enough to provide useful insights into different geochemical aspects of the system.

A total of seven teams from five difrerent countries participated in this benchmark project, using 12 different simulation codes (Table 1-1).

# 2 TH Benchmark 1 (proposed by Julian Mindel, ETHZ)

The testing concept presented in this benchmark focuses on a main problem-set that is meant to express important capabilities available in TH simulators. In the context of verification, results from a particular simulator should be compared to results from known analytical, empirical, and analytical-empirical solutions, as well as results produced by other simulators. At least within TH modelling, this should ultimately establish a point of reference in terms of capabilities and accuracy. We present an analytical transient pressure test (test1), a complex well-testing model test (test2), an experimental heat transport validation test (test3), and a convection test (test4), with the aim to establish such a benchmark. For each test within this benchmark, we present a sequence of description, specification, data formatting, and results.

## 2.1 Participating simulators

A total of 7 partners participated in this benchmark, with 10 simulators in total. The tests were carried out by each partner, as summarized in Table 2-1. At the time of drafting this report, not all partners had been able to perform all associated tests due to a variety of circumstances. Comments and reasons for incomplete and not-submitted results are briefly described in Table 2-1, and throughout section 2.

**Table 2-1: Status of benchmark test completion per simulator.**

| | | | Status | | | |
|---|---|---|---|---|---|---|
| **Participant** | **Simulator** | **% Complete** | **test1** | **test2** | **test3** | **test4** |
| BRGM | COMSOL v4.2a | 63 | complete | incomplete[2] | incomplete[6] | not submitted[8] |
| | MARTHE | 96 | complete | incomplete[3] | complete | complete |
| | COMPASS | 100 | complete | complete | complete | complete |
| ETHZ | Nexus-CSMP++ | 100 | complete | complete | complete | complete |
| | MOOSE | 100 | complete | complete | complete | complete |
| KWR | SEAWATv4 | 96 | complete | incomplete[3] | complete | complete |
| UPC | CODE_BRIGHT | 100 | complete | complete | complete | complete |
| STY | Tough3 | 83 | complete | incomplete[3] | complete[7] | complete |
| UniBe | PFLOTRAN | 92 | complete | incomplete[4] | complete | complete |
| GEUS | Eclipse 100 | 45 | incomplete[1] | incomplete[5] | incomplete[6] | not submitted [9] |

[1] PROBE_1 and PROBE_2 data is missing.

[2] Cartesian mesh results missing.

[3] Variant 3, radial mesh results missing.

[4] Complete variant 3 case is missing.

[5] Radial meshes cannot be constructed.

[6] Inaccurate input was used.

[7] Observed a major delay in transport in comparison to other simulators. Reason not found.

[8] COMSOL was, reportedly, unable to converge for all of the simulations required.

[9] Eclipse 100 is reportedly unable to represent the problem due to its formulation.

The participating simulators, whether commercial or strictly research oriented, are well known and have a significant level of published positive notoriety. Each one possesses different characteristics stemming from its core formulation, algorithmic implementation, programming, and other peripheral capabilities such as the ability to model fractures and wells. Individual simulator descriptions were provided by the participants, and also researched online with various levels of success. The characteristics are summarized to their basics in Table 2-2.

**Table 2-2: Simulator time and space discretization approach (basic), and primary implementation programming language.**

| Simulator | Language | Time Disc. Meth. | Spat. Disc. Meth. |
|---|---|---|---|
| COMSOL v4.2a | NA | SD | FE |
| MARTHE | Fortran | EI | FV |
| COMPASS | Fortran | EI | FV |
| Nexus-CSMP++ | C++ | PE | Hybrid FE-FV |
| MOOSE | C++ | EI | FE |
| SEAWATv4 | Fortran | SD | FD |
| CODE_BRIGHT | Fortran | EI | FE |
| Tough3 | Fortran | EI | IFD |
| PFLOTRAN | Fortran | EI | FV |
| Eclipse 100 | NA | EI | FD |

SD = Solver Depedent
EI = Euler Implicit
PE = Pseudo Explicit
NA = Information Not Available
FD = Finite Differences
IFD = Integrated Finite Differences
FV = Finite Volumes
FE = Finite Elements

## 2.2 Data organization

One of the main challenges within a benchmark across many simulators of different origin is the comparison of data. Methods, formats, and other individual characteristics may provide a challenge in terms of organization. It is therefore important to establish a standard for information exchange within this context. This sub-section describes the format used for the provided input data as well as the result data returned by each participant.

### 2.2.1 Test Input Data

Data is provided together with this report, to allow for consistent testing across simulators. The input folder contains necessary input data files and examples, and its organization is explained by the following list structure:

- **input/** (main base folder, 4 sub-folders, 4 sub-sub folders, 12 files)
  - **test1/**
    - test1_analytical_solution.txt
    - **examples/**
      - test1_EXAMPLE.txt
  - **test2/**
    - **examples/**
      - test2_IFDB_EXAMPLE.txt
  - **test3/**
    - glass_1615_Z0.txt
    - glass_1615_Z11.txt
    - glass_1615_Z22.txt
    - steel_2190_Z0.txt
    - steel_2190_Z5.txt
    - steel_2190_Z10.txt
    - **examples/**
      - test3_Glass_EXAMPLE.txt
  - **test4/**
    - **examples/**
      - test4_temperature_highperm_coarse_EXAMPLE_1000.jpg
      - test4_streamlines_highperm_coarse_EXAMPLE_1000.jpg

Names ending in "/" imply names of folders. The content of all provided files is further explained in each corresponding test section.

### 2.2.2 Standardized Output Data

The data used for analysis and to construct the plots presented in the different result sections of this benchmark are compiled as a general compressed file (*.zip). Within this file, data is divided on a per-simulator basis bundle. These bundles consist of data provided by each participant also compressed in a zip file "`TH_BM_results_NAME.zip`" that follows an internal structure to aid data access for plots and related comparison analysis.

The structure to be followed begins at a single base folder, and all folder and file names should be in lower case letters, with the exception of "NAME", which should be substituted by the unique person/institution (e.g. `JulianMindel_ETHZ`). The exact number of expected result files, formats, and structure that should be followed, with file names mentioned in each the test descriptions, is detailed in the following list:

- **results_NAME/** (main base folder, 4 subfolders, 50 files )
  - **test1/** (3 files)
    - test1_sys_application_info_NAME.txt
    - test1_coarse_NAME.txt
    - test1_fine_NAME.txt
  - **test2/** (7 files)
    - test2_sys_application_info_NAME.txt
    - test2_radial_NAME_variant1.txt
    - test2_radial_NAME_variant2.txt
    - test2_radial_NAME_variant3.txt
    - test2_cartesian_NAME_variant1.txt
    - test2_cartesian_NAME_variant2.txt
    - test2_cartesian_NAME_variant3.txt
  - **test3/** (3 files)
    - test3_sys_application_info_NAME.txt
    - test3_Glass_NAME.txt
    - test3_Steel_NAME.txt
  - **test4/** (37 files)
    - test4_sys_application_info_NAME.txt
    - test4_temperature_lowperm_coarse_NAME_10.jpg
    - test4_temperature_medperm_coarse_NAME_10.jpg
    - test4_temperature_highperm_coarse_NAME_10.jpg
    - test4_streamlines_lowperm_coarse_NAME_10.jpg
    - test4_streamlines_medperm_coarse_NAME_10.jpg
    - test4_streamlines_highperm_coarse_NAME_10.jpg
    - test4_temperature_lowperm_coarse_NAME_100.jpg
    - test4_temperature_medperm_coarse_NAME_100.jpg
    - test4_temperature_highperm_coarse_NAME_100.jpg
    - test4_streamlines_lowperm_coarse_NAME_100.jpg
    - test4_streamlines_medperm_coarse_NAME_100.jpg
    - test4_streamlines_highperm_coarse_NAME_100.jpg
    - test4_temperature_lowperm_coarse_NAME_1000.jpg
    - test4_temperature_medperm_coarse_NAME_1000.jpg
    - test4_temperature_highperm_coarse_NAME_1000.jpg
    - test4_streamlines_lowperm_coarse_NAME_1000.jpg
    - test4_streamlines_medperm_coarse_NAME_1000.jpg
    - test4_streamlines_highperm_coarse_NAME_1000.jpg
    - test4_temperature_lowperm_fine_NAME_10.jpg
    - test4_temperature_medperm_fine_NAME_10.jpg
    - test4_temperature_highperm_fine_NAME_10.jpg

- test4_streamlines_lowperm_fine_NAME_10.jpg
- test4_streamlines_medperm_fine_NAME_10.jpg
- test4_streamlines_highperm_fine_NAME_10.jpg
- test4_temperature_lowperm_fine_NAME_100.jpg
- test4_temperature_medperm_fine_NAME_100.jpg
- test4_temperature_highperm_fine_NAME_100.jpg
- test4_streamlines_lowperm_fine_NAME_100.jpg
- test4_streamlines_medperm_fine_NAME_100.jpg
- test4_streamlines_highperm_fine_NAME_100.jpg
- test4_temperature_lowperm_fine_NAME_1000.jpg
- test4_temperature_medperm_fine_NAME_1000.jpg
- test4_temperature_highperm_fine_NAME_1000.jpg
- test4_streamlines_lowperm_fine_NAME_1000.jpg
- test4_streamlines_medperm_fine_NAME_1000.jpg
- test4_streamlines_highperm_fine_NAME_1000.jpg

## 2.3 Test1: Analytical transient pressure verification test

This problem set is related to the practice of well testing (i.e. pressure transient testing, PTT, or pressure transient analysis, PTA). Accepting certain simplifying assumptions, this test idealizes an otherwise homogeneous reservoir geometry, and focuses on reproducing a characteristic pressure response of a reservoir subjected to a constant volumetric flow rate injection. It is aimed at quantifying accuracy across different simulators that may possess a variety of discretization formulations (e.g. Finite Difference, Finite Volumes, Finite Elements, and many others, including combinations) and to measure "H" capabilities of the available TH models.

### 2.3.1 Problem Description

This analytical solution is well known (see for example (Philips, 1969) (Pullan, 1990) (Basha, 1999) (Chen, 2007) ), and can be conveniently expressed in cylindrical coordinates. The idealized problem geometry consists of an infinitely wide cylindrical reservoir domain of thickness $h$, as shown in Figure 2-1. Given the assumption of reservoir material homogeneity and the absence of gravitational effects, it is possible to simulate this problem completely with one dimension (i.e. radial).

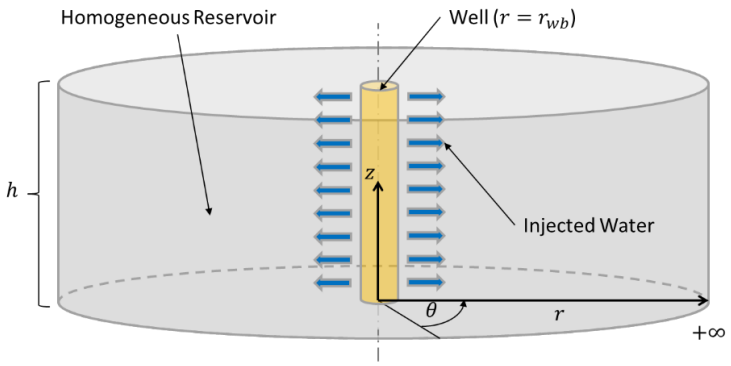


**Figure 2-1: Idealized cylindrical domain used to obtain the transient pressure analytical solution.**

Assuming that no flow is possible through the top or bottom boundaries, and that a well is placed in the center of the cylindrical reservoir domain, a constant amount of fluid is being pumped at a constant uniformly distributed rate[1] $Q\left[\frac{m^3}{s}\right]$ through the well of completion length $h$ (i.e. encompassing the entire reservoir thickness), and radius $r_{wb}[m]$. We can thus express the flow velocity $u_{wb}$ at the wellbore cylindrical face as,

[1] For the purposes of this test, $Q$ is assumed positive for injection, and negative for production.

$$u_{wb}\left[\frac{m}{s}\right] = -\frac{k}{\mu_f}\frac{dp}{dr} = \frac{Q}{2\pi r_{wb} h} \tag{2-1}$$

where $k$ is the assumed isotropic permeability, $p$ is the fluid pressure, and $\mu_f$ is the fluid viscosity. Assuming the reservoir domain is a homogeneous non-deformable porous medium, we can state the Cartesian coordinate-based *porous, isothermal, single-phase, slightly compressible, continuum formulation* for fluid flow (i.e. of pure water) in such a context as,

$$\phi\beta_f \frac{\partial p}{\partial t} - \nabla \cdot \left(\frac{k}{\mu_f}(\nabla p - \rho_f \mathbf{g})\right) = 0 \tag{2-2}$$

where $\phi$ is the rock porosity, $\rho_f$ is the fluid density, $\beta_f$ is the fluid compressibility, and $\mathbf{g}$ is the gravitational vector. In cylindrical coordinates $(r, \theta, z)$ and without the loss of generality (i.e. within the assumptions), equation (2-2) can be re-written as,

$$\phi\beta_f \frac{\partial p}{\partial t} - \frac{1}{r}\frac{\partial}{\partial r}\left\{r\frac{k}{\mu_f}\left(\frac{\partial p}{\partial r} - \rho_f \mathbf{g}\right)\right\} - \frac{1}{r^2}\frac{\partial}{\partial \theta}\left\{\frac{k}{\mu_f}\left(\frac{\partial p}{\partial \theta} - \rho_f \mathbf{g}\right)\right\} - \frac{\partial}{\partial z}\left\{\frac{k}{\mu_f}\left(\frac{\partial p}{\partial z} - \rho_f \mathbf{g}\right)\right\} = 0 \tag{2-3}$$

Neglecting gravitational effects and focusing on an arbitrary reservoir depth at a uniformly constant $p_{res}$ while assuming symmetry about the $z$ axis, problems become unidimensional and are thus governed by,

$$\frac{1}{\kappa}\frac{\partial p}{\partial t} - \frac{1}{r}\frac{\partial}{\partial r}\left\{r\frac{\partial p}{\partial r}\right\} = 0 \;\; where\; \kappa = \frac{k}{\mu_f \beta_f \phi} \tag{2-4}$$

where $\kappa$ is typically known as the pressure diffusivity. We can therefore group all the necessary equations to define our problem,

| | | | |
|---|---|---|---|
| Governing Equation | $\frac{1}{\kappa}\frac{\partial p}{\partial t} - \frac{1}{r}\frac{\partial p}{\partial r} - \frac{\partial^2 p}{\partial r^2} = 0$ | $where\ 0 < r_{wb} \leq r$ | (2-5) |
| Boundary Condition | $\frac{\partial p}{\partial r}(r_{wb}, t) = -\frac{Q\mu_f}{2\pi r_{wb} hk}$ | $where\ r = r_{wb}, for\ all\ t$ | (2-6) |
| Boundary Condition | $p(\infty, t) = p_{res}$ | $where\ r = +\infty, for\ all\ t$ | (2-7) |
| Initial Condition | $p(r, t_0) = p_{res}$ | $where\ t = t_0,\ for\ all\ r$ | (2-8) |

where we have obtained the Neumann boundary condition (2-6) from equation (2-1). Note that while a pressure solution will be undefined for $r = 0$, it will be defined for $r > 0$.

Using a method known as the *Boltzmann change of variable*, equation (2-5) may be solved analytically (Chen, 2007) while honouring the initial and boundary conditions (2-6)-(2-8), to obtain,

$$p(r, t) = p_{res} - \frac{Q\mu_f}{4\pi hk} Ei\left(-\frac{r^2}{4t\kappa}\right) \tag{2-9}$$

where $Ei$ is known as the exponential integral function which can be expressed as,

$$Ei(-\eta) = \int_{\infty}^{\eta} \frac{e^{-\eta'}}{\eta'} d\eta' = -\int_{\eta}^{\infty} \frac{e^{-\eta'}}{\eta'} d\eta' \qquad where\ \eta = \frac{r^2}{4t\kappa}, our\ Boltzmann\ variable \tag{2-10}$$

valid for all real values of $\eta$. Reproducing equation (2-9) as accurately as possible should be the main goal of this particular test. It should be noted that for the assumptions leading to this equation to remain formally valid while a constant volumetric flow rate is being applied, viscosity $\mu_f$, and fluid compressibility $\beta_f$ must also be assumed/considered constant.

### 2.3.2 Simulation Description

Given the variety of formulations that may be available throughout the range of tested applications, it is expected that simulators are able to reproduce the analytical solution (2-9) while working with all their available dimensional configurations (e.g. Cartesian coordinates, cylindrical coordinates, 3D, 2D axisymmetric, 1D, etc.). At a minimum, dimensional settings used should correspond to those applied in the work to be carried out within HEATSTORE WP2.

Whenever possible, simulators should attempt to use the meshes that are provided together with this report[2]. Considering that in some cases, direct use of these meshes might not be possible due to certain differences or limitations in modelling approaches (e.g. no lower dimensional element capability for the well region, use of regular meshes), or formats, each simulation tool should then produce an adequate yet similar set of meshes in terms of number of mesh cells and points, and overall resolution distribution (e.g. minimum and maximum element sizes). Information about the mesh should be provided as expressed in the output specification.

Honouring the assumptions described in section 2.3.1 all simulations run for this test should have the following basic characteristics,

1. Cylindrical[3] geometrical domain of radius $r_{max} = 2400\ [m]$, and height $h = 200[m]$.
2. A well[4] in the center of the cylindrical domain, of completion length $h$.
3. Single phase, isothermal, slightly compressible, flow through porous media. Constant $\mu_f$ and $\beta_f$.
4. Gravitational effects are neglected.
5. Fluid pressure values are measured at $0.1$, $1$, $10$, $100$, and $1000\ [m]$ away from the well, at the following times: $0.1$, $1$, $10$, $10^2$, $10^3$, … , $10^8\ [s]$ (i.e. the latter value is equivalent to approximately $3$ years)

Simulations should be run with two meshes, a coarse one, and a refined one (see Figure 2-2) and fluid pressure values should be measured at the prescribed locations and times (see Table 2-4). The relative error with respect to the analytical solution (expressed in evaluated fractions, not percentiles) should also be provided. It is expected that the simulations run with the refined mesh provide better results in terms of error with respect to the analytical solution (i.e. mesh convergence).

In terms of *boundary conditions*, the top and bottom boundaries should be set to no-flow (i.e. natural boundary conditions in FE, FV, and other integral-form methods, zero normal flow in other methods), while the cylindrical side boundary should be set to a Dirichlet type with a value of $p_{res}$, allowing mass to leave the domain through it. In the case of the well conditions (i.e. which could eventually be boundary conditions in methods using radial coordinates in 1D or 2D), and given that approaches to account for them may vary across simulators, a description of the strategy should be provided along with an explanation on how the volumetric flow rate $Q$ and equation (2-6) are being honoured by the formulation (see section “other comments”, in Table 2-6).
*Initial conditions* should be set to a constant $p_{res}$ throughout the computational domain. Injection at a constant volumetric flow rate $Q\left[\frac{m^3}{s}\right]$ should begin immediately and be maintained for the duration of the simulation $t_{end}$.

### 2.3.3 Detailed Problem Specification

Two different grids should be used for each simulation (see Figure 2-2), and both simulations should use the same assumptions and input parameters. Each simulation should provide the same kind of output, as specified in Section 2.3.4. Basic information about each grid provided with this report is presented in Table .

[2] Meshes will be provided in formats available to ANSYS ICEMCFD, upon request.
[3] If a cylindrical domain is not easily obtainable (e.g. a simulator is somehow limited to Cartesian grids) a prismatic domain may be constructed where the cylindrical test domain is inscribed.
[4] There are a variety of ways to simulate wells, none are prescribed here, as each formulation may allow for a different approach.

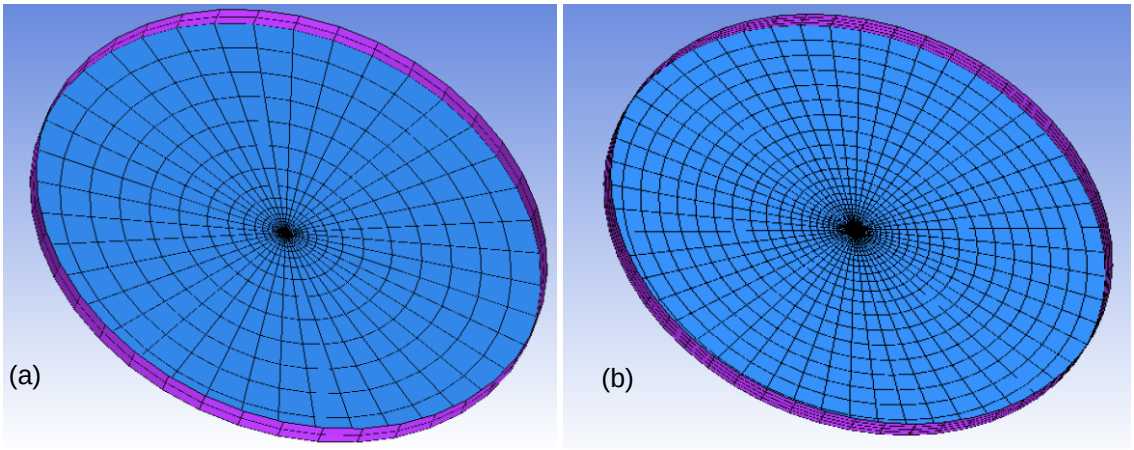


**Figure 2-2: Example of (a) a coarse grid and (b) a refined grid to be used for the analytical transient pressure comparison test.**

**Table 2-3: Mesh information summary for test1.**

| | Mesh 1 (Coarse) | | Mesh 2 (Refined) | |
|---|---|---|---|---|
| Total Number of Cells | 1568 | | 12992 | |
| Total Number of Points | 3138 | | 16125 | |
| Cell types | LINE_2, HEXA_8, TRI_3, PENTA_6, QUAD_4 | | LINE_2, HEXA_8, TRI_3, PENTA_6, QUAD_4 | |
| Maximum Cell Size (side $[m]$, volume $[m^3]$) | 367 | $1.82 \cdot 10^7$ | 270 | $2.26 \cdot 10^6$ |
| Minimum Cell Size (side $[m]$, volume $[m^3]$) | 0.11 | 11.19 | 0.011 | 0.03 |
| First cell next to well (radial length, $[m]$) | 1[5] | | 0.1 | |
| Radial subdivisions (slices) | 56 | | 56 | |
| Thickness subdivisions | 1 | | 3 | |
| Formats available | All output formats supported by Ansys ICEM CFD 17.2[6] | | | |

Details of the input parameters needed for the simulations are shown in Table 2-4.

[5] Given the location of the first observation point ($r = 0.1\ [m]$ ), values for this location must be interpolated.
[6] Meshes can be provided on request. For an updated list of formats available, please visit https://www.sharcnet.ca/Software/Ansys/17.2/en-us/help/icm_help/iout_solver.html

**Table 2-4: Simulation input specification.**

| Parameter | Value |
|---|---|
| **Permeability ( $k$ )** | $10^{-15}\ [m^2]$ |
| **Porosity ( $\phi$ )** | $0.2\ [-]$ |
| **Fluid density ( $\rho_f$ )**[7] | $994.75\ \left[\frac{Kg}{m^3}\right]$ |
| **Fluid viscosity ( $\mu_f$ )**[7] | $0.00074\ [Pa \cdot s]$ |
| **Fluid compressibility ( $\beta_f$ )**[7] | $4.45 \cdot 10^{-10}\ \left[\frac{1}{Pa}\right]$ |
| **Well volumetric flow rate ( $Q$ )** | $0.001\ \left[\frac{m^3}{s}\right]$ |
| **Wellbore radius ( $r_{wb}$ )** | $0.1\ [m]$ |
| **Simulation end time ( $t_{end}$ )** | $10^8\ [s]$ |
| **Radial pressure probe locations (five)** | $0.1, 1, 10, 100, 1000\ [m]$ |
| **Output times (ten)** | $0.1,\ 1,\ 10,\ 10^2,\ 10^3,\ \dots,\ 10^8\ [s]$ |
| **Domain radius ( $r_{max}$ )** | $2400\ [m]$ |
| **Domain height ( $h$ )** | $200\ [m]$ |
| **Initial pressure ( $p_{res}$ )** | $10^6\ [Pa]$ |
| **Outer boundary pressure ( $p_{res}$ at $r = r_{max}$ )** | $10^6\ [Pa]$ |

## 2.3.4 Output Specification

Both simulations should report a solution for fluid pressure at locations measured radially from the wellbore (see Table 2-4, "*Radial pressure probe locations*") as well as the relative error with respect to the analytical solution. The data should be reported via two ASCII[8] text files "`test1_coarse_NAME.txt`" and "`test1_fine_NAME.txt`", consisting of tab-delimited headers and values. NAME in the input file should be replaced with the full name of the author of the test result as well as the institution (e.g. "JulianMindel_ETHZ"). Values should be provided in scientific notation using at least twelve significant digits. A table of tab separated values from the evaluation of the analytical solution at the necessary locations and times is provided with this report as "`test1_analytical_solution.txt`". An example output files I provided also via "`test1_EXAMPLE.txt`", and should be used as a template for the output of this test (see Table 2-5). When calculating the relative error, values should be output in analogous order and to the right of the pressure values. There should be a total of 11 columns when including a *time* column.

[7] For simulators where setting fixed fluid properties proves problematic, values at $34\ ^{o}C$ and $10^6\ Pa$ should be used
[8] https://en.wikipedia.org/wiki/Text_file

**Table 2-5: Output format for pressure and relative error results (i.e. some columns of data have been purposely truncated from the able to aid visualization).**

| TIME | PROBE_1 | PROBE_2 | PROBE_3 | PROBE_4 | PROBE_5 | REL_ERROR1 | REL_ERROR2 | REL_ERROR3 | REL_ERROR4 | REL_ERROR5 |
|---|---|---|---|---|---|---|---|---|---|---|
| 1.000000000000e-01 | 1.005378563270e+06 | 1.000096899350e+06 | 1.000069927580e+06 | 1.000007809200e+06 | 1.000000001 |
| 1.000000000000e+00 | 1.045905307730e+06 | 1.000435860830e+06 | 1.000069927230e+06 | 1.000007809200e+06 | 1.000000001 |
| 1.000000000000e+01 | 1.349138201700e+06 | 1.020795947380e+06 | 1.000069922590e+06 | 1.000007809190e+06 | 1.000000001 |
| 1.000000000000e+02 | 2.210032465970e+06 | 1.279683507140e+06 | 1.000130876700e+06 | 1.000007809160e+06 | 1.000000001 |
| 1.000000000000e+03 | 3.029911357920e+06 | 1.883613856530e+06 | 1.029918825080e+06 | 1.000007808660e+06 | 1.000000001 |
| 1.000000000000e+04 | 3.723552542500e+06 | 2.556446846860e+06 | 1.329170303890e+06 | 1.000066101400e+06 | 1.000000001 |
| 1.000000000000e+05 | 4.446259219710e+06 | 3.277352863120e+06 | 1.959909430010e+06 | 1.027539996930e+06 | 1.000000001 |
| 1.000000000000e+06 | 5.171900549030e+06 | 4.002878405690e+06 | 2.678005909890e+06 | 1.387713178240e+06 | 1.000001318 |
| 1.000000000000e+07 | 5.846696445160e+06 | 4.677668853550e+06 | 3.352335902860e+06 | 2.018738389550e+06 | 1.021803946 |
| 1.000000000000e+08 | 6.510624146910e+06 | 5.341595417880e+06 | 4.016218589020e+06 | 2.678272646340e+06 | 1.380992251 |

Additionally, for reference purposes, information should be provided via a separate text file "`test1_sys_application_info_NAME.txt`" regarding the simulator, compiler, compiler version, operating system, the CPU used and memory available, parallel capabilities used (e.g. CUDA, MPI, OpenMP), and mesh information. The table format and sample information is provided in Table 2-6. Example files with the needed information are provided by "`test1_EXAMPLE.txt`" and "`test1_sys_application_info_EXAMPLE.txt`".

**Table 2-6: Output format for system and application information.**

```
simulator application name: nexus_thc_simulator
core language: C++
compiler name: GNU g++
compiler version: 7.3.0
operating system: Ubuntu Linux
CPU Name:  Intel(R) Xeon(R) CPU E5-2640 v3 @ 2.60GHz
max available physical memory: 128 GB
parallel capabilities (used):  OpenMP
mesh files used: cyclinder_coarse.asc cylinder_coarse.dat
mesh format: CSP format from Ansys ICEMCFD 17.2
mesh characteristics: unstructured
Total Number of Cells: 22035
Total Number of Points: 3923
Cell types  TETRA_4, TRI_3, LINE_2
Maximum Cell side [m]:437
Minimum Cell side [m]: 0.9
Maximum Cell volume [m^3]: 2.93e6
Minimum Cell volume [m^3]: 1.05
other comments: none
```

### 2.3.4.1 Notes on error calculation and evaluating the *Ei* function

Relative error should be calculated via:

$$\epsilon = \left| \frac{\left(p_{numerical} - p_{analytic}\right)}{p_{analytic}} \right| \tag{2-11}$$

Evaluating the exponential integral function in equation (2-9) accurately may prove a challenge (see (Tseng & Lee, 1998) ) unless certain pre-programmed tools are used (e.g. Maple, Matlab, etc.). Simplifications exist, such as

$$Ei(-\eta) \approx -Ln\left(\frac{0.5625}{\eta}\right) \tag{2-12}$$

however the approximation error remains low (i.e. $< 0.25\%$) if $\eta < 0.01$. Accuracy increases when measuring at distances further away from the well, and similarly with increasing simulated time, however it also depends on assumed fluid and reservoir characteristics. A Maple version of the code necessary to reproduce the analytical results is presented in section 7.1 Appendix A: TH Benchmark 1 - Analytical solution.

## 2.3.5 Results

With minor setbacks in terms of available sampling data for the Eclipse100 (GEUS) simulator, all other participants were able to reasonably reproduce the analytical solution, as can be seen through a sample of results in Figure 2-3, both within the coarse and fine mesh contexts. The full set of comparative results can be observed in section 7.3 named Appendix C: TH Benchmark 1 - Test 1 results.

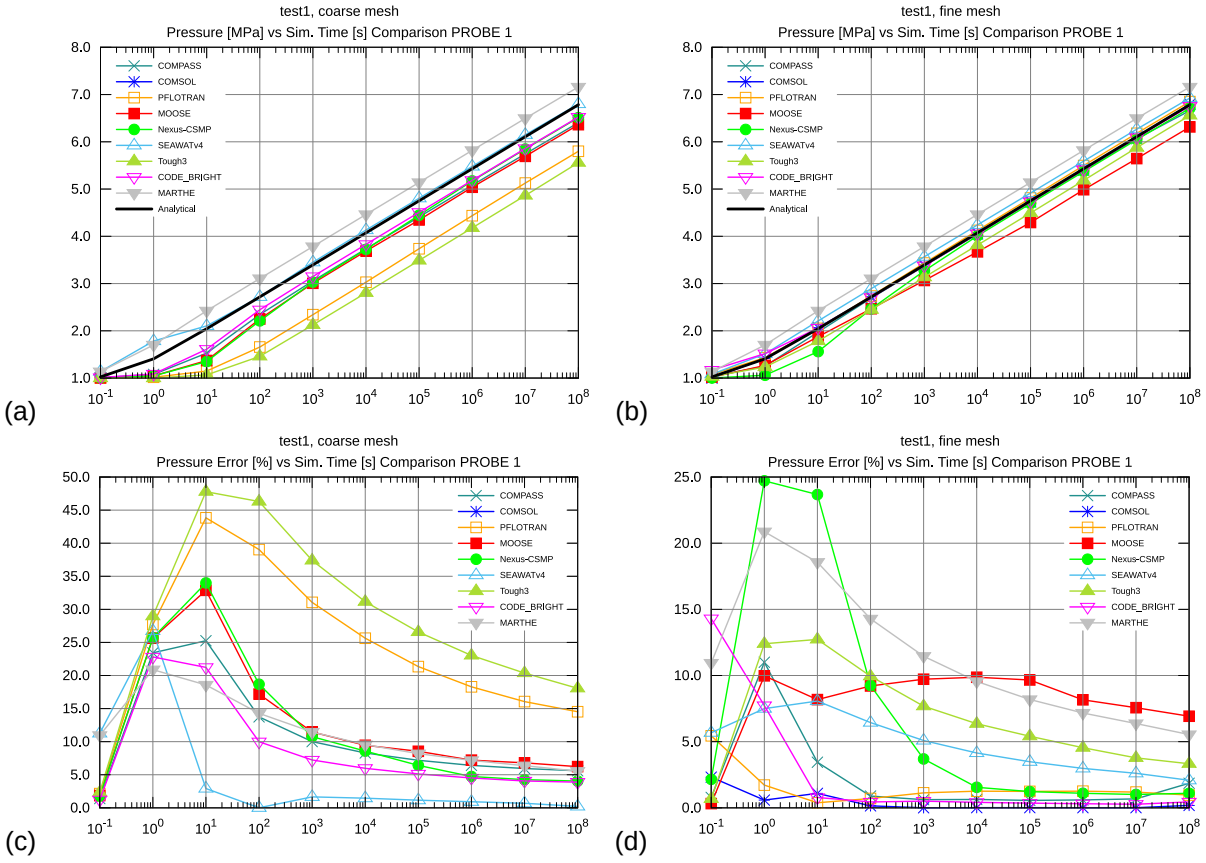


**Figure 2-3: Pressure [Mpa] and Pressure Error [%] evolution with time [s] comparison for the first probe point (PROBE_1), located at $r = 0.1[m]$ for test1.**

As can be observed from Figure 2-3(c) and (d), a major challenge is presented by the steep gradients present at the initial stages, at the well face. In the case of the Eclipse100 simulator, results for the coarse mesh were only available starting from PROBE_3 onwards, and for the fine mesh from PROBE_2 onwards. Analysing the full set of results presented by Figure C-1 in section 7.3 named Appendix C: TH Benchmark 1 - Test 1 results, highest levels (i.e. peaks) of error were presented by the Tough3 and PFLOTRAN simulators (~47%, ~43%) for the coarse mesh case, and by the Nexus-CSMP and MARTHE simulators (~25%, ~21%) for the fine mesh case. Error levels drop consistently and uniformly the further away a particular probe is from the injection point. PROBE_2 levels of error are dominated by Tough3, COMSOL, and SEAWATv4 for the coarse mesh, and by Eclipse100 (i.e. considerably, at ~48%), Tough3, and MOOSE for the fine mesh. In the cases of PROBE_3, PROBE_4, and PROBE_5, error levels for peaks are considerably lower (e.g. in the ranges ~12% - ~28%). A time delay of the onset of the maximum error is also observed, which depends on the location of the probe for all simulators. In PROBE_1, the error peak appears between 1 and 100 seconds of elapsed time for the coarse mesh case, and between 1 and 10 seconds for the fine mesh case. In contrast, the error peak at PROBE_8 appears at the end of the simulation ($t = 10^8$ $[s]$).

Eclipse100 must be signalled as a particular outlier for this test, as it was not possible to output results or interpolate them at the well face (i.e. PROBE_1) for both the coarse and fine meshes. PROBE_2 was only available for the fine mesh case, where results were particularly inaccurate with error values reported of ~48%.

Given the range of formulations, and implementations used by all simulators taking part in this particular test, a particular rationale may not easily be established solely based on the presented results. The modelling of sources and sinks tends to create a challenge for accuracy in some simulators, depending on their individual formulations and implementations. Furthermore, and in particular for commercial simulators or large open source projects, some options may not easily be available and could thus affect the optimal performance of a particular resulting application.

## 2.4 Test2: Injection-Falloff-Drawdown-Build-up well test

Well tests (e.g. Drawdown, Build-up, Injection, and Falloff) are typically run either experimentally or conveniently during operation on a drilled well to obtain and/or expand the amount of information known about a sub-surface reservoir (Slotte & Berg, 2017). The problem set described in this section is meant for simulators to reproduce typical well test responses and is aimed at comparing TH modelling characteristics and results across different simulators.

### 2.4.1 Problem Description

The problem involves utilizing the basic setup presented in Section 2.3 (test1) to perform, combined in a non-stop sequence, injection, falloff, drawdown, build-up well tests. In contrast to test1, we remove the isothermal flow restriction, the volumetric flow rate $Q\left[\frac{m^3}{s}\right]$ is varied at each stage to produce a response from the reservoir, as shown in Figure 2-6. The two main goals of the test problem are:

1. Comparing results across available simulators.
2. Analysing the test response to assess the sensitivity of simulators for capturing well response effects due to heterogeneities in the reservoir material properties.

There are three variants of this test,

1. Homogeneous reservoir.
2. With a “patch reef structure”, represented by a region of higher uniform permeability centered around the well, from $r = r_{wb}$ until $r = r_{reef}$ (see Figure 2-4)
3. With fracture at a distance from the well, $\boldsymbol{x = x_{frac}}$ (see Figure 2-5)

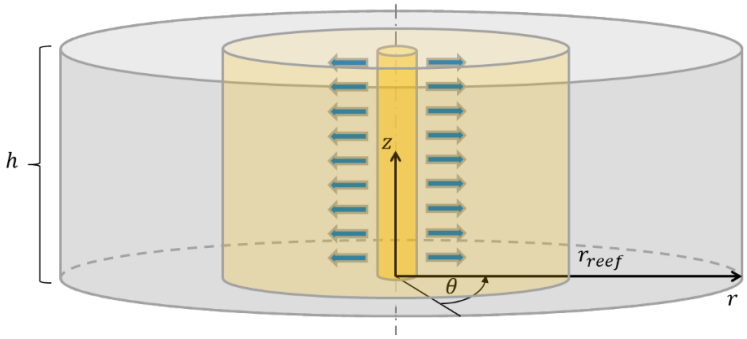


**Figure 2-4: Schematic of the “reef structure” included in an otherwise homogeneous reservoir.**

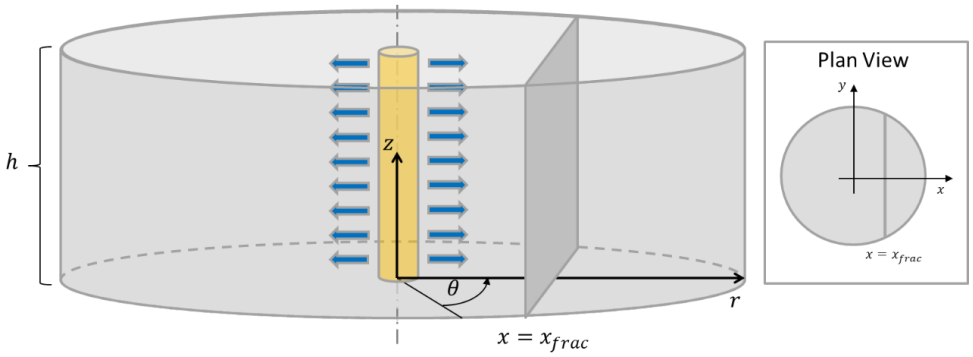


**Figure 2-5: Schematic of the fracture included in an otherwise homogeneous reservoir**

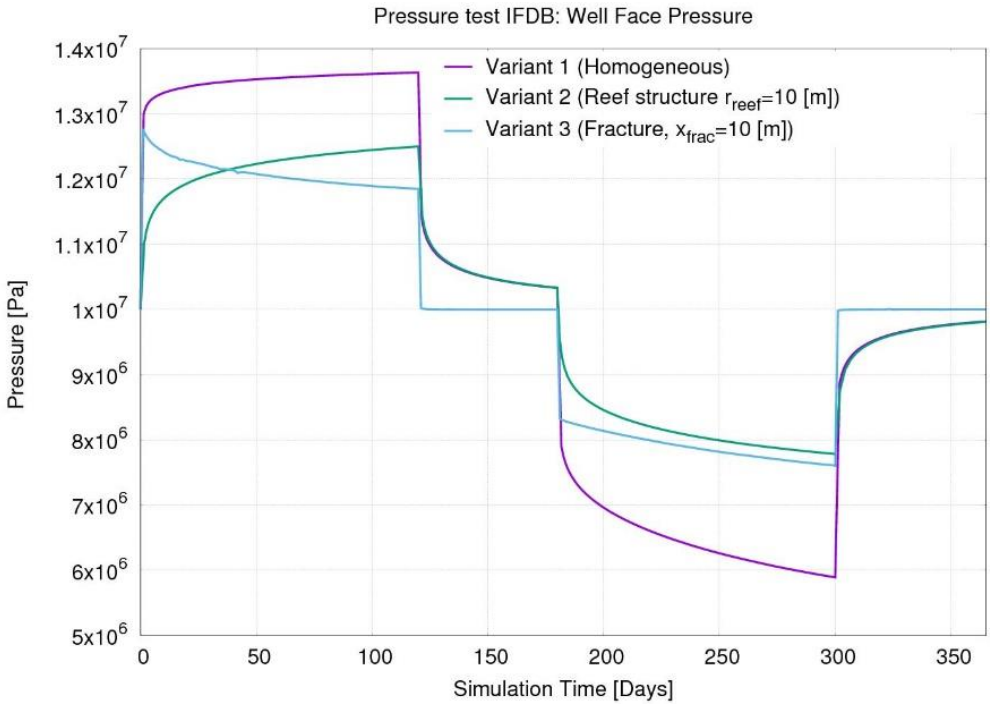


**Figure 2-6: Pressure response measured at the well face for the three variants of this test. Note that all time-steps have been sampled for this plot, in contrast to the eight time points that are expected, as indicated by Table 2-7.**

## 2.4.2 Simulation Description

Main characteristics of this test are identical to what was presented in Section 2.3.2, with some particular alterations:

1. Heat transfer is no longer neglected (i.e. non-isothermal flow, where heat advection and diffusion are present). Gravitational effects (e.g. buoyancy) are still neglected.
2. Initial reservoir temperature is uniform, of value $T_{res}$. During the injection phase, water temperature is of $T_{inj}$.
3. All fluid properties $\rho_f, \mu_f, \beta_f$ are functions of pressure and temperature, fluid thermal conductivity $\lambda_f$ is assumed to be constant.
4. Combined thermal properties such as conductivity and heat capacity are porosity-weighted:
$$\lambda_t = \phi\lambda_f + (1-\phi)\lambda_r \qquad and \qquad c_{p,t} = \phi c_{p,f} + (1-\phi)c_{p,r}$$
where $\lambda_t, \lambda_f$, and $\lambda_r$ are the thermal conductivities of the bulk, fluid, and rock, respectively and $c_{p,t}, c_{p,f}$, and $c_{p,r}$ are the specific heat capacities of the bulk, fluid, and rock, respectively
5. Pressure and temperature values are measured at $1, 10, 50, 100, 150, 200, 250, 300\ [m]$ at specified times (see section 2.4.3)
6. Flow rates vary depending on the stage/test:
    a. Injection: $Q = 0.001\left[\frac{m^3}{s}\right]$
    b. Falloff: $Q = 0.0\left[\frac{m^3}{s}\right]$
    c. Drawdown: $Q = -0.001\left[\frac{m^3}{s}\right]$
    d. Build-up: $Q = 0.0\left[\frac{m^3}{s}\right]$
7. In the second variant, a patch-reef structure is introduced, changing the permeability, porosity, thermal conductivity, and specific heat capacity values near the well, up to a distance of $r = r_{reef}$, to $k_{reef}, \phi_{reef}, \lambda_{reef}, c_{p_{reef}}$ respectively.

8. In the third variant, a fracture is introduced on the plane $x = x_{frac}$. This fracture inherits material properties from the host rock, except for permeability ($k_{frac}$) and porosity ($\phi_{frac}$). An aperture parameter $a_{frac}$ should be used to obtain the permeability via the "cubic law", where $k_{frac} = \frac{a_{frac}^2}{12}$ (Zimmerman & S. Bodvarsson, 1996).
9. Boundary conditions should not allow flow to exit or enter through the following surface intersections:
    a. Fracture – Top Boundary
    b. Fracture – Bottom Boundary
10. Under no circumstances should "well damage" factors be applied to the near-well-bore region. A change in such factors would affect the measured pressure at the well face, and thus could drastically affect the comparisons. Reservoir pressure and injection values are purposely planned to prevent, in particular, under-pressure (or negative pressure) issues.

A total number of 6 simulations to be run for this test, when counting the three variants, and the two types of meshes described in Section 2.4.3. Meshes used for this problem have similar near-well refinement characteristics to the coarse version of the analytical solution comparison test (i.e. test1).

### 2.4.3 Detailed Problem Specification

The sequence of the test, adheres to the following consecutive stages:

1. **Injection phase:** Injection of water at $Q = 0.001 \left[\frac{m^3}{s}\right]$ and $T_{inj} = 120$ ℃ for $120\ [days]$.
2. **Falloff phase:** Well is shut-in, $Q = 0 \left[\frac{m^3}{s}\right]$, for $60\ [days]$.
3. **Drawdown phase:** Well is opened to production at a constant rate $Q = -0.001 \left[\frac{m^3}{s}\right]$ for $120\ [days]$.
4. **Build-up phase:** Well is shut-in, $Q = 0 \left[\frac{m^3}{s}\right]$, for $65.25\ [days]$.

Two separate sets of meshes should be used for each variant: radial and Cartesian. The radial meshes used are shown in Figure 2-7 and the Cartesian meshes are shown in Figure 2-8. In the Cartesian mesh case, the domain planar cross section should be a square of sides of length $2r_{max}$ .

For the first variant, the mesh corresponding to reef variant may be used by assigning material properties to the reef material that are identical to the surrounding reservoir rock. Only variants 1 and 2 may be carried out under axisymmetric assumptions.

Details of the input parameters needed for all simulations are shown in Table 2-7. Notably, the initial pressure has been updated to $10^7 [Pa]$. This was done to avoid possible issues with negative pressures during the drawdown phase.

**Table 2-7: Simulation input specification for test2.**

| Variant | Parameter | Value |
|---|---|---|
| **All** | Fluid properties ( $\boldsymbol{\rho_f, \mu_f, \beta_f, c_{p,f}}$ ) | Functions of $p, T$ |
| **All** | Radial pressure/temperature probe locations (eight) | $1{,}10, 50, 100, 150, 200, 250, 300\ [m]$ |
| **All** | Reservoir Permeability ( $\boldsymbol{k}$ ) | $10^{-15}\ [m^2]$ |
| **All** | Reservoir Porosity ( $\boldsymbol{\phi}$ ) | $0.2\ [-]$ |
| **All** | Reservoir Rock Density ( $\boldsymbol{\rho_r}$ ) | $2680\ \left[\frac{Kg}{m^3}\right]$ |
| **All** | (dry) Reservoir Thermal Conductivity ( $\boldsymbol{\lambda_r}$ ) | $2.8\ \left[\frac{W}{m\cdot°K}\right]$ |
| **All** | Thermal Conductivity (Water, $\boldsymbol{\lambda_f}$) (assumed constant) | $0.6\ \left[\frac{W}{m\cdot°K}\right]$ |
| **All** | (dry) Reservoir Specific Heat Capacity ( $\boldsymbol{c_{p,r}}$ ) | $833\ \left[\frac{J}{Kg\cdot°K}\right]$ |
| **All** | Simulation end time ( $t_{end}$ ) | $1\ [year]\ (i.e\ 365.25\ [days], or\ 31557600\ [s])$ |
| **All** | Output times[9] (eight) | $0{,}50, 100, 150, 200, 250, 310, 365.25\ [days]$ |
| **All** | Domain radius ( $r_{max}$ **)** | $2400\ [m]$ |
| **All** | Domain height ( $h$ ) | $200\ [m]$ |
| **All** | Initial pressure ( $p_{res}$ ) | $10^7\ [Pa]$ |
| **All** | Initial temperature ( $\boldsymbol{T_{res}}$ ) | 34 ℃ |
| **All** | Injection temperature ( $\boldsymbol{T_{inj}}$ ) | 120 ℃ |
| **All** | Outer boundary pressure ( $\boldsymbol{p_{res}}$ at $\boldsymbol{r = r_{max}}$ ) | $10^7\ [Pa]$ |
| **2** | Reef Permeability ( $\boldsymbol{k_{reef}}$ ) | $10^{-12}\ [m^2]$ (Enos & Sawatsky, 1981) |
| **2** | Reef Porosity ( $\boldsymbol{\phi_{reef}}$ ) | $0.45\ [-]$ (Enos & Sawatsky, 1981) |
| **2** | Reef Rock Density ( $\boldsymbol{\rho_{reef}}$ ) | $2500\ \left[\frac{Kg}{m^3}\right]$ |
| **2** | (dry) Reef Thermal Conductivity ( $\boldsymbol{\lambda_{reef}}$ ) | 2.3 |
| **2** | (dry) Reef Specific Heat Capacity ( $\boldsymbol{c_{p,r_{reef}}}$ ) | $900\left[\frac{J}{Kg\cdot°K}\right]$ |
| **2** | Reef structure radius ( $\boldsymbol{r_{reef}}$ ) | $10\ [m]$ |
| **3** | Fracture aperture ( $\boldsymbol{a_{frac}}$ ) | $0.001\ [m]$ |
| **3** | Fracture Porosity ( $\boldsymbol{\phi_{frac}}$ ) | $0.5\ [-]$ |
| **3** | Fracture plane location ( $\boldsymbol{x_{frac}}$ ) | $10\ [m]$ |

[9] Note that, for practical reasons, this refers to the exact times of output.

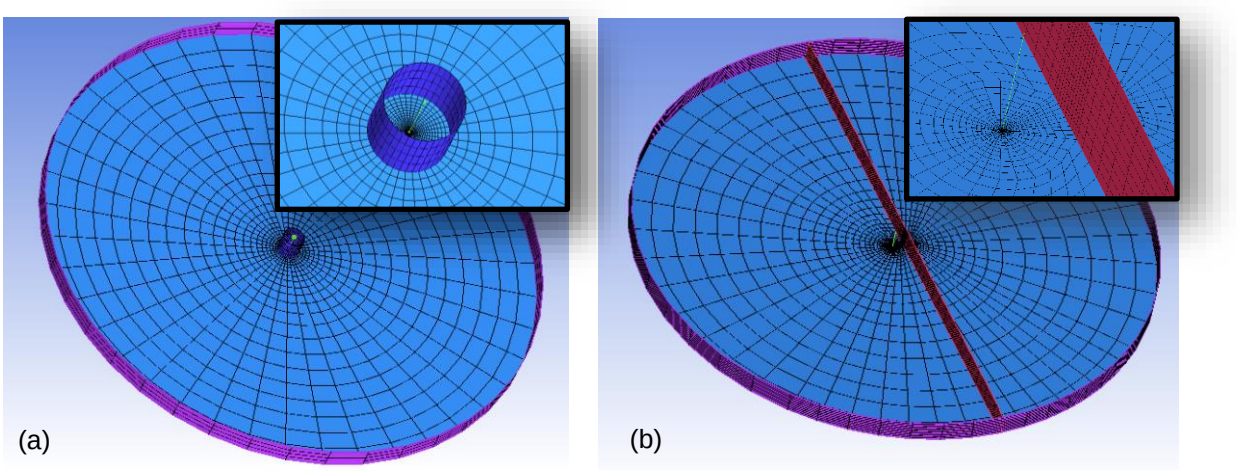


**Figure 2-7: Radial mesh samples to be used for the (a) reef variant, and (b) the fracture variant.**

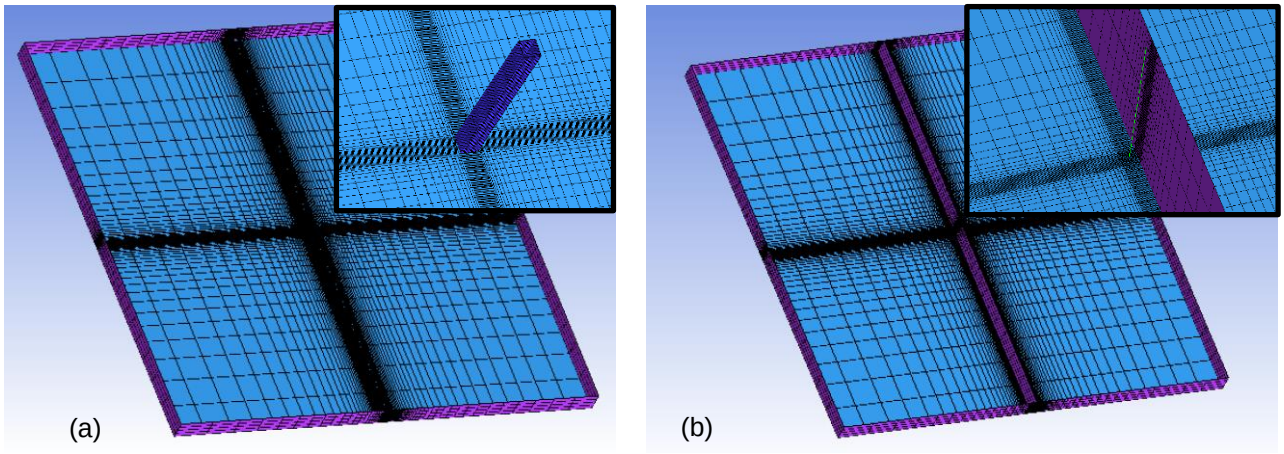


**Figure 2-8: Cartesian mesh samples to be used for the (a) reef variant, and (b) the fracture variant.**

## 2.4.4 Output Specification

All six simulations should report a solution for fluid pressure and temperature at locations measured radially from the wellbore along the x-axis (see Table 2-7, "*Radial temperature/pressure probe locations*"). The data should be reported via a set of ASCII[10] text files "`test2_radial _NAME_variant#.txt`" "`test2_cartesian_NAME_variant#.txt`" per variant, consisting of tab-delimited headers and values. NAME in the input file should be replaced with the full name of the author of the test result as well as the institution (e.g. "JulianMindel_ETHZ"), while # represents the variant number: 1 for the homogeneous case, 2 for the reef case, and 3 for the fracture case.

Values should be provided in scientific notation using at least twelve significant digits. A table of tab separated values from the evaluation of pressure and temperature solutions at the necessary locations and times is provided with this report (i.e. "`test2_IFDB_EXAMPLE.txt`") and should be used as a template for the output of this test (see Table 2-8). Ordered from left to right, columns should report pressure and temperature at each location. There should be a total of 17 columns when including a *time* column.

[10] https://en.wikipedia.org/wiki/Text_file

**Table 2-8: Output format example for pressure and temperature for the IFDB test.**

| TIME | P_PROBE_1 | T_PROBE_1 | P_PROBE_2 | T_PROBE_2 | P_PROBE_3 | T_PROBE_3 | P_PROBE_4 | T_PROBE_4 | P_PROBE_5 | T_PR |
|---|---|---|---|---|---|---|---|---|---|---|
| 0.000000000000e+00 | 9.999740448160e+06 | 1.200000000000e+02 | 9.999765317400e+06 | 3.400000000000e+01 | 9.999842590920e+06 | | | | | |
| 4.320000000000e+06 | 1.356820746330e+07 | 1.200000000000e+02 | 1.312015838100e+07 | 1.035282426010e+02 | 1.219453660120e+07 | | | | | |
| 8.640000000000e+06 | 1.365301687560e+07 | 1.200000000000e+02 | 1.321833883500e+07 | 1.087416945030e+02 | 1.240823536420e+07 | | | | | |
| 1.296000000000e+07 | 1.049717242550e+07 | 7.793233723400e+01 | 1.052105359440e+07 | 9.151144264060e+01 | 1.055239524830e+07 | | | | | |
| 1.728000000000e+07 | 4.269385770790e+06 | 8.228219104360e+01 | 5.421881638480e+06 | 6.985635801400e+01 | 7.078217345060e+06 | | | | | |
| 2.160000000000e+07 | 2.580950351670e+06 | 6.272708606050e+01 | 4.064586798670e+06 | 5.408963601490e+01 | 6.010390991390e+06 | | | | | |
| 2.678400000000e+07 | 7.973827296110e+06 | 5.696131505870e+01 | 8.191333967160e+06 | 4.841222919730e+01 | 8.448072770220e+06 | | | | | |
| 3.155760000000e+07 | 9.655561003630e+06 | 4.576039675980e+01 | 9.616076023630e+06 | 4.610288799460e+01 | 9.569804747960e+06 | | | | | |

Information should be provided via a separate text file "`test2_sys_application_info_NAME.txt`" regarding the simulator, compiler, compiler version, operating system, the CPU used and memory available, parallel capabilities used (e.g. CUDA, MPI, OpenMP), and mesh information. The table format and sample information was provided in Table 2-6 for the analytical transient pressure verification test. For this test, additional details should be provided regarding the solution algorithm sequence used, as well as the formulation (e.g. Finite Elements, Finite Volumes, decoupled fluid-rock heat equations, single coupled heat equation, monolithic approach, .etc.) in the comments section. An example of this text file is given by "`test2_sys_application_info_EXAMPLE.txt`" in the data bundle provided with this report.

## 2.4.5 Results

Through this test, simulators are meant to reproduce typical well test responses based on artificial yet representative underground realizations which include two essential types of heterogeneities: faults and reef structures. It is thus aimed at comparing TH modelling capabilities and results across the different participating applications.

Although all simulators were capable of performing at least one of the variants within test2, only four (COMPASS, Nexus-CSMP++, MOOSE, and CODE_BRIGHT) were able to carry out all of them. A detailed summary of these capabilities are summarized in Table 2-9. For the sake of completeness, it is important to note at this stage that while a particular simulator may be reported in a negative light (i.e. **No**), in some of the cases some participants may simply not have been able to submit results due to a lack of software-usage support or know-how, or of a particular commercially licensed feature. Nevertheless, each participant is also assumed to be fully aware of this handicap and the implications a comparative study such as the one presented here could have on the perception of suitability of their application for the purposes described by this benchmark.

**Table 2-9: Simulator capability summary per variant case for test2.**

| Simulator | Variant 1<br>Rad. mesh, Cart. mesh | Variant 2<br>Rad. mesh, Cart. mesh | Variant 3<br>Rad. mesh, Cart. Mesh |
|---|---|---|---|
| COMSOL v4.2a | **Yes**, **No** | **Yes**, **No** | **Yes**, **No** |
| COMPASS | **Yes**,**Yes** | **Yes**,**Yes** | **Yes**,**Yes** |
| MARTHE | **Yes**,**Yes** | **Yes**,**Yes** | **No**,**Yes** |
| Nexus-CSMP++ | **Yes**,**Yes** | **Yes**,**Yes** | **Yes**,**Yes** |
| MOOSE | **Yes**,**Yes** | **Yes**,**Yes** | **Yes**,**Yes** |
| SEAWATv4 | **Yes**,**Yes** | **Yes**,**Yes** | **No**,**Yes** |
| CODE_BRIGHT | **Yes**,**Yes** | **Yes**,**Yes** | **Yes**,**Yes** |
| Tough3 | **Yes**,**Yes** | **Yes**,**Yes** | **No**,**Yes** |
| PFLOTRAN | **Yes**,**Yes** | **Yes**,**Yes** | **No**, **No** |
| Eclipse100 | **No**,**Yes** | **No**,**Yes** | **No**,**Yes** |

Pressure results for variant 1 of this test, for both radial and cartesian meshes, are relatively comparable for most simulators, as can be observed in Figure 2-9 (a) and (b). Only CODE_BRIGHT and MOOSE appear to stand out in this respect with values spanning well beyond the range of values of the other 7 simulators. In

particular, for the Cartesian mesh case, CODE_BRIGHT presents a considerable delay in the pressure response. MOOSE, on the other hand, does not express delay but reports a higher level of asymmetry for pressure values observed during injection and drawdown (+3/-5 MPa).

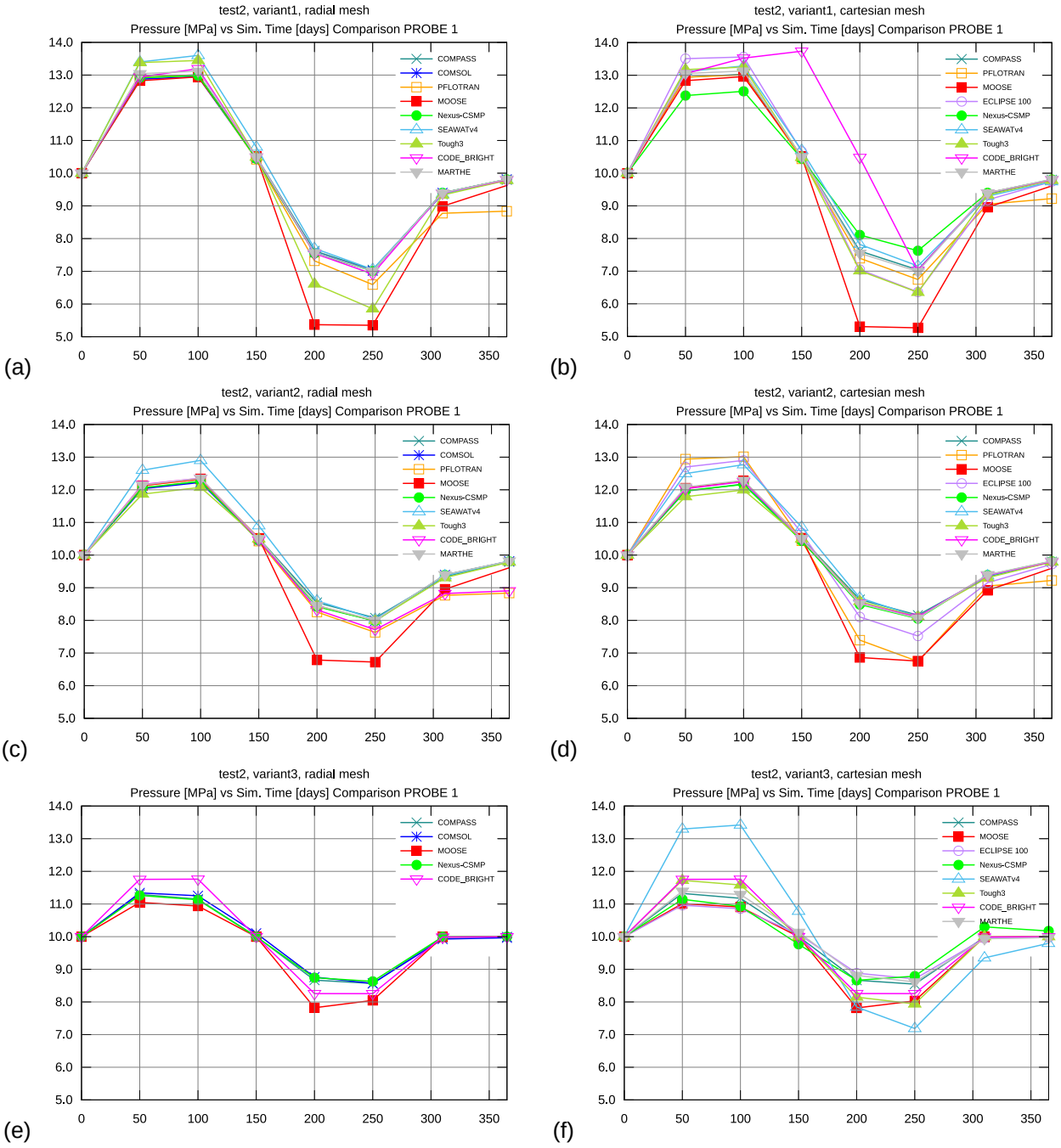


**Figure 2-9: Pressure [Mpa] vs. Time [days] comparison for the first probe point (PROBE_1), located at $r = 1[m]$ for test2 variants 1, 2, and 3. Subfigures (a), (c), and (d) represent results available on radial meshes, while (b), (d), and (f) represent results available on cartesian meshes.**

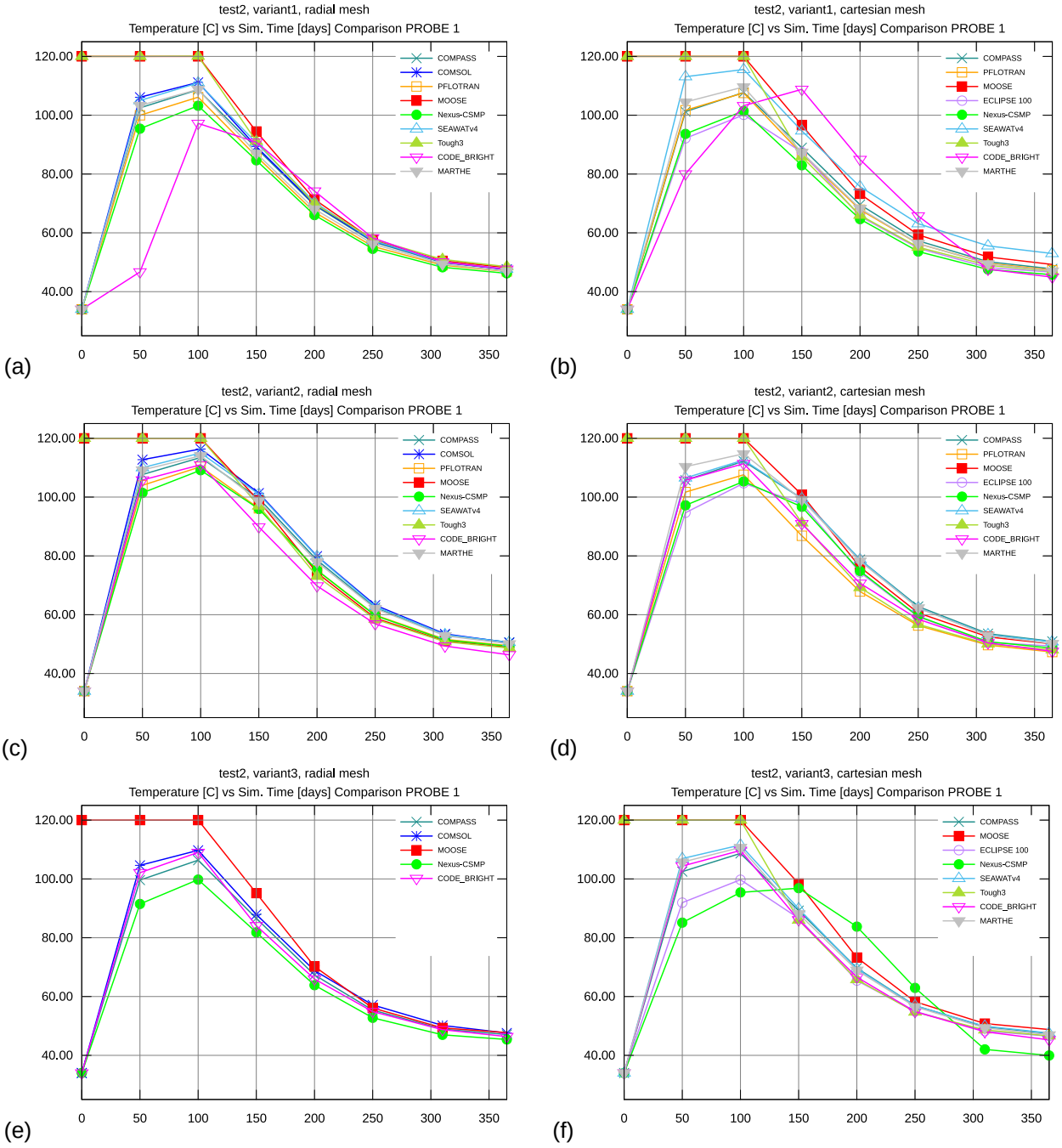


**Figure 2-10: Temperature [°C] vs. Time [days] comparison for the first probe point (PROBE_1), located at $r = 1[m]$ for test2 variants 1, 2, and 3. Subfigures (a), (c), and (d) represent results available on radial meshes, while (b), (d), and (f) represent results available on cartesian meshes.**

For variant 2, pressure results remain reasonably similar and symmetrical for injection and drawdown periods across simulators, with minor exceptions for MOOSE and SEAWATv4 in both mesh types (see Figure 2-9 (c) and (d)). For variant 3, in contrast to other simulators and consistent with its behaviour in variant 1 and 2, MOOSE reports a higher pressure change during drawdown than during injection, for the same flow rate magnitude (see Figure 2-9 (e) and (f)). The outlier for variant 3 however is SEAWATv4 when using a cartesian mesh, where the injection pressure change is higher than the change during drawdown.

In terms of temperature results for this test, variant 1 shows similar issues for CODE_BRIGHT in the form of a time delay (see Figure 2-10(a) and (b)). Nexus-CSMP++ displays a slight delay in the temperature

decrease for variant 3, radial mesh case during the fall-off and drawdown periods in comparison to other simulators. Furthermore, there seems to be an acceleration of this decrease during the build-up phase, leading to a considerable difference (i.e. ~-6 °C).

For all variants we can also observe that MOOSE and Tough3 have not used an enthalpy source-type condition at the injection site, but have resorted to a Dirichlet condition for temperature. The latter is evident from the fixed nature of the temperature evolution throughout the injection part of the simulation. In response to this observation the MOOSE benchmark test leader specified that: "*MOOSE is capable of specifying an enthalpy injection rate with other equations of state, but the specification of an enthalpy injection rate while using the EOS that was prescribed for this problem proves difficult. (…) . The equation of state for water uses IAPWS-IF97.*"

In all variant/mesh cases, since for some simulators meshes may have been manually to replicate the specifications of this test, a combination of this and the individual formulations used are likely the main reasons for the result discrepancies. The comparison of variant 3 is particularly challenging, as those simulators that manage to perform this sub-test tend to utilize different assumptions to model the presence of the single fracture. There may be some argument to the fact that there was no strict control or review over the particular implementation of the IAPWS standard used for calculating flow properties. Nevertheless, within reason, large discrepancies in such implementations would amount to much larger differences in the varied situations that were modelled by this test.

The complete set of results can be observed in section 7.4 Appendix D: TH Benchmark 1 - Test 2 results, where the remarks made for PROBE_1 are translatable to the remaining 7 probes placed downstream in sequence from the well face. For the probes placed farthest from the well (i.e. PROBE_5, PROBE_6, PROBE_7, and PROBE_8), small numerical fluctuations can be observed particularly for the temperature results. All simulators tested display these fluctuations, ranging ~+/-0.01°C. These small variations are likely due to cumulative numerical error of varying source (e.g. formulation, implementation, etc.), however a thorough assessment has not been made at the moment of writing this report.

Overall, it should be noted that with the exception of some notable outliers, the comparison of results for both pressure and temperature shown by Figure D-1 and Figure D-2 respectively, and observed in section 7.4 Appendix D: TH Benchmark 1 - Test 2 results are within reasonable agreement.

## 2.5 Test3: Experimental heat transport validation test

### 2.5.1 Problem Description

This test is aimed at studying unidimensional, unsteady, fluid and heat transport (i.e. TH) through porous media, with particular focus on thermal transport. It is based on the published material by (Singh, et al., 2006) who describes numerical results using two distinct solution approaches, while simultaneously comparing them to experimental results. Our aim is thus to emulate the settings of their experiment to be able to compare our simulation results with the experimental ones.

### 2.5.2 Simulation Description

The test comprises passing fluid through a pipe packed full of spheres of two different materials (i.e. one material per sub-test): steel, and glass (see Figure 2-11). Once flow is established and at a cool temperature $T_C$, the temperature is increased at the inlet to $T_H$, creating a step signal that is transported by the fluid through the pipe. Temperature sensors along the centreline of the pipe were used to record the temperature change with time inside the pipe at various locations during the physical experiment, and those values are used to verify numerical results.

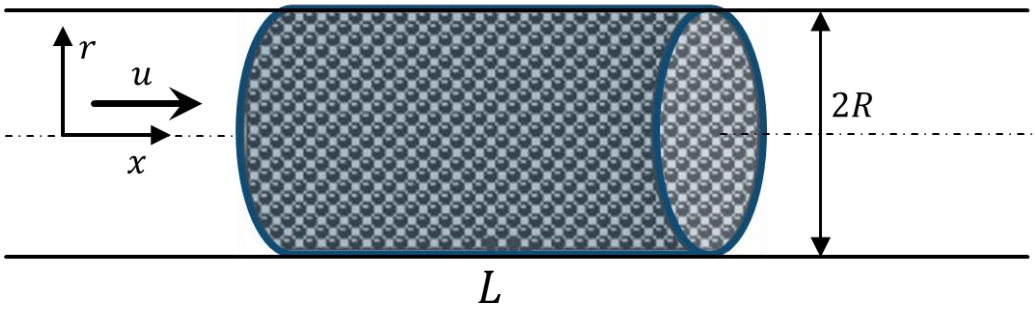


**Figure 2-11: Physical model and coordinate system (adapted from (Singh, et al., 2006) )**

Simulations should be run at one particular Péclet number per sub-test, shown in Table 2-10. Assuming a reference temperature of $300\,°K$ / $26.85\,℃$, an inflow velocity may be calculated via the Péclet number for heat transfer,

$$Pe = Re \cdot Pr = \frac{\rho_f \, c_{p,f} \, u \, R}{\lambda_f} \tag{2-13}$$

where $Re$ is the Reynolds number, and $Pr$ is the Prandtl number. In turn, these may be calculated via,

$$Pr = \frac{\mu_f \, c_{p,f}}{\lambda_f} \qquad Re = \frac{\rho_f \, u \, R}{\mu_f} \tag{2-14}$$

where $\mu_f$, $c_{p,f}$ and $\lambda_f$ are the fluid dynamic viscosity, heat capacity, and thermal conductivity, respectively. For the calculation of the Reynolds number ($Re$) a reference characteristic length equal to the radius $R$ of the pipe has been used, $u$ is the flow velocity, and $\rho_f$ is the fluid density. Physical properties of the spheres are given in Table 2-11. Furthermore, packing of the spheres results in a porosity $\phi$ of $0.37$ for the glass spheres, and $0.4$ for the steel spheres.

**Table 2-10: Experimental Péclet numbers used for each type of sphere. Values for water properties at $26.85\,℃$ ($c_{p,f} = 4178\,\left[\frac{J}{Kg°K}\right]$, $\lambda_f = 0.61\,\left[\frac{W}{m°K}\right]$, $\rho_f = 995.7\,\left[\frac{Kg}{m^3}\right]$) and a pipe radius $R = 0.029\,[m]$ were used to calculate inlet velocity.**

| Sphere type | Péclet Number Values | Corresponding Flow Velocity Values ($u$) |
|---|---|---|
| **Glass** | 1615 | $0.00817\,\left[\frac{m}{s}\right]$ |
| **Steel** | 2190 | $0.01107\,\left[\frac{m}{s}\right]$ |

**Table 2-11: Solid sphere material properties (extracted from (Singh, et al., 2006) ).**

| Solid phase | $\rho$, kg m$^{-3}$ | $C_p$, J (kg K)$^{-1}$ | $\lambda_s$ W (m K)$^{-1}$ |
|---|---|---|---|
| Glass | 2,225 | 840 | 1.09 |
| Steel | 7,900 | 477 | 14.9 |

A total of two simulations should be run for this problem, corresponding to the two available porous medium materials. These simulations should include assumptions of non-isothermal single-phase, slightly compressible porous media flow. Given the characteristics of the test, fluid flow ($u_f$) should either be uniformly prescribed throughout the domain, or calculated via non-Darcy methods. Additionally, gravitational effects may be ignored.

Flow is considered positive in the positive direction of the x-axis, which should be the preferred orientation of the pipe. Unless x-scaling is used, a different mesh (see Figure 2-12) is needed for each case given the different lengths of the pipes for each sphere type. Understandably, planes of symmetry, or cylindrical coordinate capabilities may be used to reduce run-time and simplify calculations.

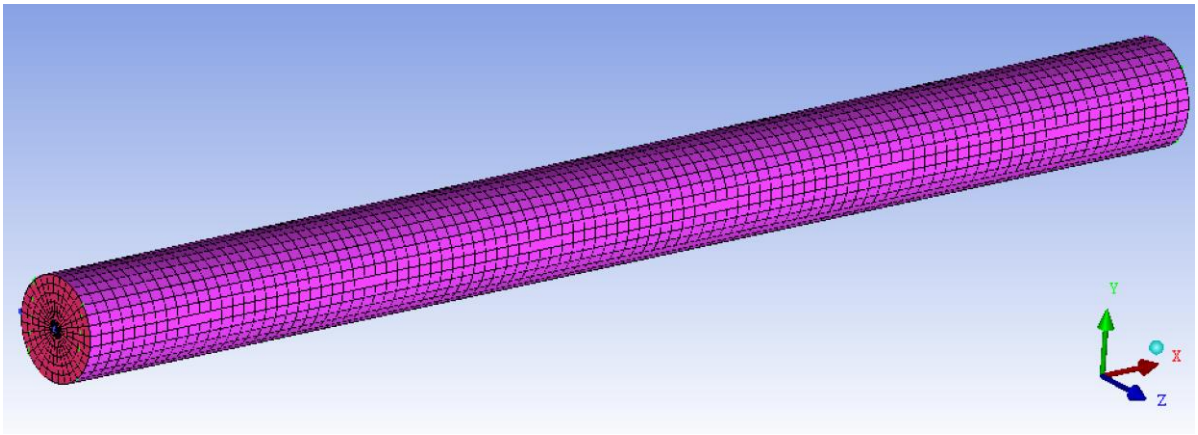


**Figure 2-12: Sample mesh for the pipe containing glass spheres.**

Boundary conditions should be applied which create uniform flow rate along the pipe corresponding to the particular Péclet number detailed in Table 2-10. If (optionally) solving for pressure to obtain velocity, (see section 2.5.2.1), this should be a combination of a velocity/flowrate condition (e.g. at the inlet), and standard atmospheric pressure (e.g. at the outlet), if solving for pressure. No flow of heat or mass is allowed through the side walls. Inlet water temperature should follow the supplied experimental data for $x = 0\ [m]$ (i.e. `glass_1615_Z0.txt`, and `steel_2190_Z0.txt`) as a time-dependent Dirichlet condition. This was also carried out by (Singh, et al., 2006) to avoid issues with flow development at the inlet. Data for two other downstream observation points in each case are provided in files `glass_1615_Z11.txt, glass_1615_Z22.txt, steel_2190_Z5.txt, and steel_2190_Z10.txt`. Experimental values provided in data files are non-dimensional (i.e. non dimensional time $t_{exp}$, and non-dimensional temperature $T_{exp}$):

$$t_{exp} = t\frac{\alpha_f}{R^2}\ and\ T_{exp} = \frac{T - T_C}{T_H - T_C}$$

where $\alpha_f$ is the fluid thermal diffusivity calculated via $\alpha_f = \frac{\lambda_f}{\rho_f c_{p,f}}$ and values described in Table 2-10 should be used to construct it. Each experimental file consists of two columns of data extracted from plots by (Singh, et al., 2006), with the left one corresponding to $t_{exp}$ and the right not to $T_{exp}$.
The outlet temperature gradient should be set to zero (i.e. $\left.\frac{\partial T}{\partial x}\right|_L = 0$). The side-wall should be assumed to be adiabatic (i.e. $\frac{\partial T}{\partial r} = 0$). The remaining two points of observation in each sub-test should be used for validation. Initial conditions are of steady flow at a temperature $T_C$.

It is important to know that the simplest approximation in this problem is provided by the assumption of instantaneous thermal equilibrium between the solid and fluid phases. When this simplification may not be assumed by a particular simulator, details are provided by (Singh, et al., 2006) for the case of simulating transient heat transfer between the solid and the fluid.

Due to the non-Darcian magnitude of the velocities involved, an effective thermal conductivity of the fluid may be calculated, that includes dispersion effects,

$$\lambda_{eff,f}\big|_x = \lambda_f(\phi + 0.5Pe) \qquad (2\text{-}15)$$

Given that this dispersion effect is influenced by the flow direction, it introduces anisotropy into the effective thermal conductivity. Hence, if anisotropic material properties are an available feature of a particular simulator, equation (2-15) should be used for the component corresponding to the flow direction, while

$$\lambda_{eff,f}\big|_r = \lambda_f(\phi + 0.1Pe) \qquad (2\text{-}16)$$

should be used for the radial component.

When using a formulation that assumes instantaneous thermal equilibrium between the solid spheres and the fluid, a combined thermal conductivity may be calculated. This can be done via a porosity weighted approach:

$$\lambda_{eff,m}\big|_x = \lambda_f(\phi + 0.5Pe) + \lambda_s(1-\phi) \quad (2\text{-}17)$$

$$\lambda_{eff,m}\big|_r = \lambda_f(\phi + 0.1Pe) + \lambda_s(1-\phi) \quad (2\text{-}18)$$

### 2.5.2.1 Solving for flow velocity (optional)

An approach for solving flow velocity is not reported by (Singh, et al., 2006), and a constant uniform value is assumed for numerical calculations. The Kozeny-Carman (Kozeny, 1927) (Carman, 1937) (McCabe, et al., 2005) semi-empirical formula may be used to estimate the corresponding value of permeability based on porosity. It is typically used to calculate the pressure loss of fluid flowing through a packed bed of solids, and it can be described by (i.e. in one of its forms),

$$\frac{\Delta p}{L} = -\frac{180\mu_f(1-\phi)}{\Phi_s\, d_p^2\, \phi^3}u \quad (2\text{-}19)$$

where $\Delta p$ is the pressure drop, $d_p$ is the particle diameter, $\Phi_s$ is the particle *sphericity* (i.e. with a value of 1 for spheres), and $\phi$ is the medium porosity. In contrast to the original numerical test presented by (Singh, et al., 2006), using equation (2-19) allows us to perform transient calculations of both heat and mass transfer. Thus, we able to verify the TH capabilities of the benchmarked simulators by comparing to their physical experiments. Substituting the definition of Darcy velocity into (2-19) we obtain,

$$\frac{\Delta p}{L} = \frac{180\mu_f(1-\phi)}{\Phi_s^2\, d_p^2\, \phi^3}\frac{k}{\mu_f}\frac{\Delta p}{L} \quad \rightarrow \quad k = \frac{\Phi_s^2 d_p^2 \phi^3}{180(1-\phi)^2} \quad (2\text{-}20)$$

A summary of particle diameter, pipe length, porosity and resulting permeability values is presented in Table 2-12. The experimental test section is reported to be of $R = 0.029\ [m]$ while the length varies from $L = 0.725\ [m]$ for the glass sphere sub-test to $L = 0.465\ [m]$ for the steel sphere sub-test.

**Table 2-12: Permeability estimate via the Kozeny-Carman relation.**

| Parameter | Value (left: Glass sub-test, right: Steel sub-test) | |
|---|---|---|
| **Pipe length ( $L$ )** | $0.725\ [m]$ | $0.465\ [m]$ |
| **Porosity ( $\phi$ )** | 0.37 | 0.4 |
| **Particle Diameter ( $d_p$ )** | $0.00225\ [m]$ | $0.00476\ [m]$ |
| **Permeability ( $k$ )**[11] | $3.59 \cdot 10^{-9}\ [m^2]$ | $2.24 \cdot 10^{-8}\ [m^2]$ |

Once a value of permeability is determined, we may proceed to solve for fluid pressure, and ultimately flow velocity. Due to the flow conditions ($Re_{glass} \approx 295, Re_{steel} \approx 400$) the Darcy approximation to flow velocity is not an appropriate estimate. In such a case, the Darcy-Forchheimer-Brinkman approach may be used to calculate velocity, thus taking into account the now more relevant inertia effects. Darcy's formula is replaced by (Baghapour, et al., 2018),

$$-\frac{\partial p}{\partial x} = \frac{\mu_f}{k}u + \mathrm{B}u^2 \quad (2\text{-}21)$$

where $\mathrm{B}$ is an empirical parameter that can be approximated via

$$\mathrm{B} = \frac{1.75\rho(1-\phi)}{d_p\phi^3} \quad (2\text{-}22)$$

[11] Calculated via equation (2-20).

Equation (2-21) needs to be taken into account in the simulator's discretization formulation, and it will introduce non-linearity into the problem. Nevertheless, it is probably the most appropriate approach to approximating fluid flow solution and ultimately validates the complete TH scheme with the cited experimental work.

### 2.5.3 Detailed Problem Specification

Fluid and thermal properties, including flow rate values, are provided by the original paper, and a full list of compiled parameters used for our comparison is provided in Table 2-13.

**Table 2-13: Simulation input specification.**

| Parameter | Value (left: Glass sub-test, right: Steel sub-test) | |
|---|---|---|
| **Fluid properties ( $\rho_f$, $\mu_f$, $\beta_f$, $c_{p,f}$)** | Functions of $p, T$ | |
| **Thermal Conductivity (Water, $\lambda_f$)** (assumed constant) | $0.61\ \left[\frac{W}{m\cdot°K}\right]$ | |
| **Material density ( $\rho$ )** | $2225\ \left[\frac{Kg}{m^3}\right]$ | $7900\ \left[\frac{Kg}{m^3}\right]$ |
| **Permeability ( $k$ )**[12] | $3.59 \cdot 10^{-9}\ [m^2]$ | $2.24 \cdot 10^{-8}\ [m^2]$ |
| **Porosity ( $\phi$ )** | $0.37$ | $0.4$ |
| **(dry) Thermal Conductivity ( $\lambda_s$ )**[13] | $1.09\ \left[\frac{W}{m\cdot°K}\right]$ | $14.9\ \left[\frac{W}{m\cdot°K}\right]$ |
| **(dry) Specific Heat Capacity ( $c_p$ )** | $840\ \left[\frac{J}{Kg\cdot°K}\right]$ | $477\ \left[\frac{J}{Kg\cdot°K}\right]$ |
| **Inlet Temperature ( Cold, $T_C$ )** | $300\ °K\ /\ 26.85\ ℃$ | |
| **Inlet Temperature ( Hot, $T_H$ )** | $315\ °K\ /\ 41.85\ ℃$ | |
| **Inlet flow velocity ( $u$ )** | $0.00817\ \left[\frac{m}{s}\right]$ | $0.01107\ \left[\frac{m}{s}\right]$ |
| **Pipe radius ( $R$ )** | $0.029\ [m]$ | |
| **Pipe length ( $L$ )** | $0.725\ [m]$ | $0.465\ [m]$ |
| **Temperature Probe Locations ( $x$ ) (Thermocouple Locations)** $Z = \frac{x}{R}$ | $0\ [m]\ (Z = 0)$ | $0\ [m]\ \ (Z = 0)$ |
| | $0.319\ [m]\ (Z = 11)$ | $0.145\ [m]\ (Z = 5)$ |
| | $0.638\ [m]\ (Z = 22)$ | $0.290\ [m]\ (Z = 10)$ |
| **Output intervals ( $t$ )**[14] | $\left\{\frac{(100\cdot R)^2}{\alpha_f}\Delta t_{exp}\cdot i\right\}_{i=0}^{17}, where\ \Delta t_{exp} = 0.0025\ and\ \alpha_f = 0.00146\ \left[\frac{cm^2}{s}\right]$ | |
| **Total Simulation Time** | $0.04 \cdot \frac{(100\cdot R)^2}{\alpha_f} = 230.41096\ [s]$ | |
| **Mesh spacing** | $0.01 \cdot L = 0.00725\ [m]$ | $0.01 \cdot L = 0.00465\ [m]$ |
| **Suggested Timestep**[15] | $0.0230\ [s]$ | |

[12] Calculated via equation (2-20) if flow velocity (i.e. solution for pressure) is modelled.
[13] Note that values of thermal conductivity should be updated for dispersion effects via equations (2-15) and (2-16)
[14] A summary table of output times is provided in 7.2 (section 7.2).
[15] Timestep requirements may vary depending on formulation used in each simulator.

## 2.5.4 Output Specification

Both simulations should report a solution for temperature measured at the specified locations along the pipe domain (see Table 2-13, "T*emperature probe locations*"). The data should be reported via two ASCII[16] text files (e.g. "`test3_Steel_NAME.txt`", "`test3_Glass_NAME.txt`") consisting of tab-delimited headers and values. NAME in the input file should be replaced with the full name of the author of the test result as well as the institution (e.g. "JulianMindel_ETHZ").

Values should be provided in scientific notation using at least twelve significant digits. A table of tab separated values of temperature at the monitored locations, relative error, and times is provided with this report (i.e. "`test3_Glass_EXAMPLE.txt`") and should be used as a template for the output of this test (see Table 2-14). Ordered from left to right, columns should report temperature at each location. There should be a total of 7 columns when including a *time* column. A sample comparison of results is presented in Figure 2-13.

**Table 2-14: Output format example for temperature and relative error results at each probe (test3)**

| TIME | PROBE_1 | PROBE_2 | PROBE_3 | REL_ERROR_PROBE1 | REL_ERROR_PROBE2 | REL_ERROR_PROBE3 |
|---|---|---|---|---|---|---|
| 0.00000000000E+00 | 2.68500000000E+01 | 2.68500000000E+01 | 2.68500000000E+01 | 0.00000000000E+00 | 0.00000000000E+00 | 0.00000000000E+00 |
| 1.44006849300E+01 | 2.91203204460E+01 | 2.68500763947E+01 | 2.68500620143E+01 | 8.11983164100E-04 | 2.84524022342E-06 | 2.30965735565E-06 |
| 2.88013698600E+01 | 3.50378624572E+01 | 2.71367158904E+01 | 2.68501459640E+01 | 2.57105897028E-03 | 1.15234204533E-02 | 5.43627560514E-06 |
| 4.32020547900E+01 | 3.89828544931E+01 | 3.04176127511E+01 | 2.68541560366E+01 | 2.18194688403E-03 | 7.53956950256E-02 | 1.54787210428E-04 |
| 5.76027397200E+01 | 4.04110565322E+01 | 3.62195215565E+01 | 2.75707396241E+01 | 3.80993869188E-03 | 9.55271003885E-02 | 2.73707710565E-02 |
| 7.20034246500E+01 | 4.10066094824E+01 | 3.93759828939E+01 | 3.16601365755E+01 | 4.19584643919E-04 | 4.70476931612E-02 | 1.41199026895E-01 |
| 8.64041095800E+01 | 4.13752850119E+01 | 4.05719022575E+01 | 3.70950159684E+01 | 5.16754987095E-04 | 2.00492656106E-02 | 1.96795029178E-01 |
| 1.00804794510E+02 | 4.16636150089E+01 | 4.10954260169E+01 | 3.97004491166E+01 | 2.05450178742E-04 | 1.09886081094E-02 | 1.02014543701E-01 |
| 1.15205479440E+02 | 4.18161869446E+01 | 4.14427265896E+01 | 4.06952300105E+01 | 8.95883977896E-05 | 8.09347181478E-03 | 4.72401141564E-02 |
| 1.29606164370E+02 | 4.18625476870E+01 | 4.17059800946E+01 | 4.11706889458E+01 | 2.99825256870E-04 | 6.62284274515E-03 | 2.96845521722E-02 |
| 1.44006849300E+02 | 4.18634356938E+01 | 4.18274985464E+01 | 4.15057074706E+01 | 3.21044057348E-04 | 1.76709390184E-03 | 1.48562571210E-02 |
| 1.58407534230E+02 | 4.18634356938E+01 | 4.18620791305E+01 | 4.17407421415E+01 | 3.21044057348E-04 | 1.03175545414E-03 | 1.09530073823E-02 |
| 1.72808219160E+02 | 4.18634356938E+01 | 4.18622903204E+01 | 4.17444420707E+01 | 3.21044057348E-04 | 4.87122153999E-04 | 6.31005766669E-03 |
| 1.87208904090E+02 | 4.18634356938E+01 | 4.18622903204E+01 | 4.17444420707E+01 | 3.21044057348E-04 | 4.87122153999E-04 | 3.98502919399E-03 |
| 2.01609589020E+02 | 4.18634356938E+01 | 4.18622903204E+01 | 4.17444420707E+01 | 3.21044057348E-04 | 4.87122153999E-04 | 1.08914969484E-03 |
| 2.16010273950E+02 | 4.18634356938E+01 | 4.18622903204E+01 | 4.17444420707E+01 | 3.21044057348E-04 | 4.87122153999E-04 | 1.85073435515E-03 |
| 2.30410958880E+02 | 4.18634356938E+01 | 4.18622903204E+01 | 4.17444420707E+01 | 3.21044057348E-04 | 4.87122153999E-04 | 3.13044020895E-03 |

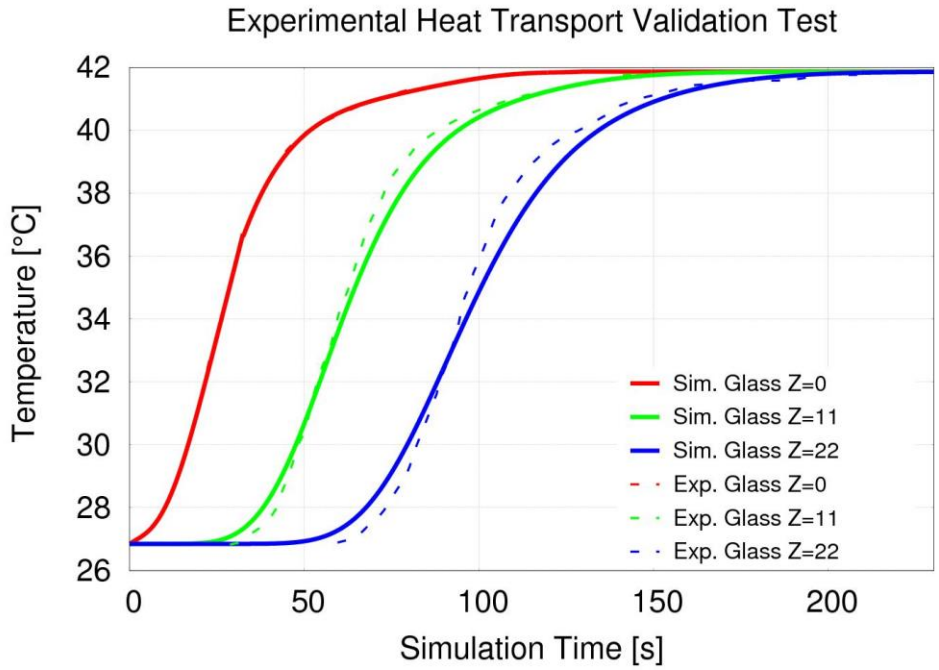


**Figure 2-13: Sample experimental vs. numerical comparison for the pipe containing glass spheres.**

Information should be provided via a separate text file "`test3_sys_application_info_NAME.txt`" regarding the simulator, compiler, compiler version, operating system, the CPU used and memory available, parallel capabilities used (e.g. CUDA, MPI, OpenMP), and mesh information. The table format and sample information was provided in Table 2-6 for the analytical transient pressure verification test. For this test, additional details should be provided regarding the solution algorithm sequence used, particularly for the

[16] https://en.wikipedia.org/wiki/Text_file

heat transport approach, as well as the formulation (e.g. Finite Elements, Finite Volumes, decoupled fluid-rock heat equations, single coupled heat equation, .etc.) in the comments section. An example of this text file is given by "`test3_sys_application_info_EXAMPLE.txt`" in the data bundle provided with this report.

### 2.5.5 Results

The goal of this test is to compare simulator heat transport capabilities while shifting the focus away from the obtainment of a transport velocity. The singular dimension of the flow considered by this experiment provides an ideal setting for this comparison as mesh requirements become more flexible. Thus, all simulators were able to perform this test, as evidenced by the results presented in Figure 2-14 and Figure 2-15.

All simulators were able to read in the input boundary conditions set by the temperature time-dependent profile at PROBE_1. This implies that the level of error at this particular monitoring point should be extremely low. Only Eclipse100 produced a read-in error above 2% for both the glass and steel spheres case. Only for the steel spheres, COMSOL also produced an error above 2% which, after careful review, suggests that the glass sphere case input was erroneously used for the steel sphere case. At the time of drafting this report, a correction was not received from the corresponding participant.

Most simulators (i.e. COMPASS, COMSOL, PFLOTRAN, MOOSE, Nexus-CSMP++, SEAWATv4, CODE_BRITGHT, MARTHE) remained in relative close agreement with the experimental results, and with one another. The shapes of the time-dependent temperature monitor at each probe location remained qualitatively very similar to experimental results, with an observed slight speedup of the thermal front. In decreasing order of importance, the slight speedup expressed by the first group of simulators is most likely due to a combination of:

1. Heat losses through walls were not modelled (i.e. $\partial T/\partial r = 0$). This would have the greatest effects, with the heat being lost radially and a subsequent subtle slow-down of the temperature front.
2. Over-prediction of Péclet-based diffusion (i.e. equation (2-15)). This would cause a change in the slope of the T vs t curves.
3. Slight over-prediction of transport velocity (see Table 2-10). This is assumed to be rather unlikely or with the least effect (i.e. within some reasonable degree of numerical precision) given the length of the modelled domain. If the estimated values for the velocities were incorrect, then so would be the experimental setup.
4. Assuming all simulators have followed the described mesh geometry accurately for each case related to a type of sphere, and all numerical methods used are consistent and stable, a grid effect is very unlikely a major factor.

Continuing further within this first sub-group of simulators, at probes 2 and 3 maximum levels of error observed are ~10% and ~20% for glass spheres, and ~4% and ~7% for steel spheres, respectively. COMSOL shows a slightly elevated level of diffusion, as evidenced by the difference in the slope (i.e. $\partial T/\partial t$) of the line in both Steel and Glass sphere cases.

Establishing the second group of simulators, Eclipse100 and Tough3 remained as the main outliers due to their exceptionally slow-progressing and diffuse temperature profile leading to elevated error values ranging from ~15% to ~30%. In the case of Tough3, the overall shape of the temperature time-profile remains similar to the experiments, however it is severely delayed. The latter is reportedly difficult to assess, but is likely due to a setup/configuration issue or an inadvertent excessive heat loss through non-adiabatic walls. Results from Eclipse100 likely suffered from similar effects, coupled to excessive diffusion (i.e. numerical and/or physical), as supported by the slant in most of the curves shown in Figure 2-14 (b and c) and Figure 2-15 (b and c).

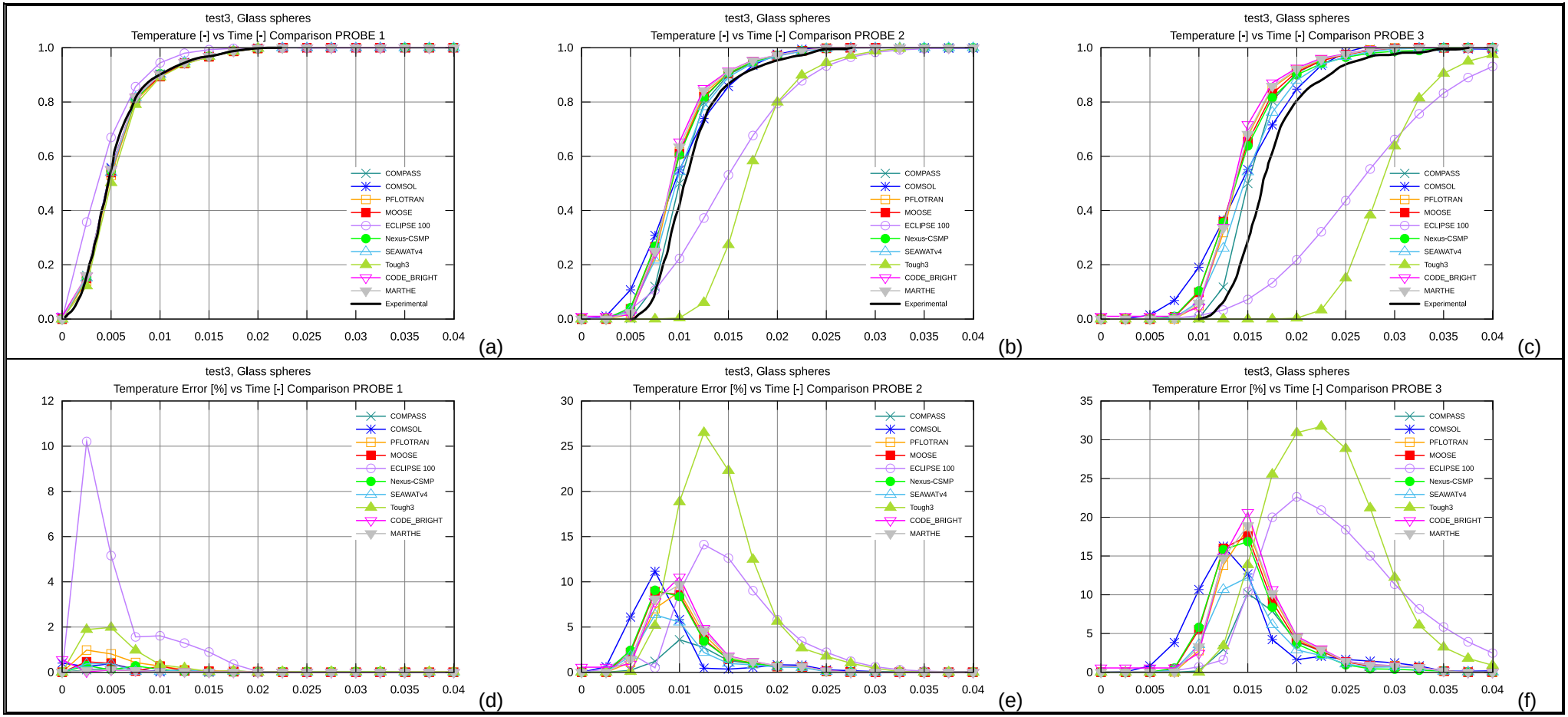


**Figure 2-14: Temperature [ºC] and Error [%] vs non dimensional time [-] for the glass sphere simulation as part of test3. Each column of plots represents measurements at a particular probe (i.e. 3 probes In total), while the top row represents temperature, and bottom row represents error. Note that PROBE_1 is essentially an input boundary condition.**

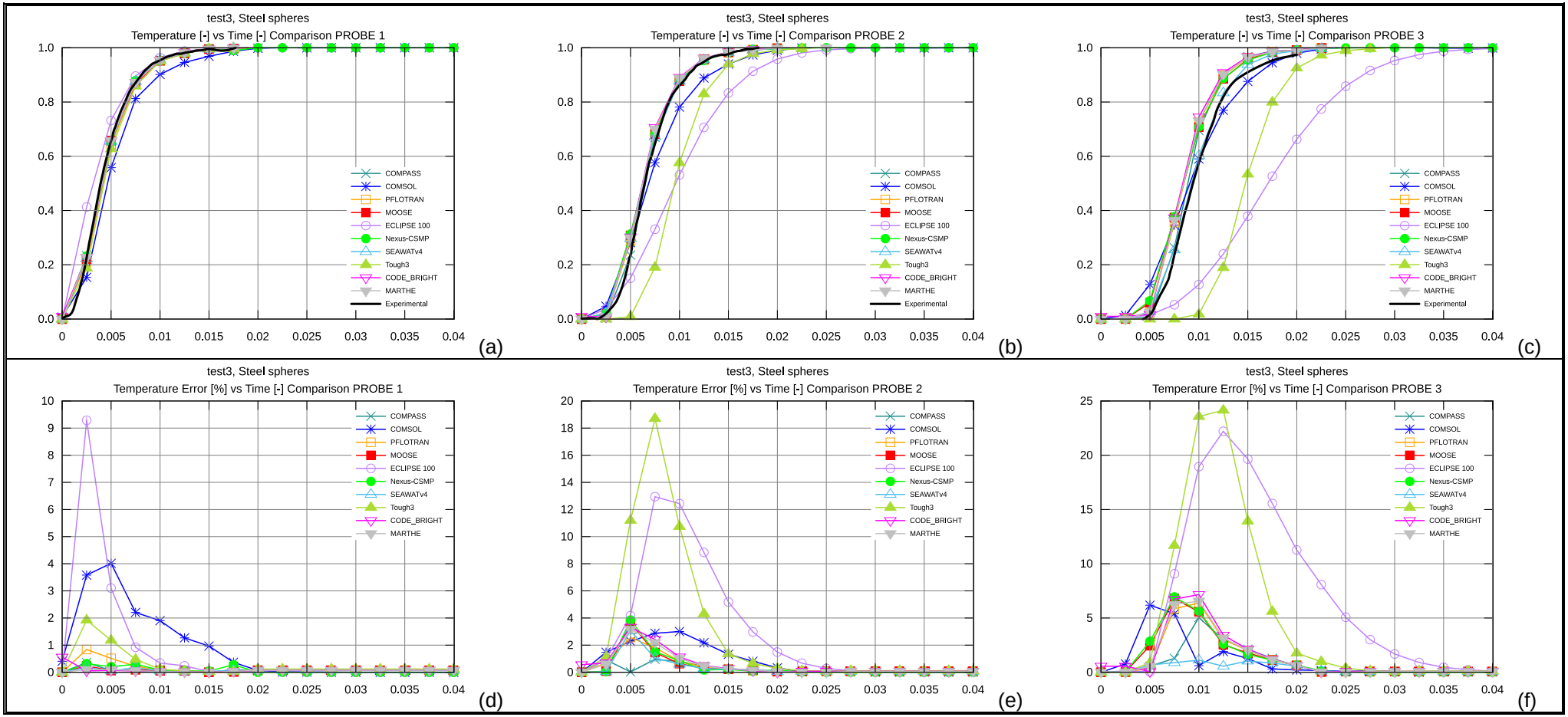


**Figure 2-15: Temperature [ºC] and Error [%] vs non dimensional time [-] for the steel sphere simulation as part of test3. Each column of plots represents measurements at a particular probe (i.e. 3 probes In total), while the top row represents temperature, and bottom row represents error. Note that PROBE_1 is essentially an input boundary condition.**

## 2.6 Test4: Horton-Rogers-Lapwood problem test

This test is based on modelling internal natural convection in a porous medium. This essentially implies that the fluid is always contained within the modelled domain, while heat may leave and enter it. The focus of this test is on determining and comparing the thermal-buoyancy modelling capabilities of simulators, and to act as a complement to the test presented in Section 2.5 (test3).

### 2.6.1 Problem Description

This test is based on creating the conditions for a self-organizing non-linear phenomenon, typically called Rayleigh–Bénard (RB) convection. RB convection is the term used to describe the flow characteristics in the general case of a free fluid, while the Horton-Rogers-Lapwood (HRL) problem addresses RB convective flow in the particular low inertia case of a saturated porous medium (Horton & Rogers, 1945) (Lapwood, 1948).

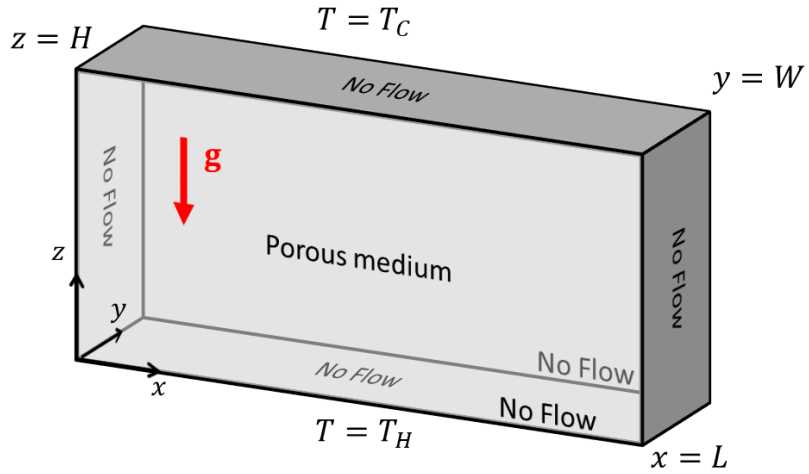


**Figure 2-16: Three dimensional schematic of the Horton-Rogers-Lapwood problem, ideally consisting of a horizontally infinite (x-axis), saturated porous medium domain subjected to heating from below and gravitational forces (g).**

Given a liquid-water-saturated porous medium (i.e. see Figure 2-16) of constant isotropic permeability $k$, thermal conductivity $\lambda_r$, density $\rho_r$, and heat capacity $c_{p,r}$, it is subjected to thermally conductive (i.e. constant temperature) boundary conditions at the top and bottom of temperatures $T_C$ and $T_H$, respectively, in the presence of gravitational acceleration **g**. Initial conditions are given by a static thermal gradient defined by $\frac{T_H - T_C}{H}$ and hydrostatic pressure conditions.

In such a setting (i.e. Figure 2-16) it is useful to characterise the expected convection onset based on the Rayleigh number, defined as the ratio between the diffusive and buoyant thermal transport time scales,

$$Ra = \frac{\Delta t_{diff}}{\Delta t_{grav}} \tag{2-23}$$

These timescales are dictated on one hand by the thermal diffusivity $\alpha_t$ of the combined fluid and porous medium, and on the other by the buoyancy-triggering density differences of the fluid. Hence,

$$\Delta t_{diff} = \frac{H^2}{\alpha_t} \qquad \Delta t_{grav} = \frac{H}{\left(\frac{\Delta \rho_f k g}{\mu_f}\right)} \tag{2-24}$$

and finally,

$$Ra = \frac{\Delta \rho_f k g H}{\mu_f \alpha_t} \tag{2-25}$$

where $\mu_f$ is the fluid viscosity and $\Delta \rho_f$ is defined as the fluid density difference between the two temperatures $T_C$ and $T_H$. The combined thermal diffusivity is given by,

$$\alpha_t = \frac{\lambda_t}{\rho_t c_{p,t}}, \quad \lambda_t = \lambda_f \phi + \lambda_r (1-\phi), \quad \rho_t = \rho_f \phi + \rho_r (1-\phi), \quad c_{p,t} = c_{p,f} \phi + c_{p,r} (1-\phi), \tag{2-26}$$

where subscripts $f, r,$ and $t$ indicated fluid, rock, and total properties, respectively. A porosity-weighted approach has been used to estimate total values necessary for $Ra$ calculations.

As shown by (Beck, 1972), and also by (Florio, 2017) in Figure 2-17, where $h_1 = \frac{L}{H}, h_2 = \frac{W}{H}$, as long as the domain dimensions in the y-direction remain sufficiently small in comparison to $x$ and $z$, convection will happen only along the $x - z$ plane. This allows testing three dimensional gravitationally-driven heat transport features of simulators as well as observing and comparing results qualitatively and somewhat quantitatively with relative ease.

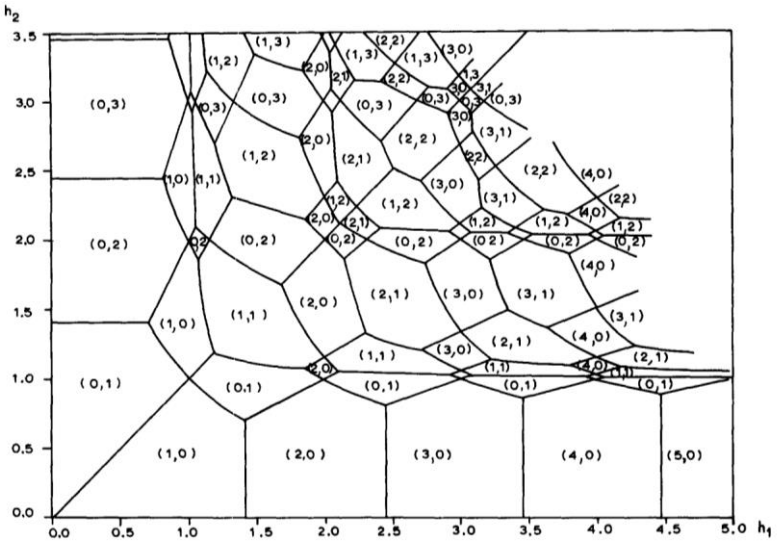


**Figure 2-17: Preferred cellular convection modes, as a function of $h_1$, and $h_2$, as originally presented by (Beck, 1972).**

## 2.6.2 Simulaton Description

Simulations for this test case are designed to run at Rayleigh numbers above the critical one ($Ra_c$), thus triggering the appearance of RB cells. In general, the higher the Rayleigh number, the higher the number of these cells. For very high Rayleigh numbers chaotic conditions would develop, and depending on thermal properties, Darcy assumptions would eventually cease to be valid (i.e depending on the Reynold's number).

Using simulation values provided in Table 2-15, $\boldsymbol{Ra}$ can be estimated using equation (2-25) and a plot can be constructed of $\boldsymbol{Ra}$ as a function of permeability, as shown in Figure 2-18. Values for the simulation cases were selected based on this plot.

All boundaries should be set to be impermeable (i.e. no-flow), and the vertical boundaries should be set to be adiabatic. The top and bottom boundaries should be set to be conductive at $T_C$ and $T_H$ , respectively. Initial conditions correspond to a steady state conductive thermal gradient based on bottom and top temperatures, as well as a hydrostatic pressure gradient based on a top boundary value of $10^7$ $[Pa]$.

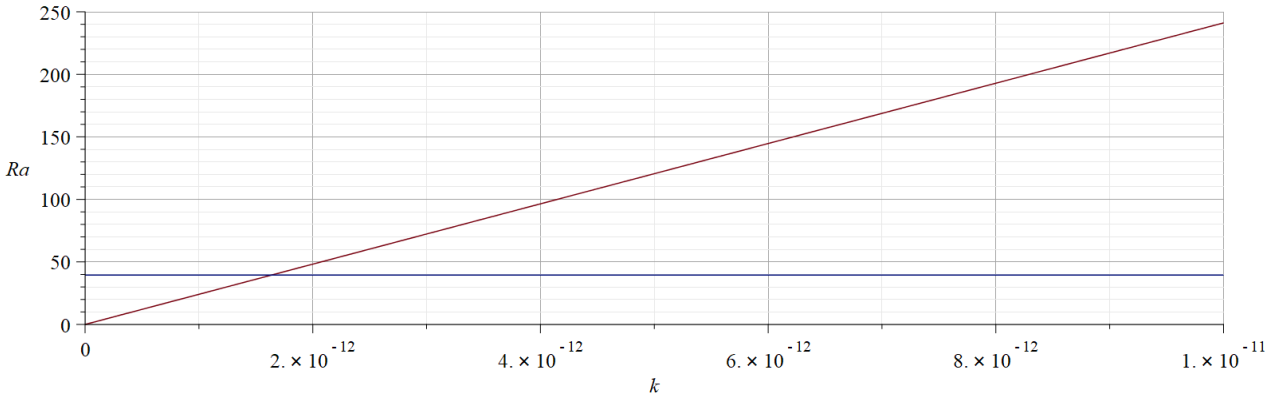


**Figure 2-18: Rayleigh number vs permeability plot (red line). The blue line shows the critical Rayleigh number under which the onset of convection should theoretically[17] not be possible. The corresponding value of permeability at the $Ra_c = 4\pi^2$ is $1.63 \cdot 10^{-12}$ $[m^2]$.**

Simulation meshes should follow a regular pattern, as shown in Figure 2-19. Grid cells are cubic, and edge sizes are 5 $[m]$ for the coarse grid, and 2.5 $[m]$ for the fine grid.

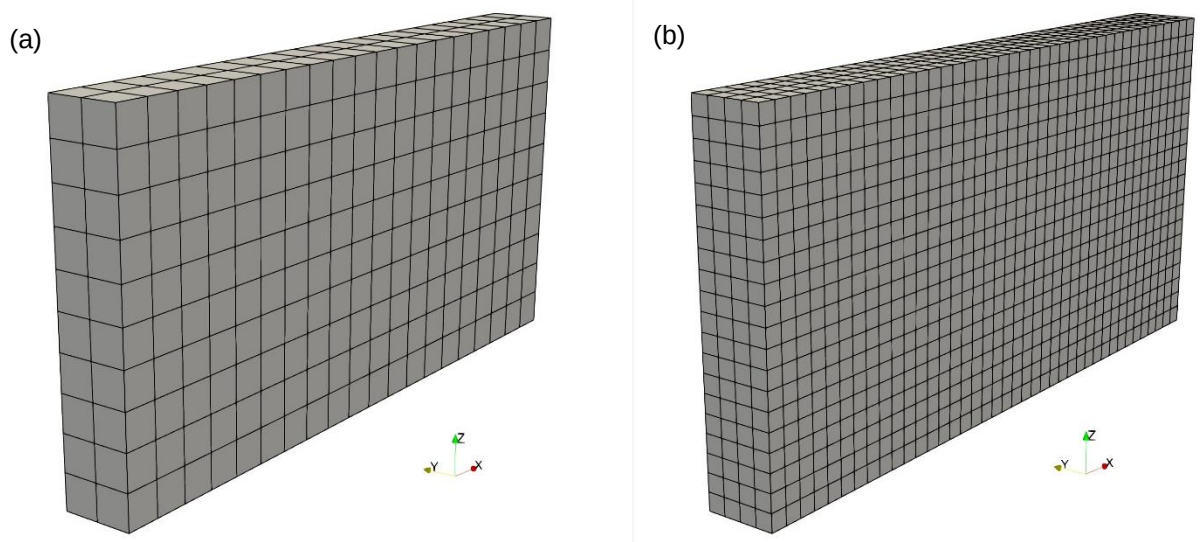


**Figure 2-19: (a) Coarse grid and (b) refined grid used in the convection tests.**

[17] This number is calculated from linear stability analysis of the problem, assuming a linear variation of density with temperature. In practice, due to conditions far from ideal, estimating $Ra$ could prove challenging.

### 2.6.3 Detailed Problem Specification

Fluid and porous medium (i.e. rock) thermal properties, including a full compiled list of parameters to be used in the simulations is provided in Table 2-15. It is important to highlight that a pure $H_2O$ equation of state is to be used in the simulations, in contrast to a typical Boussinesq linearization.

**Table 2-15: Simulation input specification.**

| Parameter | Value |
|---|---|
| **Fluid properties ( $\rho_f$, $\mu_f$, $\beta_f$, $c_{p,f}$ )** | Functions of $p, T$ |
| **Water Thermal conductivity ( $\lambda_f$ )** (assumed constant) | $0.65\ \left[\frac{W}{m\cdot°K}\right]$ |
| **Rock Porosity ( $\phi$ )** | $0.1\ [-]$ |
| **Rock Permeability ( $k$ )** (three possible values) | $2\cdot10^{-12},\quad 5\cdot10^{-12},\quad 1\cdot10^{-11}\ [m^2]$ |
| **Rock density ( $\rho_r$ )** | $2400\ \left[\frac{Kg}{m^3}\right]$ |
| **Rock Thermal Conductivity ( $\lambda_r$ )** | $2.275\ \left[\frac{W}{m\cdot°K}\right]$ |
| **Rock Specific Heat Capacity ( $c_{p,r}$ )** | $860.2\ \left[\frac{J}{Kg\cdot°K}\right]$ |
| **Top Temperature ( Cold, $T_C$ )** | 20 ℃ |
| **Bottom Temperature ( Hot, $T_H$ )** | 80 ℃ |
| **Simulation end time ( $t_{end}$ )** | $1000\ [yrs]$ |
| **Output times (three)** | $10,\ 10^2,\ 10^3\ [yrs]$ |
| **Mesh spacing (cubic cells)** (two values) | $5\ [m],\quad 2.5\ [m]$ |
| **Domain height, length, width ( $H, L, W$ )** | $50\ [m], 100\ [m], 10\ [m]$ |
| **Initial pressure ( $p_{res}$ )** | Hydrostatic conditions, top at $10^7\ [Pa]$ |

Given the structured nature of the mesh, it is very possible that the initial conditions represent a stable solution to the problem. For this reason, initial conditions should possess a slight perturbation in the temperature field, namely in the form of a $0.125\ \%$ linear variation of the bottom temperature boundary condition:

$$T_{Bottom}(x) = T_H + \frac{x}{1000} \tag{2-27}$$

Following initialization, the bottom boundary temperature condition should be returned to its constant value of $T_H$.

### 2.6.4 Output Specification

All six simulations (i.e. two meshes, three permeabilities) should report a collection of snapshots of the temperature field as well as a separate plot of a collection of streamlines including the outline of the domain, as a reference. The snapshots should be reported via JPEG files (i.e. .jpg, or .jpeg file extension is assumed equivalent):

1. `test4_temperature_lowperm_coarse_NAME_#.jpg`
2. `test4_temperature_medperm_coarse_NAME_#.jpg`
3. `test4_temperature_highperm_coarse_NAME_#.jpg`
4. `test4_streamlines_lowperm_coarse_NAME_#.jpg`
5. `test4_streamlines_medperm_coarse_NAME_#.jpg`
6. `test4_streamlines_highperm_coarse_NAME_#.jpg`
7. `test4_temperature_lowperm_fine_NAME_#.jpg`
8. `test4_temperature_medperm_fine_NAME_#.jpg`
9. `test4_temperature_highperm_fine_NAME_#.jpg`
10. `test4_streamlines_lowperm_fine_NAME_#.jpg`
11. `test4_streamlines_medperm_fine_NAME_#.jpg`
12. `test4_streamlines_highperm_fine_NAME_#.jpg`

As with the other tests mentioned in this report, NAME in the input file should be replaced with the full name of the author of the test result as well as the institution (e.g. “JulianMindel_ETHZ”). The “#” should be replaced with the output time number $10$, $100$, and $1000$, when appropriate. This should equate to a total of 36 JPEG files.

Snapshots should possess the following characteristics:

1. Reasonable resolution (e.g $1920 \cdot 1200$ pixels or better) JPEG of high quality, with most of the visualization area occupied by the simulated domain.
2. Background colour should be white.
3. The temperature colour code should follow rainbow characteristics (blue/cold, through green and yellow, to red/hot, see Figure 2-20). A legend should be provided.
4. Temperature colour legend and contours should contain 6 colour levels (i.e. every $10℃$ from $20℃$ to $80℃$). The contours should be delineated by a thin black line.
5. Grid should be visualized easily through temperature contours (via thin black lines)
6. There should be enough streamlines to be able to clearly count the number of Bernard cells present in the domain.

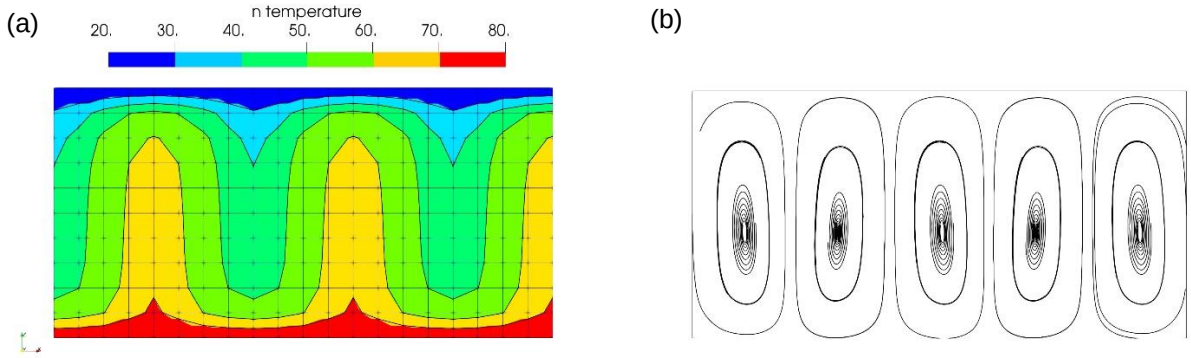


**Figure 2-20: Sample snapshots for the coarse grid simulation with $k = 10^{-11}$. (a) Temperature contours, depicting six colour levels demarcated with thin black edges. (b) Streamlines, shown in black, inside the outline of the modelled domain.**

Finally, and as also required by the other tests, information should be provided via a separate text file “`test4_sys_application_info_NAME.txt`” regarding the simulator, compiler, compiler version, operating system, the CPU used and memory available, parallel capabilities used (e.g. CUDA, MPI, OpenMP), and mesh information. The table format and sample information was provided in Table 2-6 for the analytical transient pressure verification test. For this test, additional details should be provided regarding the solution algorithm sequence used, particularly for the heat transport approach, as well as the formulation (e.g. Finite Elements, Finite Volumes, decoupled fluid-rock heat equations, single coupled heat equation, .etc.) in the comments section. An example of this text file is given by “`test4_sys_application_info_EXAMPLE.txt`” in the data bundle provided with this report. Examples of the snapshots are also provided via:

- "test4_temperature_highperm_coarse_EXAMPLE_1000.jpeg"
- "test4_streamlines_highperm_coarse_EXAMPLE_1000.jpeg"

### 2.6.5 Results

The focus of this test is on determining and comparing the thermal-buoyancy modelling capabilities of simulators. With the exception of COMSOL (BRGM) and Eclipse100, all simulators were able to carry out this test. Reportedly, COMSOL was not able to converge on any of the simulations set out by this test regardless of the permeability values or mesh grade used. Eclipse100 on the other hand is also reportedly incapable of modelling buoyancy whilst using an equation of state such as the one defined by the IAPWS due to its formulation. The latter does not include a true energy equation and simply mimics hydrothermal flow via the numerical transport of a passive tracer field.

Assuming that the setup/configuration for all simulators were peformed accurately, all 8 succesful ones were able to produce some form of steady state at 1000 [yrs] for all 6 simulations, with one minor exception from MOOSE, for which solution convergence was not achieved for the high permeability, fine mesh case.

The type of problem presented by this test has been studied for decades, and it remains challenging in all its simplicity. As can be observed from the extended summary of simulators presented in section 7.5 Appendix E: TH Benchmark 1 - Test 4 results, for the same mesh and equivalent permeability, some simulators display a disturbance in their temperature fields earlier than others. As further observed in an extract of early (i.e. *t = 10[yrs]*) results presented in Figure 2-21, while streamlines may exist at a very early stage, velocity magnitudes may vary. The latter is particularly exhibited by the level of perturbation of the temperature field. It is thus reasonable to assume that some simulators will reach a steady state earlier than others, and that 1000 [yrs] is sufficient time for the least permeable of cases.

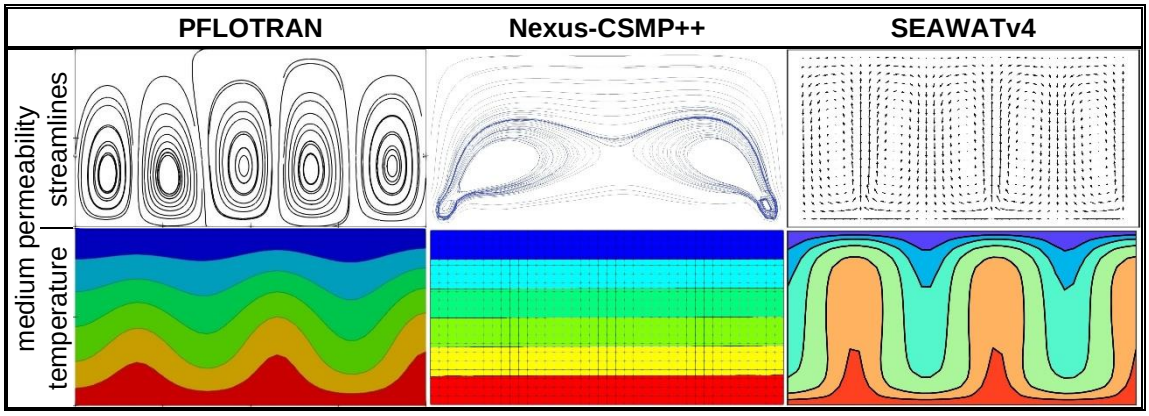


**Figure 2-21: Cross-simulator comparison depicting coarse-mesh snapshots of streamlines and temperature contours at time level t=10 [yrs] for PFLOTRAN, Nexus-CSMP++, and SEAWATv4.**

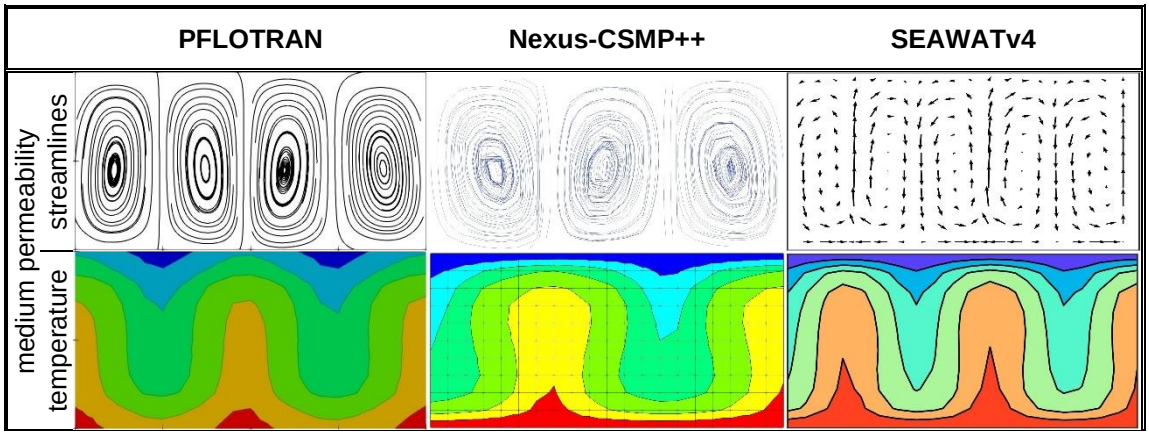


**Figure 2-22: Cross-simulator comparison depicting coarse-mesh snapshots of streamlines and temperature contours at time level t=1000 [yrs] for PFLOTRAN, Nexus-CSMP++, and SEAWATv4.**

As observed in Figure 2-22, some simulators may reach a different number of RB cells. Studying the fullly detailed rationale behind this is beyond the scope of this report, however in principle it can be assumed that it pertains to at least the following reasons, in decreasing order of importance:

1. The particular formulation, numerical discretization, and solution process of each simulator. Coupled to the non-linear aspect of the problem, these likely have an impact on the level of numerical diffusion in both space and time, and may thus tend to either attenuate or even occasionally strengthen instabilities. As observed in
2. Figure 2-21 for the SEAWATv4 and PFLOTRAN simulators, the flow field is strong enough already at $t = 10\ [yrs]$ to significantly affect the temperature field.
3. The level of initial perturbation. It was not verified whether all simulators were able to properly and uniformly implement equation (2-27).

**Table 2-16: Summary of observed number of RB cells at $t = 1000\ [yrs]$.**

| Simulator | Spatial Disc. Method | Time Disc. Method | low permeability | | medium permeability | | high permeability | |
|---|---|---|---|---|---|---|---|---|
| | | | coarse | fine | coarse | fine | coarse | fine |
| MARTHE | FV | EI | 3 | 3 | 4 | 4 | 5 | 6 |
| COMPASS | FV | EI | 2 | 2 | 4 | 3 | 5 | 3 |
| Nexus-CSMP++ | Hybrid FE-FV | PE | 3 | 3 | 3 | 3 | 3 | 3 |
| MOOSE | FE | EI | 3 | 3 | 3 | 6 | 4 | X |
| SEAWATv4 | FD | SD | 3 | 3 | 5 | 5 | 5 | 5 |
| CODE_BRIGHT | FE | EI | 2 | 2 | 3 | 3 | 4 | 3 |
| Tough3 | IFD | EI | 3 | 3 | 6 | 5 | 5 | 6 |
| PFLOTRAN | FV | EI | 3 | 3 | 4 | 5 | 4 | 6 |
| | | **Average** | **3** | **3** | **4** | **4** | **4** | **5** |

SD = Solver Depedent
EI = Euler Implicit
PE = Pseudo Explicit
FD = Finite Differences
IFD = Integrated Finite Differences
FV = Finite Volumes
FE = Finite Elements

A summary of achieved RB cells per simulation case and simulator is presented in Table 2-16. A rounded average is presented, displaying a value of 3 for the low permeability cases, 4 for the medium permeability cases, 4 for the high permeability coarse case and 5 for the high permeability fine case. These values show quite clearly that there is, as expected, a general tendency for increase in the number of RB cells with

increasing permeability. This is also true to a lesser extent for decreasing mesh-cell size. Nevertheless, some simulator results are more sensitive to permeability and mesh grade values than others. Nexus-CSMP++ displays an even 3 cells throughout all 6 simulations, while other simulators like MOOSE change from 3 to 6 for medium permeability. Although not a definitive statement, it should be noted from Table 2-16 that simulators utilizing FD and FV methods tend to be more sensitive to the increase in permeability than those possessing at least some FE aspect (i.e. a notable exception to this observation is MOOSE). In a similar light, nearly all simulators displaying sensitivity to the permeability and mesh cell size values utilize an Euler Implicit (EI) approach to timestepping, while the only simulator that uses explicit timestepping (i.e. Nexus-CSMP++) does not. Further tests with current (or other) simulators set to utlize explicit timestepping should be carried out to allow further investigation of whether time discretization approach is an important factor.

Due to the non-linear characteristic of the fluid flow assumptions in the problem posed by this test, predicting the number of RB cells is a difficult task. Approaches exist, however they typically rely on a linear stability analysis under Boussinesq considerations for density. While performing such an estimate may have provided an approximate idea for a steady state number, this test was not designed to assess the ability of simulators to predict a theoretical number of RB cells in a rectangular enclosure. Given that such an exercise would have proven elusive, and ultimately meaningless due to the difference in flow assumptions, the current focus was to test and observe the capabilities of simulators to model thermal convection, as well as compare the values obtained at particular time levels. As shown with some degree of variation, results were within reasonable agreement. The latter is particularly true for the simulations that used low permeability value (i.e. $k = 2 \cdot 10^{-12}[m^2]$) , as this likely brings flow conditions closest to the Darcy assumptions for which most of the participating simulators were designed.

## 2.7 Conclusions

A TH modelling benchmark exercise was carried out by 7 teams, which comprised up to 10 simulators. Within the exercise, tests included an analytical transient pressure test (test1), a complex well-testing model test (test2), an experimental heat transport validation test (test3), and a convection test (test4). The intended design of the benchmark was thus to express and verify the different capabilities of simulators available to the HEATSTORE project from a comparative accuracy point of view, and not timed performance. Although ultimately possible, setting up a fairly timed benchmark would have proved logistically challenging, given the perceived challenge already presented at times by the data-exchange needed for accuracy comparisons.

The first test (test1) focused on the hydrological (H) aspect of flow in saturated porous media, and although with a slight issue for Eclipse100 (GEUS), it was successfully carried out by all 10 simulators. Since test1 possessed a well-defined analytical solution, accuracy was clearly shown to be a concern for most simulators. Particularly in early simulated times and measured at close proximity to the well (i.e. essentially at the well face), simulators showed up to ~50% error on the coarse mesh case and ~25% error on the fine mesh case. This error diminished relatively quickly with time. Levels of error decreased systematically for most simulators with elapsed time and distance. In a rather unintentional show of fairness, and with a few exceptions, simulators did not rank systematically in terms of error at a particular probe with elapsed time for a particular mesh case.

The second test (test2) concentrated on both thermal and hydrological aspects (TH) while reproducing typical phases of well tests (i.e. Injection, Fall-off, Drawdown, Build-up). These phases were assembled into an artificial sequence that was reproduced by all simulators to a varying level of completion. Scenarios for this test included three possibilities: a homogenous reservoir (variant 1), a reservoir with a reef structure centered on the well location (variant 2), and a reservoir with a single fracture in relative close proximity to the well (variant 3). Furthermore, complexity in this test was increased by adding two different types of meshes: a radial mesh and a coarse mesh. All simulators were capable of performing both variant 1 and variant 2 with at least one type of mesh (i.e. COMSOL did not succeed with a cartesian mesh, and Eclipse100 did not succeed with a radial mesh). As rather expected, variant 3 proved to be the most challenging variant, where 5 out of 10 were capable of performing it with the radial mesh, and 8 out of 10 with the Cartesian mesh. Due to its non-linear conditions, this test does not possess an analytical solution. Nevertheless, most simulators performed within reasonable agreement with one another, with some minor sporadic outliers evidencing a fixed temperature condition at the well during injection (i.e. MOOSE, Tough3),

some exceptional asymmetries between the minimum and maximum pressure changes (i.e. MOOSE), pressure response delays (i.e. CODE_BRIGHT), and temperature response delays (i.e. Nexus-CSMP++). Given the wide range of capabilities (i.e. or lack thereof) in the participating simulators, and the ever-present possibility of human error, these outlying events are minor enough to not represent “incorrect” results, but to merit further study with respect to the underlying reason.

The third test (test3) consisted of a unidimensional hydrothermal (TH) experimental comparison focusing mainly of thermal transport aspect while utilizing a fixed flow velocity. With some minor issues regarding the read-in of boundary condition input signals (i.e. COMSOL, Eclipse100), all simulators were able to carry out this benchmark, which included two different types of porous media: one composed by a tube of glass spheres, and another with steel spheres. Results produced by most simulators were fairly accurate and with very good inter-agreement, with only two exceptional outliers (i.e. Tough3, Eclipse100). Discrepancy of the results produced by most simulators displays a generalized speedup of the thermal front, which can be most likely attributed to the modelling of the tube walls as adiabatic. An out-of-scope level of conductivity imposed in the tube walls would most likely have delayed the thermal front enough to reproduce the experimental results more accurately. Nevertheless, the error observed at the probe point furthest away from the inlet (i.e. PROBE_3) did not exceed ~21% for the glass spheres case, and ~7% for the steel spheres case (i.e. not including the outliers mentioned). The results from Tough3 and Eclipse100 presented for this test displayed an excessive level of diffusion, as well as a disproportionate time delay. Given the relative simplicity of the test, these displays are most likely due to an incorrect setup of tube wall boundary conditions and/or diffusion/dispersion coefficients.

The fourth test (test4) consisted of a three dimensional hydrothermal problem (TH) posed by prismatic impermeable enclosure containing a saturated porous medium. Also known as the Horton-Rogers-Lapwood (HRL) problem, this test contrasts from test3 mainly via the increasing importance of ensuing gravitational effects. It is thus aimed at modelling thermal convection, which is triggered by its boundary conditions and deliberately-uneven initial conditions. Given the prescribed values of permeability and other medium material properties, onset of convection is essentially ensured, and this is further studied by allowing two levels of resolutions to be tested (i.e. a coarse, and a fine mesh). Non-linearity exists mainly due to the prescribed usage of the IAPWS standard for water properties, and an analytical prediction of the stable number of Rayleigh–Bénard (RB) cells may thus not be easily estimated. Still, it was the aim of this test to compare capabilities and evaluate how sensitive simulators are to the imposed boundary conditions and material properties. Nearly all simulators were capable of performing all 6 simulation tasks required by this test, with notable exceptions for COMSOL and Eclipse100. Reportedly, COMSOL failed to converge in all 6 simulations, while Eclipse100 was not designed to accurately model convection using a full equation of state. All simulators reported characteristic thermal convection, a relatively consistent behaviour, and a varying level of sensitivity to the increasing value of permeability, with the exception of Nexus-CSMP++. For the latter, the main difference in comparison to other simulators is the usage of a pseudo-explicit approach to its time discretization. This does not imply a straightforward reason, but rather that this test should be carried out by other simulators with explicit time-stepping to obtain a better perspective.

Nearly all simulators have shown reasonable accuracy performance in all the TH-related tests provided by this benchmark. The main issues with those simulators that did not submit results for a particular test, or submitted an incomplete result set likely resided in the lack of a particular feature/capability or knowledge support to activate it, as well as a degree of inflexibility or “black box” behaviour of some commercial simulators. These features/capabilities included the ability to interpolate values to assigned monitoring probe points (i.e. Eclipse100, test1), usage of different mesh types (i.e. radial and cartesian, particularly for COMSOL and Eclipse100 in test2), injection temperature setting (i.e. Tough3 and MOOSE in test2), the modelling of fractures (i.e. PFLOTRAN in test2), modelling of buoyancy (i.e. COMSOL and Eclipse100 in test4), and solver control (i.e. COMSOL, test4).

Overall, when considering the varying complexity of the tests, the number of teams and simulators involved, and the high level of feedback and communication provided by many of the individual participants, a more-than-sizeable level of completion has been achieved by this benchmark. This comparison exercise clearly shows that there are quite a number of very flexible simulators capable of performing all basic-yet-essential TH calculations at a comparatively equal level of accuracy.

# 3 TH benchmark 2 (proposed by Virginie Hamm, BRGM)

## 3.1 Introduction

This benchmark is part of the GEOSTOCAL research project “GEO-STOckage de ChALeur” (2007-2011) that was funded by the “Agence Nationale de la Recherche” (ANR) under BRGM coordination. The project included various components (modeling of the hydrothermal and geochemical behavior of the reservoir under HT storage conditions, energy modeling...) on the feasibility of a seasonal heat storage system in the Dogger limestone aquifer in the commune of Ivry-sur-Seine (South-East of Paris).
The deep aquifer inter-seasonal heat storage system envisaged was based on a set of 2, 3 or 4 wells for injection and / or pumping (see Figure 3-1), in order to store excess heat (waste energy from an incineration plant) during the summer period and then to recover it during the heating demand period. The storage-recovery sequence is periodic with a 12-month cycle. During this period, the reversible well(s) is (are) operated alternately in injection and pumping.

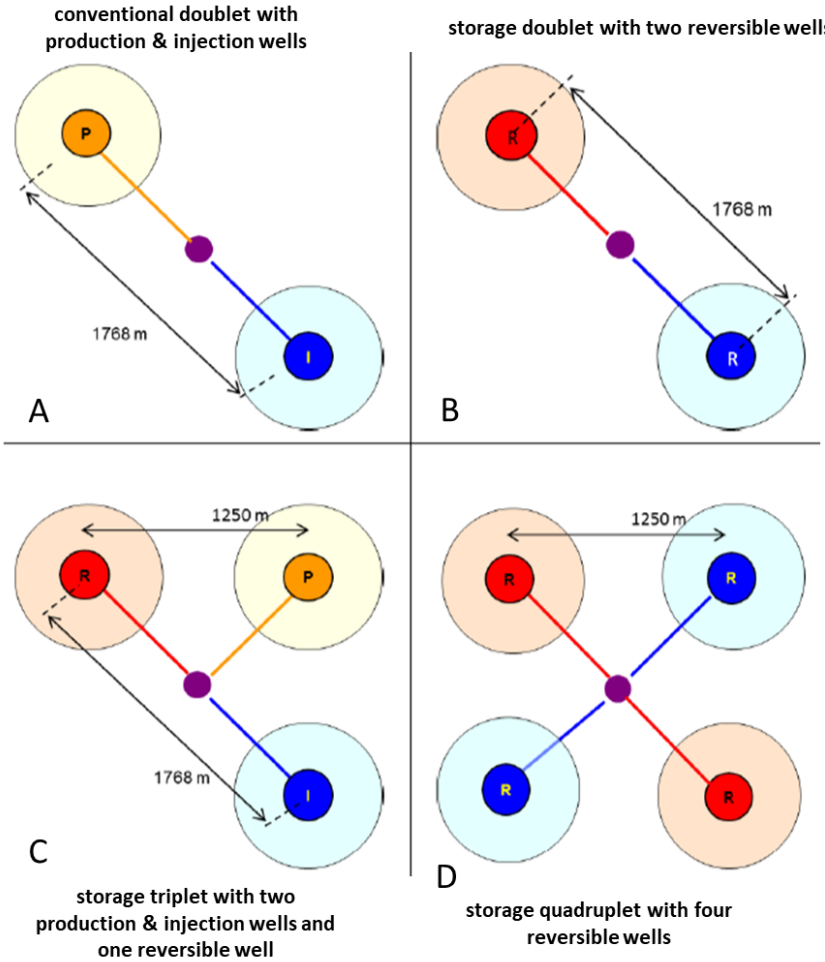


**Figure 3-1: Different schemes of wells for HT-ATES.**

For the benchmark we propose to focus on one configuration that was published in Reveillera et al., (2013).

This ATES system produces a hot plume in the reservoir around the hot storage well during the summer period (hot well operates as an injector and the cold well as a producer, Figure 3-2A) and a cold plume around the cold storage well during the winter period (hot well operates as a producer and the cold well as an injector).

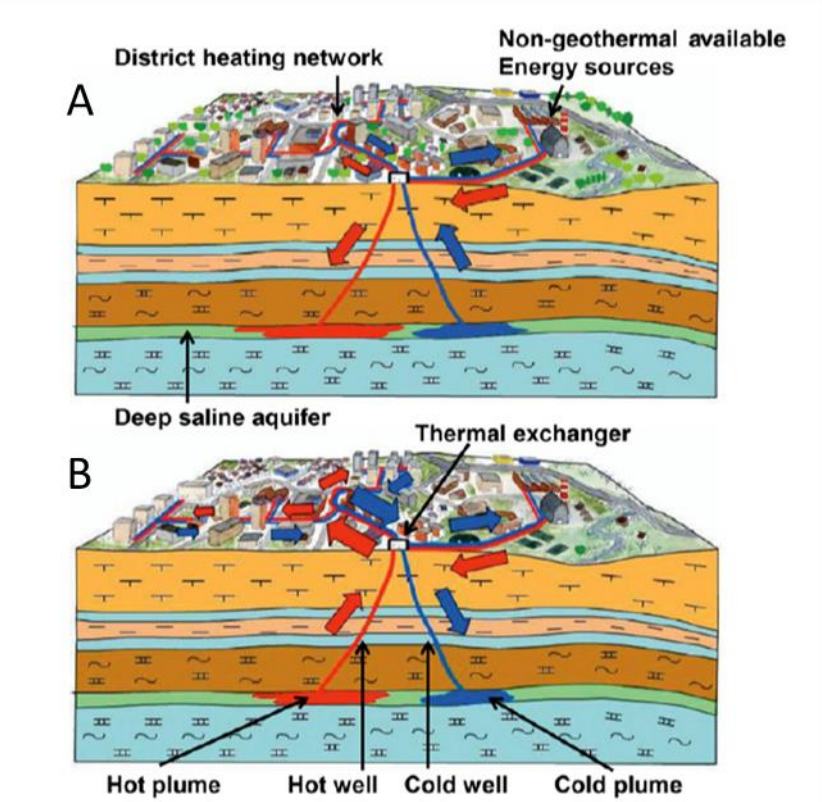


**Figure 3-2: Schematic representation of the ATES concept (top panel: summer storage, bottom panel: winter unloading).**

The ATES system was simulated for a total of 30 one-year cycles each consisting of:

- 14 weeks of hot water storage at a constant flow rate of 300 $m^3/h$ and temperature of 95 °C; this also induces water unloading at the cold well;
- 34 weeks of hot water unloading at varying flow rates and temperatures, the average flow rate was 242 $m^3/h$ and the average injection temperature at the “cold well” was 46.1 °C;
- 2 weeks pause at the end of each period.

These baseline operating conditions maximizes the use of geothermal energy on the heating network. This ATES operates with an unbalanced mass flow rate which results in an average annual overall flow of 80 $m^3/h$ from the hot well to the cold well.
Two teams were implied in this benchmark: BRGM, who proposed the benchmark case, by using Marthe simulator and Storengy by using Tough3 simulator.

## 3.2 Participating teams and codes

*MARTHE (BRGM)*
MARTHE software package is a hydrothermal reservoir simulator designed and developed by BRGM (Thiéry D., 2004, 2012, 2015). The software can be used for modeling steady and non-steady state conditions, one, two or three dimensional geometry or multi-layered aquifers. It can be used for saturated and unsaturated conditions and can solve the mass or heat transport fully coupled with hydraulic calculation in porous media.
The hydrodynamic calculations are carried out by a finite volumes algorithm with a purely implicit method by establishing the flow equilibrium equations between the calculation mesh and the six adjoining meshes (North, South, East, West, Top and Bottom). Several conjugate gradients schemes (Choleski pre-conditioning, Eisenstat pre-conditioning, Geometric Multi-Grid pre-conditioning) are proposed. For the transport calculation the user can choose among different calculations techniques, according to the type of problem encountered

(predominance of convection or dispersion) to optimize the transport model to be used. Those methods are TVD method (Total Variation Diminishing) with flux limiter, Finite Difference method, Method of Characteristics (MOC) and Random Walk method with particles displacement. Transport in the aquifer considers advective (convection), diffusive (conduction) and dispersive components.

The modelled domain is discretized as a rectangular "tartan" grid: each row and each column of the grid has a constant width, but the user is free to adapt the width of each of these rows and columns so as to fit local heterogeneities, the amount of available data and the desired accuracy. It is also possible to create locally finer cells using fully coupled nested sub-grids. Grid data may be defined on a cell basis, or on a “zone” basis, on a layer basis, or globally for the whole grid.

Different boundary and initial conditions can be applied (constant or variable hydraulic head, concentration or temperature, constant or variable flux, river condition). The resulting hydraulic head, concentration or temperature are calculated in the centers of each cell of the model at any time step.
In the case of impervious layers with very large thicknesses (“hanging wall”) at the top and bottom of the reservoir, MARTHE allows to use the method of Vinsome and Westerveld (1980) to perform the calculation much more quickly. This method uses an approximate analytical solution which is based on the assumption that the heat transfer between the impervious wall and the aquifer is predominantly perpendicular to the aquifer and only by conduction. The analytical method involves a single layer of impervious wall on each side of the aquifer and avoids a fine discretization of the impervious layer. It is thus possible to considerably reduce the number of meshes (the number of layers) to simulate the impervious layers, almost without loss of precision. The calculation therefore requires much less memory and is much faster. This particular feature was used in the benchmark model.

*TOUGH3 (Storengy)*
TOUGH3 simulator is developed for applications involving subsurface flow problems. It can be used for saturated and unsaturated conditions and can solves mass and energy balance equation that describe fluid and heat flow in general multiphase, multicomponent fluid mixtures and multidimensional system in porous and fractured media.
TOUGH3 use an integral finite difference method (IFDM) for space discretization. The IFDM (Edwards, 1972; Narasimhan and Witherspoon 1976) offers the advantage of being applicable to regular or irregular discretization in one, two and three dimensions. TOUGH3 includes one direct solver LUBAND and four iterative solvers DSLUBC, DSLUCS, DSLUGM and DLUSTB. By default TOUGH3 uses DSLUCS with incomplete LU-factorization as preconditioner for serial runs. Heat flow occur by conduction and convection as well as radiative transfer according to the Stefan -Boltzmann equation.

Different boundary and initial conditions can be applied (constant or variable pression, concentration or temperature, constant or variable flux, river condition). The resulting pression, concentration or temperature are calculated in the centers of each cell of the model at any time step.
In the case of impervious layers with very large thicknesses (“hanging wall”) at the top and bottom of the reservoir, TOUGH3 also allows to use the method of Vinsome and Westerveld (1980) to perform the calculation much more quickly.

## 3.3 Problem description

### 3.3.1 Domain definition and temporal description

The geometrical support of the HT-ATES model is a multi-layered model representing the upper half-space according to z (half-aquifer and top impervious hanging wall, Figure 3-3). The total extension is 11 km x 11 km in x-y directions and 5.2 m in z direction. The aquifer is assumed homogenous and isotropic. The vertical discretization according to z includes an "infinite" impervious layer that can be modelled by a semi-analytical approach (Vinsome and Westerveld solution) and 4 layers of progressive thickness (0.2 m, 0.6 m, 1.2 m and 3 m) for the half-aquifer. These layers are refined closer to the cap rock, where sharper temperature gradients are expected. The material is the same in those layers.

For Marthe simulator, the global mesh includes 578920 hexahedral meshes with a narrower mesh around the wells (meshes of 12.5 m on a square of 4km x 4km) and meshes of 100 m beyond (see Figure 3-3).

For Tough3 simulator, the total number of cell in the 4 layers are 67600 rectangular cells with a narrower cell around the well (meshes of 12.5 m on a square of 1,375 km x 1.375 km ) and meshes of 25 m, 50 m, 100m, 500 m. It is not possible to create locally finer cells with TOUGH3, trying to have the same mesh like the BRGM did was increasing the time of the calculation for more than 1 week. That is why the narrower cell are kept only on a square of 1375 m length, following the positions of wells which are located on the opposite sides of the diagonal of a square of 1250 m length (1768 m between the wells) that is centered at X=0 and Y=0 (see Figure 3-4).

The heat storage and heat recovery was simulated for a period of 1580 weeks with a time step of one week. The heat storage occurred between weeks 23 and 36 with a constant flow rate of 300 $m^3/h$ and a constant storage temperature of 95 °C. The heat recovery occured between weeks 39 and 52 with a minimal flowrate of 65 $m^3/h$ and maximal flowrate of 300 $m^3/h$. The reinjection temperature during heat recovery varies between a minimum of 44.3 °C and 50°C.

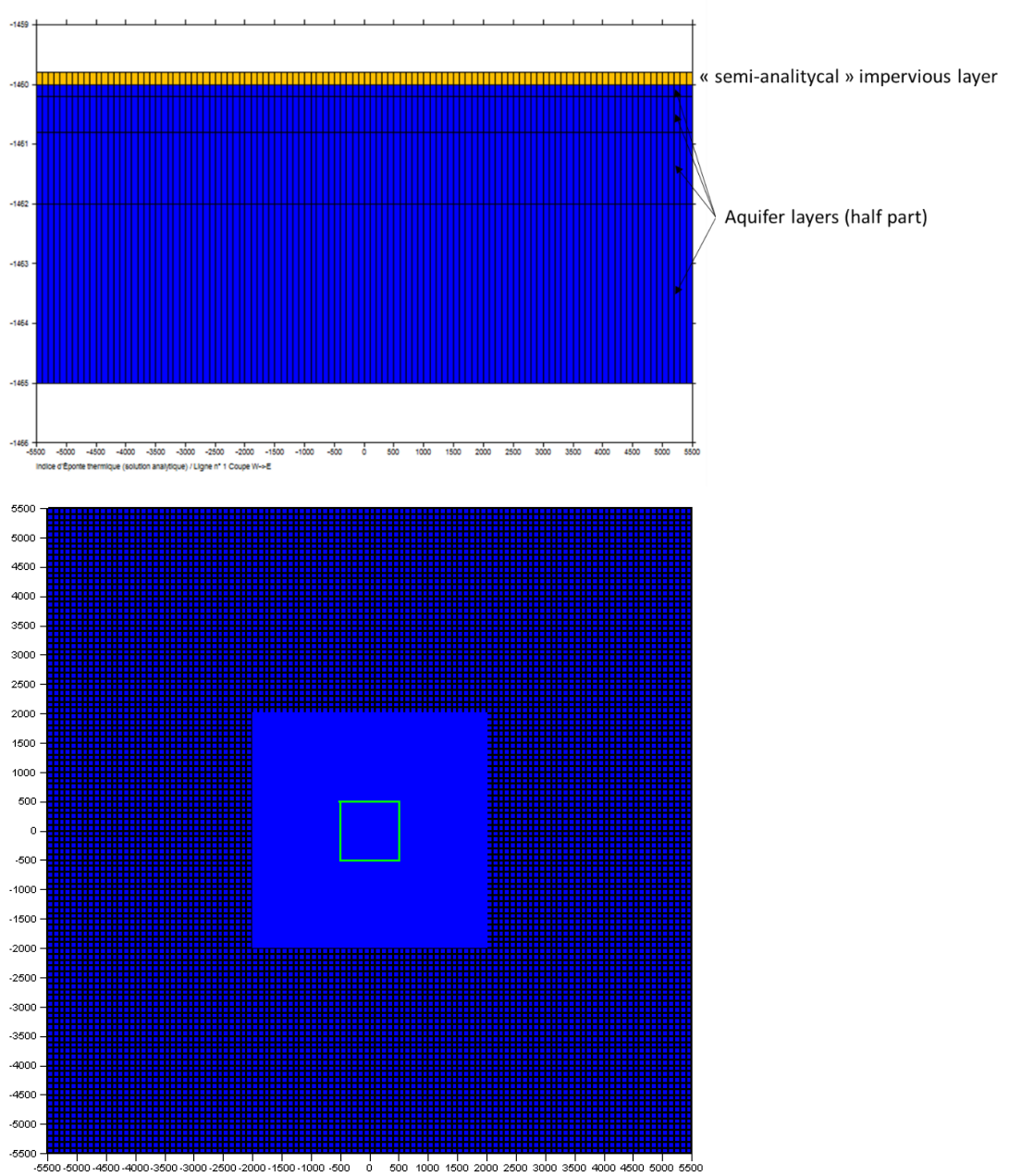


**Figure 3-3: Vertical and horizontal view of the model meshing (Marthe simulator).**

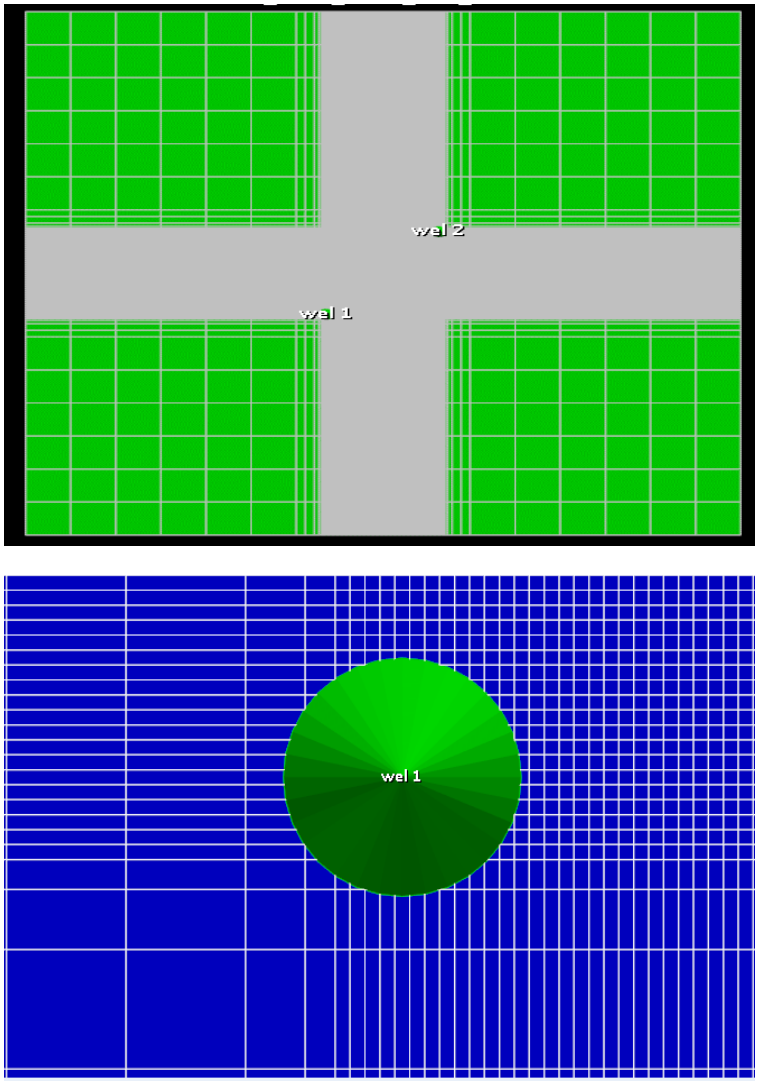


**Figure 3-4: Horizontal view (x-y plan) of the model meshing (TOUGH3 simulator).**

### 3.3.2 Material and fluid properties

The main parameters of the model including material and fluid properties are defined in Table 2-1. Those parameters are considered constant except for the fluid dynamic viscosity and density, which vary with temperature according to different laws (see Figure 3-5, Figure 3-6 and Figure 3-7) to account the changes in the hydraulic conductivity (permeability) of the fluid and therefore the hydraulic head.

**Table 3-1: Main model parameters.**

| | |
|---|---|
| **Ground level (amsl)** | 32 |
| **Average production depth (m bgl)** | 1497 |
| **Average productive thickness (m)** | 10 |
| **Intrinsic permeability (D)** | 3.5 |
| **Porosity (%)** | 15 |
| **Initial temperature (°C)** | 65 |
| **Fluid salinity (g/l)** | 19 |
| **Fluid viscosity (mPa.s) at initial temperature** | 0.44 |
| **Fluid density (kg/m3) at initial temperature** | 994 |
| **Longitudinal dispersivity (m)** | 20 |
| **Transversal dispersivity (m)** | 10 |
| **Reservoir volumic heat capacity (MJ/m3/°C)** | 2.5 |
| **Impervious layer volumic heat capacity (MJ/m3/°C)** | 2.2 |
| **Fluid volumic heat capacity (MJ/m3/°C)** | 4.166 |
| **Reservoir thermal conductivity (W/m/°C)** | 2.5 |
| **Impervious layer thermal conductivity (W/m/°C)** | 2 |
| **Fluid thermal conductivity (W/m/°C)** | 0.664 |

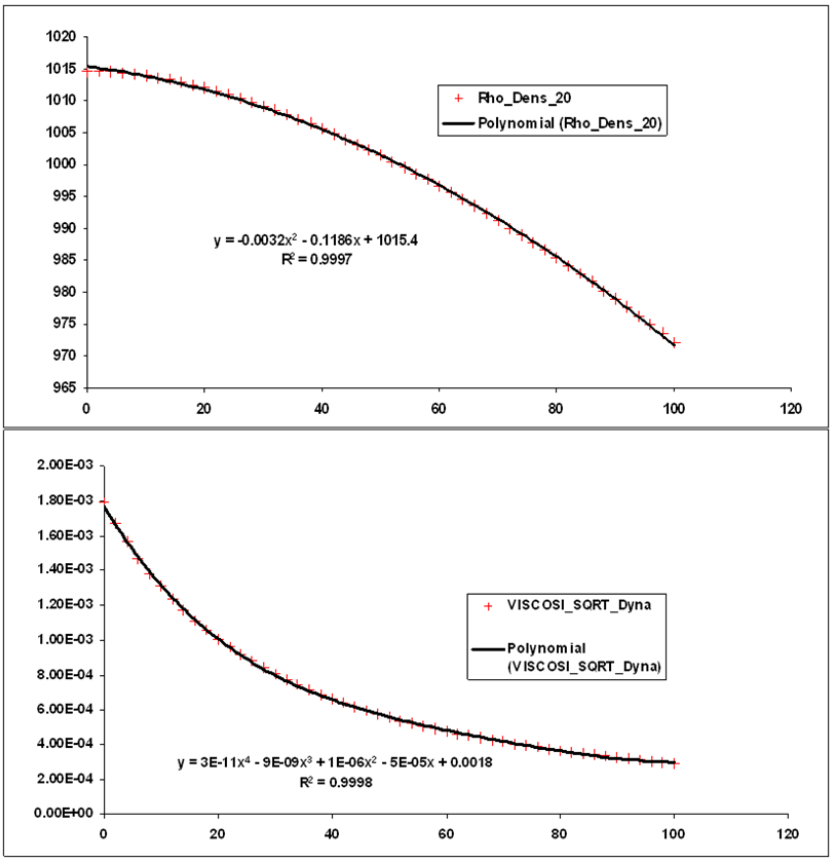


**Figure 3-5: Relationship between fluid density (kg/m3) and fluid dynamic viscosity (Pa.s) with temperature in MARTHE simulator.**

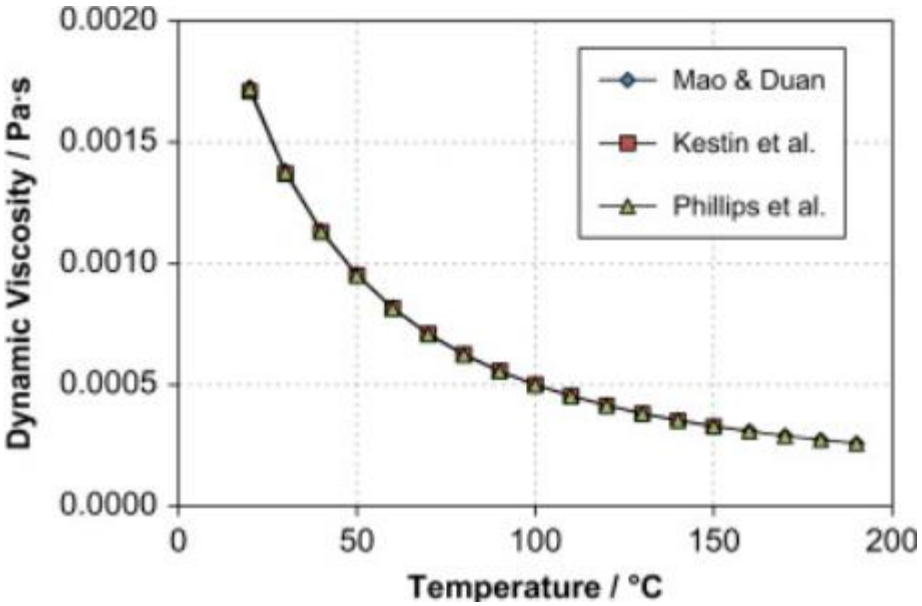


**Figure 3-6: Fluid viscosity calculation after Philips et al. (1981) used in TOUGH3 simulator.**

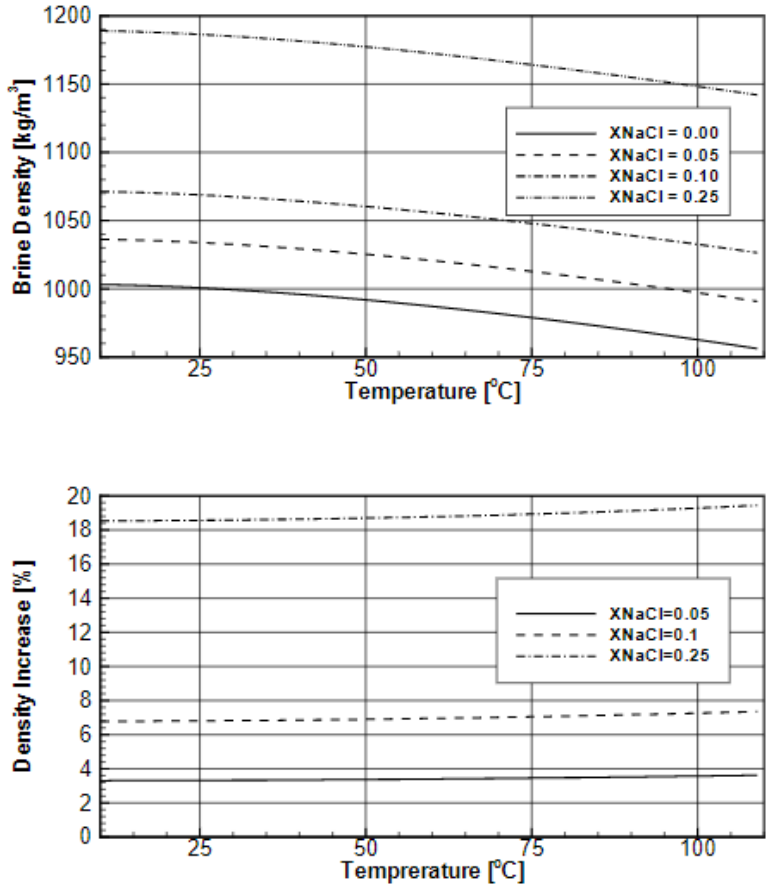


**Figure 3-7: Computed density and density increase of NaCl solutions for salt mass fraction (XNaCl) from 0 to 0.25 using the EWASG correlation (Tough3, after Battistelli et al, 1997).**

### 3.3.3 Initial and boundary conditions

The initial conditions are a fixed hydraulic head of 120 m (equivalent to an initial pressure of 158 bar) and a fixed temperature of 65°C on the entire domain.
The boundary conditions are of different types:

- fixed hydraulic head imposed at the edges of the model corresponding to the initial reservoir pressure. Therefore there is no regional underground water flow. This condition implies that fluid enters the model at the temperature of 65°C and leaves it with the temperature of the upstream cell;
- variable Hydraulic flowrates updated each time step (week) on the meshes where the pumping or injection wells are located;
- variable temperatures updated every time step on the reinjection well meshes (hot well during heat storage period and cold well during heat recovery period).

## 3.4 Results

### 3.4.1 Output specification

The variables used for the comparison between both simulators are:

1. the temperature (°C) calculated at each well (hot and cold well) every time step (week);
2. the pressure (bar) calculated at each well (hot and cold well) every time step (week);
3. the temperature profiles between the hot and cold well (temperature versus distance between wells) at the end of the $1^{th}$, $5^{th}$ , $10^{th}$ and $30^{th}$ cycles of heat storage and recovery.

### 3.4.2 Well temperature and pressure evolution

Figure 3-8 represents the average temperature at the cells intercepted by the hot and cold wells of the doublet configuration. The analysis of the temperature evolution shows that:

- The temperature at the hot well vary between 95°C at the end of storage (the hot well acts as an injector and the cold well as a producer) and 71°C (Marthe) or 69,5°C (Tough3) at the end of unloading (the hot well acts as a producer and the cold well as an injector) and after 30 cycles of seasonal storage;
- The temperature at the cold well (initially at 65°C) declines until 45°C during heat unloading process (geothermal process flow direction) and remains then below 50°C when reversing flow (during heat storage) after the $10^{th}$ cycle of seasonal storage.

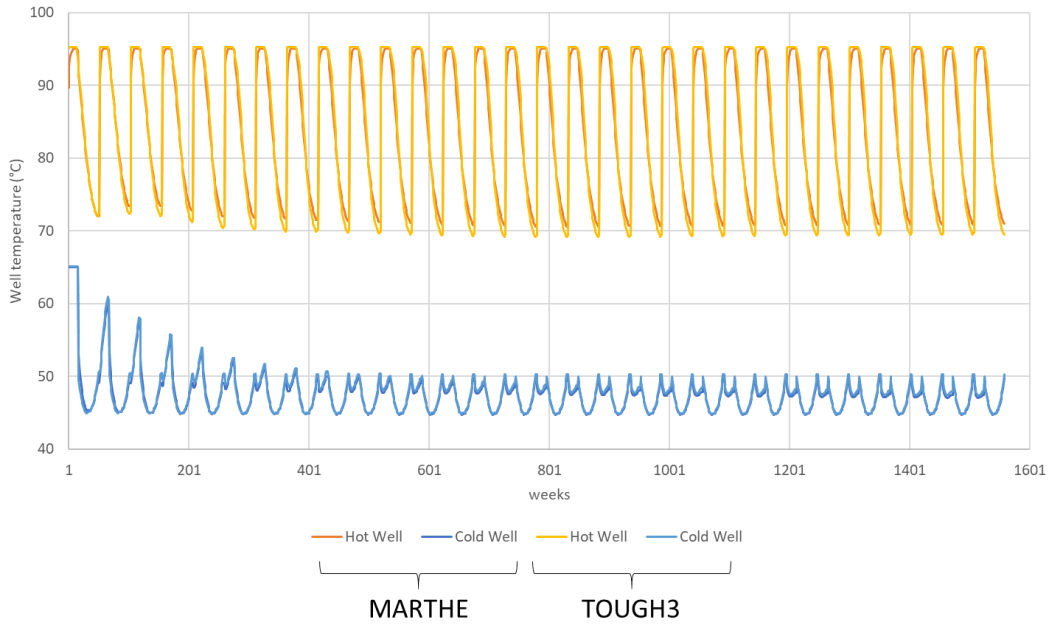


**Figure 3-8: Temperature evolution during seasonal storage cycles at the hot and cold wells.**

Figure 3-9 represents the average pressure at the cells intercepted by the hot and cold wells of the doublet configuration. The analysis of the pressure evolution shows that:

- The pressure at the hot well is close to 164 bar (Marthe simulator) or 168 bar (Tough3 simulator) at the end of storage period. This pressure then decline progressively until 146 bar (Marthe simulator) or 147 bar (Tough3 simulator) after heat unloading;
- The pressure at the cold well, is close to 145 bar during heat storage (production at the cold well) and increase until 174 bar (Marthe simulator) or 173 bar (Tough3 simulator) during heat unloading (injection at the cold well).

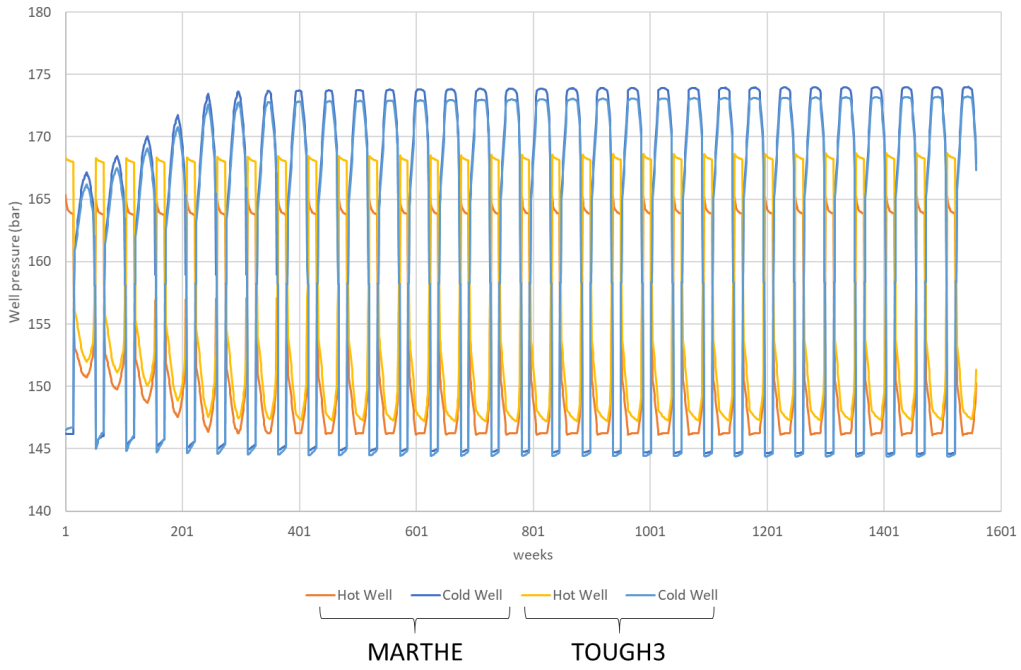


**Figure 3-9: Pressure evolution during seasonal storage cycles at the hot and cold wells.**

The results of both simulators are globally similar. Some discrepancies exist specifically for the pressure calculated at the hot well. Indeed the pressure calculated during heat storage is higher by 4 bar with Tough3 simulator comparing to Marthe simulator. The reason of this difference is difficult to fully explain at this stage. Different laws are used for viscosity and density coupling that could have a higher impact at higher temperature.

### 3.4.3 Temperature profiles between the hot and cold wells

Figure 3-10 to Figure 3-13 represent at different time scale (1th, 5th, 10th and 20th seasonal storage cycle) the temperature profile along the doublet axis linking the two reversible wells (see Figure 3-2B).
Those figures show the lateral extension of the hot and cold plumes around the reversible wells.
Since the quantity of water/heat exploited at the hot well is twice the quantity of water/heat stored, on average 1380 kton against 705 kton per cycle, the hot and cold plumes do not evolve similarly. Over successive contractions and expansions, the cold plume grows in the direction of the hot well over the cycles, similarly to the development around the injector well in a conventional geothermal doublet. The cold plume, defined as the region where the temperature decrease exceeds 1°C, does not reach the hot plume during the 30 years of ATES operating.

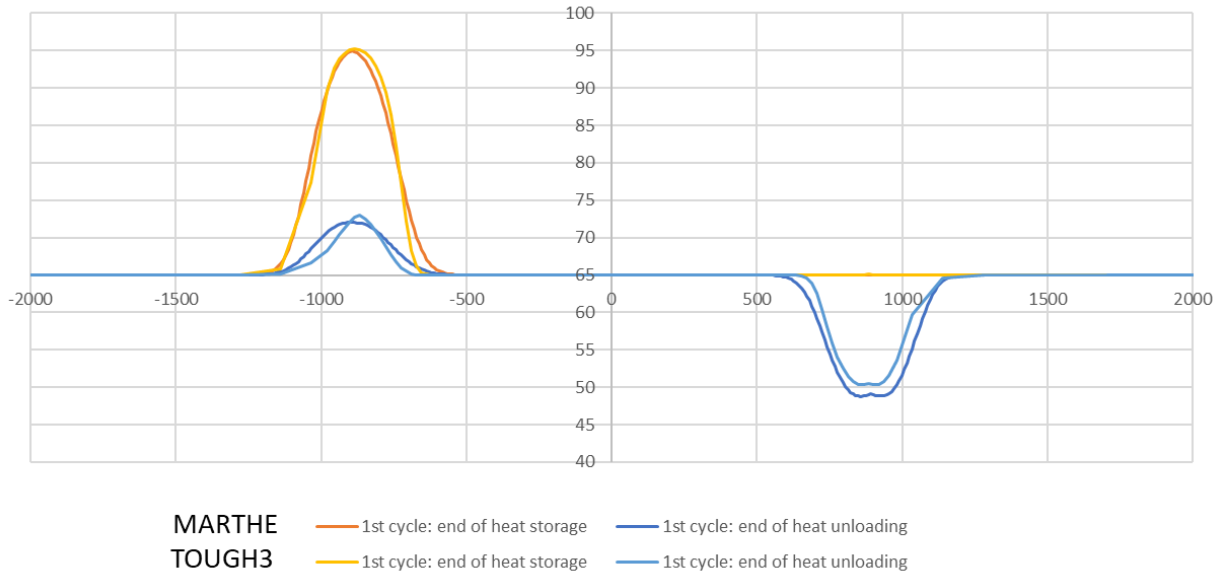


**Figure 3-10: Temperature profile between the hot (left) and cold (right) wells: end of 1st cycle of storage and unloading.**

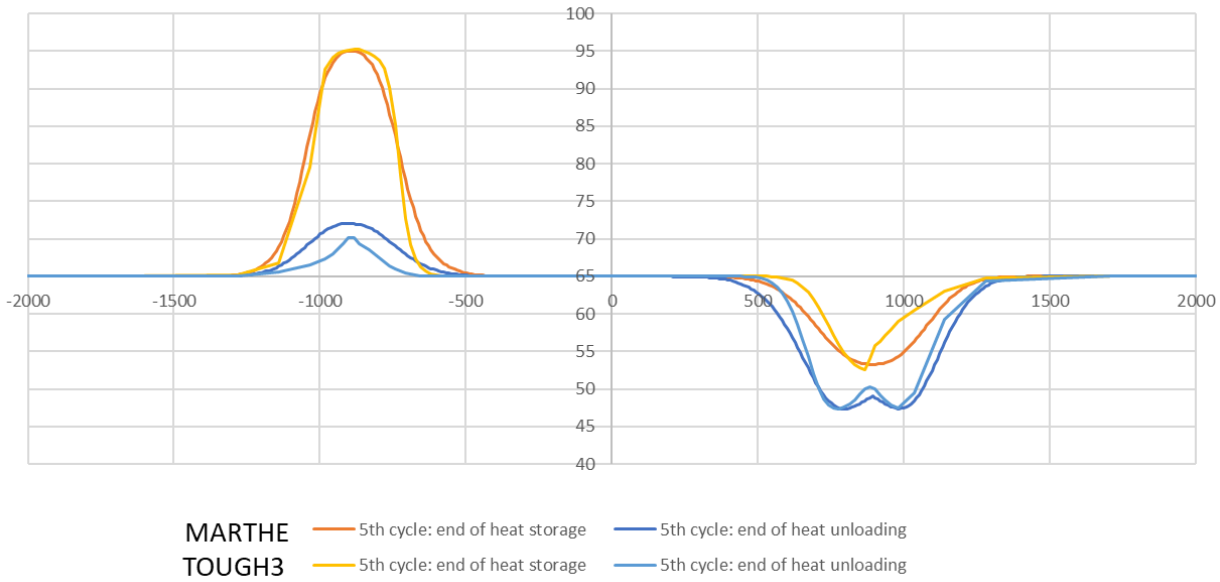


**Figure 3-11: Temperature profile between the hot (left) and cold (right) wells: end of 5th cycle of storage and unloading.**

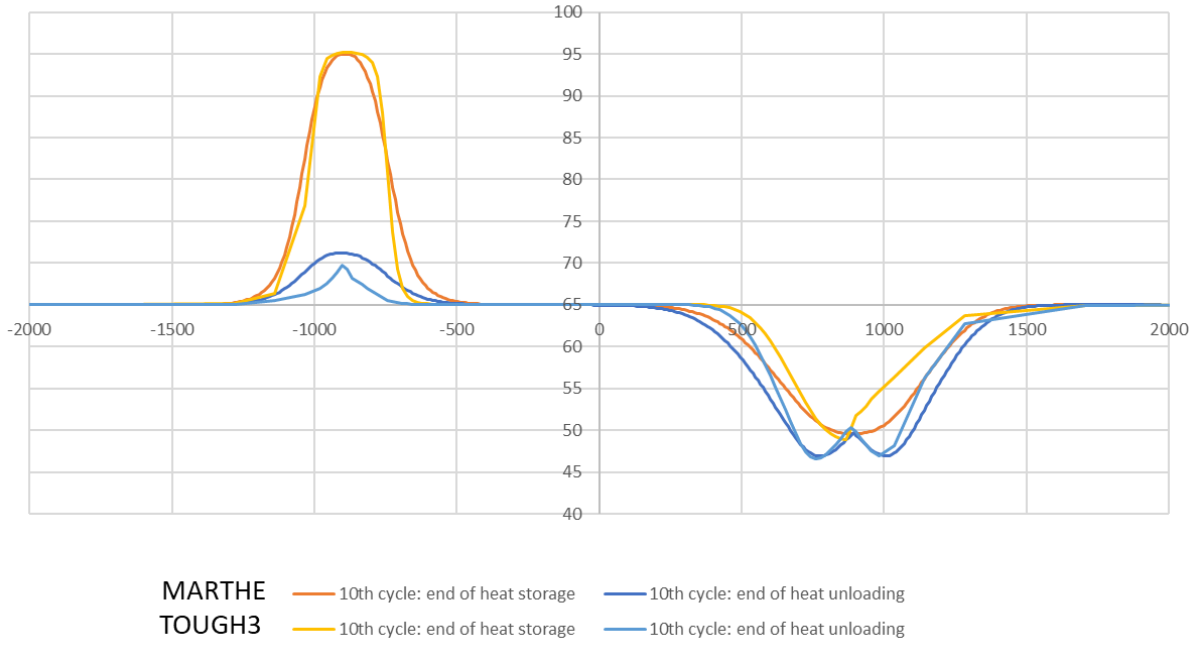


**Figure 3-12: Temperature profile between the hot (left) and cold (right) wells: end of 10th cycle of storage and unloading.**

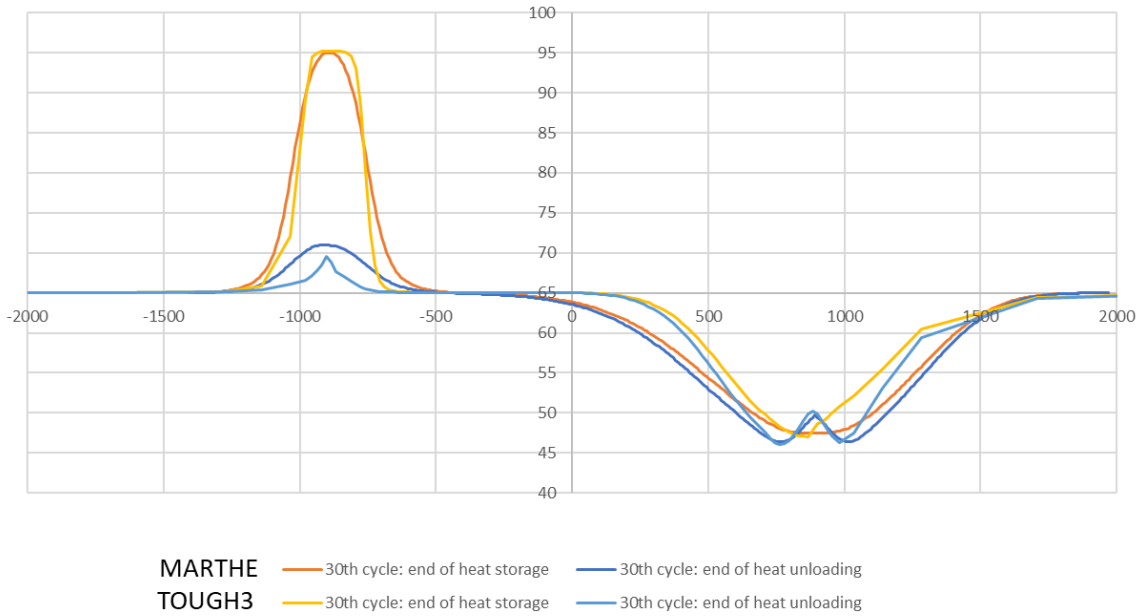


**Figure 3-13: Temperature profile between the hot (left) and cold (right) wells: end of 30th cycle of storage and unloading.**

The extension of the hot and cold plumes between both simulators are globally similar. We can see, however, that the plumes have slightly a larger extension for Marthe simulator than for Tough3 simulator. Another point of difference is the form of the plumes that are perfectly symmetrical in the lateral direction for Marthe simulator while they are not exactly symmetrical for Tough3 simulator. This is specifically the case at the end of heat unloading at the hot plume and at the end of heat storage at the cold plume. This difference is caused by the mesh difference which becomes quickly coarse when moving away from the inter well area in Tough3 simulations (see Figure 3-4).

# 4 THC benchmark (proposed by Peter Alt-Epping, University of Bern)

## 4.1 Introduction

Reactive transport models integrate thermal, hyraulic and chemical processes into a single simulation framework. Reactive transport modelling has evolved into a research tool that helps assess chemical processes in engineered or natural subsurface systems that are driven by transport processes. In engineered systems these models 1) provide guidance during the planning stage of a project (e.g. in terms of risk assessment, design optimization etc.), 2) identify knowledge gaps, develops and integrates new knowledge, 3) support monitoring activities during operation, and 4) provide a mechanistic understanding that represents the collective wisdom of the participating scientists and engineers (Steefel et al., 2015). The intercomparison of reactive transport codes through well defined benchmark problems is useful 1) for code developers to test their own code against others in terms of performance and accuracy and 2) for the code users as a starting point into new reaction processes and as templates that can be adapted for their own purposes.

Moreover, code comparisons help identify strengths and weaknesses of codes and therefore provide guidance as to which code may the most appropriate to use for solving a specific problem. There could be several reasons for choosing one code over the other: performance, ease of use, user friendliness (e.g. GUI), simulation of specific processes, specific capabilities such as meshing of complex geometries.

THC models coupling different physico-chemical processes are inherently complex. For a numerical model to yield reliable results and to have predictive capabilities it is necessary that important system parameters are well constrained and that the relevant processes and couplings between them are included in the simulation. Couplings between processes are often problem or site specific and hence simulations results may be unreliable unless constitutive relations describing these coupling are costrained by experimental results. Reaction networks in chemical models need to be complete, thermodynamic data accurate and databases have to be consistent. However, even a well constrained model can produce erroneous results if the problem is ill-posed by the user or the solution scheme is flawed.

We use the planned HT-ATES project at Forsthaus in Bern, Switzerland as a basis for constructing four simple benchmark problems that increase in complexity. The benchmark problems are simple enough to run on a laptop computer within a reasonable period of time yet they include processes and couplings most relevant to a hot water injection/extraction operation.

“Geospeicher Forsthaus” in Bern, Switzerland is a pilot project that aims at storing excess (i.e. unusable) heat produced in the waste-burning power plant at Forsthaus in the groundwater aquifer of the “Untere Süsswassermolasse” (USM) between 160 m and 500 m below ground surface (Figure 4-1). In an annual cycle, hot water carrying excess heat from the plant will be pumped into the aquifer in summer. The heat contained in the injected water is transferred to and stored in the aquifer material. In the cold winter months the warm water is extracted from the aquifer. The heat contained in the water is extracted by a heat exchanger on the ground surface and the heat gained will serve as an additional input to the district heating system. Injection temperatures are still subject to debate but will fall in the range of 60 °C to 90 °C. To establish a closed fluid circulation system supporting wells are drilled some 50-60 m away from the main injection/extraction well (Figure 4-1).

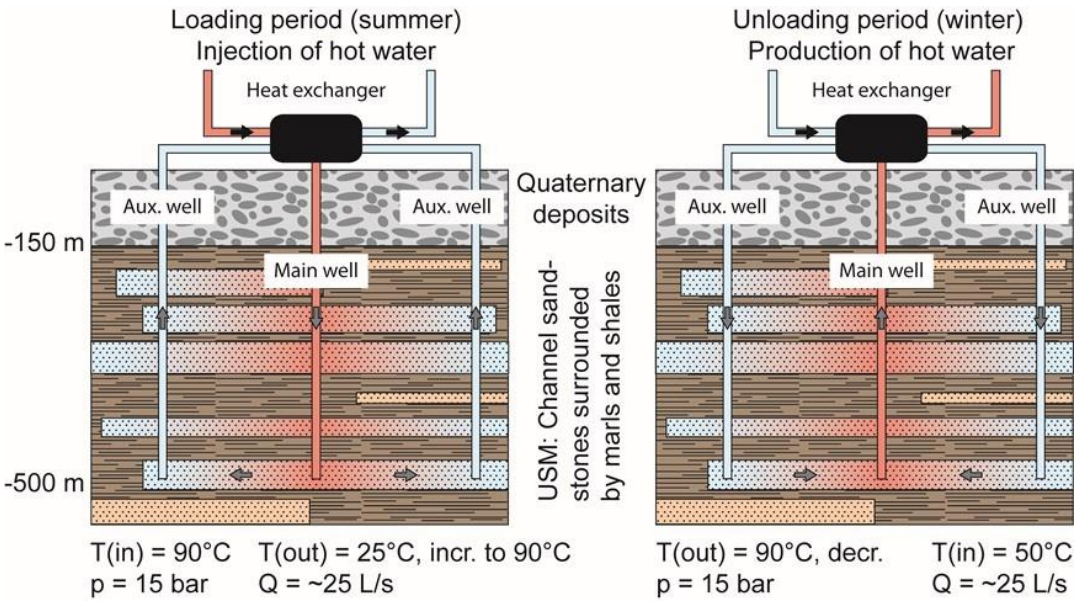


**Figure 4-1: Conceptual model of the Forsthaus "Geospeicher" in Bern, Switzerland.**

The USM consists of alternating low-permeability clays and permeable sandstone layers. The latter will be the main targets for fluid injection, whereas the clay units limit groundwater flow but contribute to storing heat. The sandstones represent ancient channel deposits and thus are laterally discontinuous. This makes a generalized model representation of system difficult.

The sandstone is composed of quartz (~40 %), feldspars (~30 %), a clay fraction (~20 %) and carbonate minerals (~10 %). The clay units are dominated by minerals such as smectites, kaolinite or illite/muscovite and contain a smaller fraction of quartz and carbonate minerals. It is reasonable to assume that the groundwater is at or close to equilibrium with the aquifer rock at the start of the operation.

Chemical reactions induced by temperature and pressure changes along the fluid pathway may pose a risk to a sustained operation of the system. Pipes may become clogged by mineral scales or corrode by chemically aggressive waters. Clogging of porosity due to mineral precipitation in the aquifer may reduce permeability and thus injectivity. Remedying these problems will incur additional costs and in the worst of case will threaten the entire operation of the system. Hence, it is useful to develop an understanding of the chemical processes taking place in such a system before the operation starts. For this, predictive numerical modelling is a useful tool.

## 4.2 Participating teams and codes

Three different codes were used in this benchmark project involving 3 teams: PFLOTRAN (University of Bern, Switzerland), RETRASO (UPC, Spain) and MARTHE-PHREEQC (BRGM, France).

*PFLOTRAN (UniBern)*

PFLOTRAN (www.pflotran.org; Hammond et al., 2014; Lichtner and Hammond, 2012) is an open source, state-of-the-art massively parallel subsurface flow and reactive transport code. PFLOTRAN solves a system of generally nonlinear partial differential equations describing multiphase, multicomponent and multiscale reactive flow and transport in porous materials. The code is designed to run on massively parallel computing architectures as well as workstations and laptops. Parallelization is achieved through domain decomposition using the PETSc (Portable Extensible Toolkit for Scientific Computation) libraries.

PFLOTRAN is written in Fortran 2003. It uses a finite volume spatial discretization, flow and transport/reactions are solved sequentially, while transport and reactions are solved implicitly. A Newton-Raphson method is used to solve the nonlinear partial differential equations.

Subsurface flow processes include single-phase variably saturated flow (Richards equation), non-isothermal two-phase $H_2O$-supercritical $CO_2$ and air-water systems, thermal-hydrologic coupled heat and mass conservation and three-phase ice-liquid-vapor ($H_2O$) flow. Multicomponent reactive transport processes include aqueous complexation, sorption (isotherm-based, ion exchange, surface complexation), mineral precipitation/dissolution and microbially mediated biodegradation.

*RETRASO (UPC)*

RETRASO (Saaltink et al, 2004) simulates transport processes (advection, dispersion and diffusion) and chemical reactions (acid-base reactions, redox, complexation, adsorption, cation exchange, precipitation and dissolution of minerals). Chemical reactions can be assumed to follow either an equilibrium or a kinetic approach. The numerical solution is obtained by using a global implicit or direct substitution approach (DSA) in which chemical equations are substituted as a source/sink term in the transport mass-conservation equations which are solved at the same time. All equations are solved simultaneously by applying the Newton-Raphson method.

Triangle finite element techniques are used for spatial discretization. RETRASO can cope with problems having irregular boundaries and composed of non-uniform physical and geochemical properties. The code can handle heterogeneous and anisotropic media in two-dimensional horizontal plane for confined or unconfined aquifers, in two-dimensional vertical planes and in three dimensional regions with axial symmetry for confined aquifers. Both steady state and transient flow regimes can be simulated.

*MARTHE-PHREEQC (BRGM)*

The MARTHE-PHREEQC reactive transport modelling software is an extension of the MARTHE software (http://marthe.brgm.fr/, Thiéry, 2015) used in the TH benchmarks described above. MARTHE was upgraded by coupling it with the PHREEQC chemical module (Parkhurst and Appelo, 2013). The coupling algorithm is purely sequential; at each time step, MARTHE computes the hydraulic head field and hence the velocity in the entire domain. It then transports all dissolved chemical elements and heat to determine the temperature field on which geochemical reactions depend. Then, the geochemistry is computed using PHREEQC. PHREEQC is one of the most advanced, best known and most widely distributed batch chemical simulators. It can simulate a broad range of geochemical processes. PHREEQC includes a BASIC interpreter that allows for incorporating scripts written in the BASIC programming language into the input file. Hence it is possible to easily customize simulations via the input file while keeping the underlying source code untouched.

## 4.3 Problem description

The benchmark problem is based on the Forsthaus HT-ATES project in the city of Bern in Switzerland. The project is currently in the planning stage so that at this stage the model parameterization, in particular those parameters related to the operation of the system (e.g. pumping rate, injection temperature) are based on realistic assumptions. The chemical reaction network and chemical parameters implemented in the more advanced benchmark problems are constrained by batch and flow-through experiments carried out at the University of Bern.

To keep the benchmark simulations tractable, the model is a strong simplification of reality. The model geometry is axisymmetric, with a radius of 200 m and the injection and extraction well in the center. The model represents a single clay-sandstone-clay sequence of the USM (Figure 4-2), eqch layer is 5 m thick. We assume that the domain is symmetric with respect to a horizontal plane at mid-depth so that the vertical dimension of the model is reduced to 7.5 m, comprising a 5 m thick clay layer and a 2.5 m thick sandstone layer (Figure 4-2). Top and bottom boundaries are impermeable and adiabatic boundaries, hence both boundaries represent planes of symmetry.

The benchmark problem is divided into four components problems, starting with simple 1D reactive transport model, followed by heat and solute transport alone and then by the implementation of the full reaction network. Additional complexity is introduced in component problem 4 by incorporating a simple “heat exchanger” to model the effect of cooling and depressurizing the extracted fluid.

The clay layer is of low permeability and thus acts as a hydraulic seal. The clay layers play an important role in storing heat. In contrast, the sandstone layer is permeable and stores the injected thermal water. There are no supporting wells included in the model hence we do not consider the complete circulation system. Instead, a fixed hydrostatic pressure is imposed at the far end of the model, allowing for free in and outflow of water during injection and extraction, respectively. A fixed background temperature of 15 °C and a fixed pore water composition are assigned to the far end boundary representing undisturbed, pre-injection conditions. In any case, the lateral extend (r = 200 m) of the model is chosen to minimize the effect of the outer boundary on processes within the system.

The well is represented as a highly permeably zone with a radius of 0.11 m (representing a borehole of 0.22 m diameter). The well screen is perforated over the entire model thickness and fluid injection is distributed over the 7.5 m length of the well. Thus, the rate of infiltration into each unit is scaled by its permeability. The screen is considered explicitly in the model and represents a 0.1 m interval between borehole and the rock.

Because we consider only a 7.5 m thin interval of the total 350 m thickness of the USM, injection and extraction into and from the model rock units are scaled by a factor of 7.5/350 = 0.021.

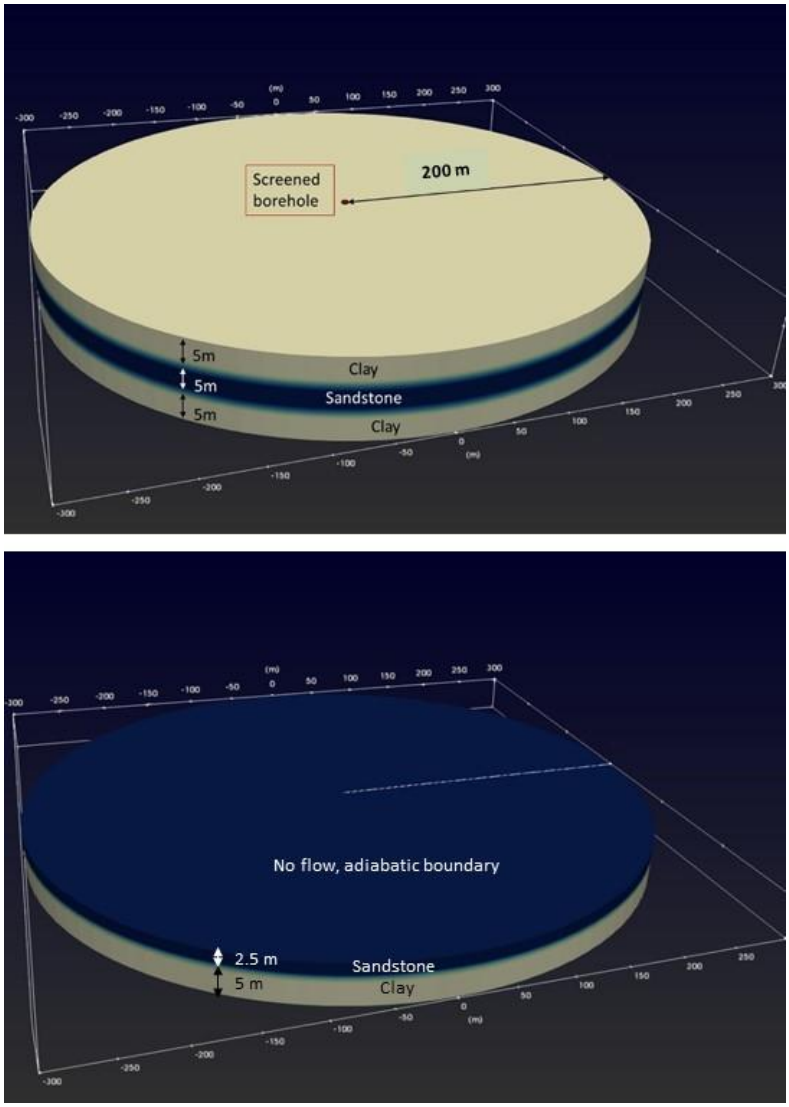


**Figure 4-2: Simplified model of the "Geospeicher" , full domain and reduced domain (upper and lower panel, respectively).**

The benchmark problem simulates a sequence of water injection/extraction cycles over a period of 10 years. Injection and extraction occur according to an annual schedule, representing injection and extraction during warm and cold seasons, respectively. The injection temperature is 90 °C. The origin of the injected water is the groundwater in the USM aquifers. This implies that the water was in chemical equilibrium with the sandstone mineralogy at in situ conditions before its usage as heat carrier during operation. During the first cycle, the water is pumped to the surface, heated to 90 °C and then reinjected into the USM reservior.

Although the groundwater composition of the USM is known reasonably well from various drilling campaigns and from batch chemical simulations of in-situ aquifer conditions, the composition of the 90 °C hot reinjected water is not known. However, the composition of the reinjected water can be estimated by successively heating the USM groundwater from the in-situ temperature to 90 °C. Minerals that become oversaturated are allowed to precipitate and are then removed from the system to prevent redissolution.

Injection and extraction of thermal water into and out of the USM aquifer drive advective flow through the reservoir. Pumping water in and out of the system follows an annual schedule summarized below. The total injected volume is somewhat higher than the extracted volume. To avoid excessive over- or underpressures, the boundary at the far end of the domain allows for water entering or leaving the domain. It constitutes a Dirichlet boundary with fixed hydrostatic pressure and background reservoir temperature. Heat transport is by convection and conduction. Simulating convection requires a modified implementation of Darcy's law which explicitly accounts for temperature dependent changes in density and viscosity as well as buoyancy effects due to density differences in the fluid. However, given the small vertical extent of the model and the strong lateral forcing due to pumping, the buoyancy effect in the model is negligible. Top and bottom boundaries are impermeable and adiabatic following symmetry constraints based on the assumption that strata above and below heat at the same rate and that clay units inhibit vertical flow.

The initial pressure distribution in the USM is hydrostatic with a fixed pressure along the top boundary of 4.5 MPa. The initial temperature is 15 °C. The initial pressure and temperature conditions remain fixed along the outer boundary of the domain, by assigning Dirichlet PT conditions along the outer boundary.

Diffusion of solutes is the second main chemical transport mechanism. Diffusion plays a role in the exchange of solutes between the permeable sandstone and the low permeability clays. Diffusion is assumed to be Fickian The diffusive flux according to Fick's law can be written as:

$$J_i = D_e \frac{\partial C_i}{\partial x} \tag{4-1}$$

where $J_i$ is the diffusive flux of component $i$, $C_i$ is the concentration and $D_e$ is the effective diffusion coefficient, defined as

$$D_e = \tau\phi D_0 , \tag{4-2}$$

for liquid and gas, respectively, where $\tau$ and $\phi$ are tortuosity and porosity, respectively, and $D_0$ is the molecular diffusion coefficient assumed to be 1e-9 $m^2/s$ for all species.

Discretization is refined in and around the well. The maximum dimension of the cells in the radial or vertical direction is 1 m.

The reaction network includes the carbonate system with the minerals calcite and dolomite. Quartz is expected to be the dominant primary mineral in the sandstone, followed by the feldspars albite and K-feldspar. Clay minerals such as smectite, illite, chlorite and muscovite occur in small amounts. The clay units are dominated by smecite and quartz as primary minerals. Calcite and dolomite exist in smaller fractions. Clay minerals are known to have a negative surface charge and thus provide surface sites for sorbing cations. Since we have little information about the exchange properties of the clay units in the USM we neglect sorption reactions here. Minerals are only involved in dissolution and precipitation reactions. Amorphous silica is included as a possible mineral precipitate in simulations involving a heat exchanger (component problem 4).

Mineral solubilities are computed from thermodynamic databases based on the default PFLOTRAN database derived to a large extent from the SUPCRT92 database (Johnson et al., 1992). For the carbonate system SUPCRT92 was used to compute thermodynamic properties at 4.5 MPa. This was done to account for the pressure dependence of the solubility of $CO_2$,g. We assume that the pressure dependence of the thermodynamic properties of quartz and the alumino-silicates can be neglected. The stability of aqueous complexes is based on the same default thermodynamic database. The selection of aqueous complexes to be included in the simulation is based on the availability of temperature dependent equilibrium constants in the database. Thermodynamic data used in this simulation are summarized in Appendix F.

Mineral reactions are implemented as kinetic reactions. A rate law for mineral precipitation and dissolution can be written in a general form (e.g., Lasaga et al., 1994; Steefel and Lasaga, 1994):

$$r = Ak\left|\left(\frac{Q}{K}\right)^{M} - 1\right|^{n} \tag{4-3}$$

where $r$ is the rate (positive denotes mineral precipitation, negative denotes mineral dissolution), $A$ is the reactive surface area, $k$ is the temperature-dependent dissolution rate constant, $Q$ is the ion activity product, $K$ is the equilibrium constant for the mineral-water reaction, and $M$ and $n$ are empirically determined exponents to account for nonlinear rate-laws.

The temperature dependence of the rate constant is expressed through the Arrhenius equation (Lasaga, 1984), which can be written in general terms as:

$$k = k_{25}\exp\left[\frac{-E_a}{R}\left(\frac{1}{T} - \frac{1}{298.15}\right)\right] \tag{4-4}$$

where $k_{25}$ is the rate constant at 25 °C, $E_a$ is the activation energy, $R$ is the gas constant and $T$ is the temperature in Kelvin. The dissolution rate of minerals commonly shows a dependence on the pH (and/or other species in solution). To account for these effects the rate constant of a mineral can be written as the sum of species-dependent rate constants. Here we consider only the pH dependence of a rate constant, which can be formulated as (Lasaga et al., 1994; Palandri and Kharaka, 2004):

Reaction rates of feldspars and carbonates are known to be strongly pH dependent, hence their bulk reaction rate is formulated as the sum of pH dependent parallel reactions. Rate parameters are taken from the compilation of kinetic mineral properties by Palandri and Kharaka (2004).

$$\begin{aligned} k = {} & k_{25}^{n}\exp\left[\frac{-E_a^{n}}{R}\left(\frac{1}{T} - \frac{1}{298.15}\right)\right] + k_{25}^{ac}\exp\left[\frac{-E_a^{ac}}{R}\left(\frac{1}{T} - \frac{1}{298.15}\right)\right]a_{H+} \\ & + k_{25}^{b}\exp\left[\frac{-E_a^{b}}{R}\left(\frac{1}{T} - \frac{1}{298.15}\right)\right]a_{OH-} \end{aligned} \tag{4-5}$$

where the superscripts *n*, *ac* and *b* denote neutral, acidic and basic conditions, respectively, and $aH^+$ and $aOH^-$ are the activity of $H^+$ and OH-, respectively.

Initially, conditions in the aquifer are in thermodynamic equilibrium with the most reactive minerals (i.e. calcite and dolomite). We assume that $CO_2$,aq is in initial equilibrium with a $pCO_2$ of 7.08e-3 bar. The initial chemical conditions remain fixed as Dirichlet-type boundary condition along the outer boundary of the domain.

In component problem 4 we assess the implications of depressurizing the thermal water for the solubility of $CO_2$,g. This is achieved by creating a dummy mineral $CO_2$,s which reacts according to the reaction

$CO_2$,s = $CO_2$,aq

The solubility of the mineral mirrors the solubility of $CO_2$,g at 3 bar. The exsolution of $CO_2$,g can thus be simulated as a precipitation reaction of the mineral $CO_2$,s. The rate of this mineral reaction is fast such that $CO_2$,g/$CO_2$,aq equilibrium is maintained if gas saturation is achieved.

In component problem 4, the borehole acts as a heat exchanger during extraction cycles. This requires that the borehole attains the temperature after cooling in the heat exchanger during extraction and switches back to the injection temperature for the injection cycle. This can be achieved by changing material properties, boundary conditions and chemical conditions in time simultaneously during the simulation. Details of this approach are described below.

*Summary of the geochemical reaction network* (note: "45 bar" indicates minerals and species for which temperature-dependent solubilities are calculated at 45 bar rather than at saturation pressure)
Thermodynmaic properties of all species, minerals and gases are summarized in Appendix F.

*Component species*
$SiO_2$(aq)
$H^+$
$Na^+$
$Cl^-$
$Ca^{++}$
$Mg^{++}$
$K^+$
$Al^{+++}$
$HCO_3^-$
$SO_4^{--}$

*Secondary species*
$OH^-$
$CO_2$(aq) (45bar)
$CO_3^{--}$ (45bar)
$H_3SiO_4^-$
$HSiO_3^-$
$MgOH^+$
$MgCO_3$(aq) (45bar)
$MgHCO_3^+$ (45bar)
$MgCl^+$
$MgSO_4$(aq)
$CaCO_3$(aq) (45bar)
$CaHCO_3^+$ (45bar)
$CaCl^+$
$CaCl_2$(aq)
$CaSO_4$(aq)
KCl(aq)
NaCl(aq)
NaOH(aq)
$NaCO_3^-$
$NaHCO_3$(aq)
$AlOH^{++}$
$Al(OH)_2^+$

*Gases*
$CO_2$(g) (45 bar)

*Minerals*
Quartz
Calcite (45bar)
Dolomite (45bar)
Albite
K-Feldspar
Illite
Muscovite
Smectite-Na
Smectite-Ca
Kaolinite
Clinochlore-14A
Gypsum
Anhydrite
Amorphous silica
"$CO_2$(s)" (representing $CO_2$(g) solubility at 3 bar)

## 4.4 Component problem specification

### 4.4.1 Component problem 1

The first component benchmark problem is designed to compute the composition of the injected water by heating the USM in-situ groundwater to 90 °C along a 1D flowpath. In addition, from this simulation it can be assessed which minerals are expected to form as scales upon heating of the groundwater and in what quantities.
The composition of the reinjected water is computed by heating the USM groundwater from its in-situ temperature (15 °C ) to 90 °C. This is achieved by letting the groundwater flow along a fixed linear temperature profile that starts at 15 °C (representing ambient conditions) and ends at 90 °C. The water composition at 90 °C is extracted and used in benchmark problem 3 and the principal problem as the composition of the injected water. The flowpath is 38 m long, it is discretized into 152 cells, each having a length of 0.25 m. The material properties are that of the sandstone (Table 4-1), except that a very high thermal conductivity 1e6 W m-1 K-1 is imposed which ensures that a linear temperature gradient between inlet and outlet is attained rapidly and that the temperature gradient remains linear during flow.
At the inlet, the fluid composition is that of the sandstone porewater at 15 °C (Table 4-1). At the outlet a zero-gradient boundary condition and a fixed temperature of 90.75 °C are imposed. The temperature gradient along the flowpath is thus 1.99 °C /m. (Note that since PFLOTRAN uses cell boundaries along domain boundaries, this model set up yields the print out of the fluid composition at exact 90 °C. It is possible that other codes use different discretization schemes (e.g. codes using nodes on boundaries), that may require a different model dimensioning or interpolation of results to obtain results precisely at 90 °C.) Fluid flow along the flowpath is driven by a pressure differential between inlet and outlet of 0.01 MPa.

Total simulation time is 730 days, the maximum allowable timestep is 2 days.

**Table 4-1: Injected pore water composition as total concentrations or buffering mineral or gas phase.**

| | **Sandstone porewater (15 °C)** |
|---|---|
| Tracer | 1e-5 |
| $SiO_2$,aq | Quartz |
| pH | 7.6 |
| $Na^+$ | Charge |
| $Cl^-$ | 8.69e-4 |
| $Ca^{++}$ | Calcite |
| $Mg^{++}$ | Dolomite |
| $K^+$ | 7.16e-5 |
| $Al^{+++}$ | 1e-12 |
| log($pCO_2$) (bar) | -2.15 |
| $SO_4$-- | 2.34e-4 |

## 4.4.2 Component problem 2

Component problem 2 involves a thermal-hydraulic simulation with non-reactive transport in the axisymmetric model domain shown in Figure 4-2 and Figure 4-3. Figure 4-3 summarizes boundary and initial cnditions. Along with the thermal water a non-reactive tracer is injected to simulate the radius of chemical perturbation around the injection well. Thermal and hydraulic properties of the different materials are summarized in Table 4-2. The annual schedule of injection and extraction and the pumping rates are given in Table 4-3. The simluated operation time is 10 years.

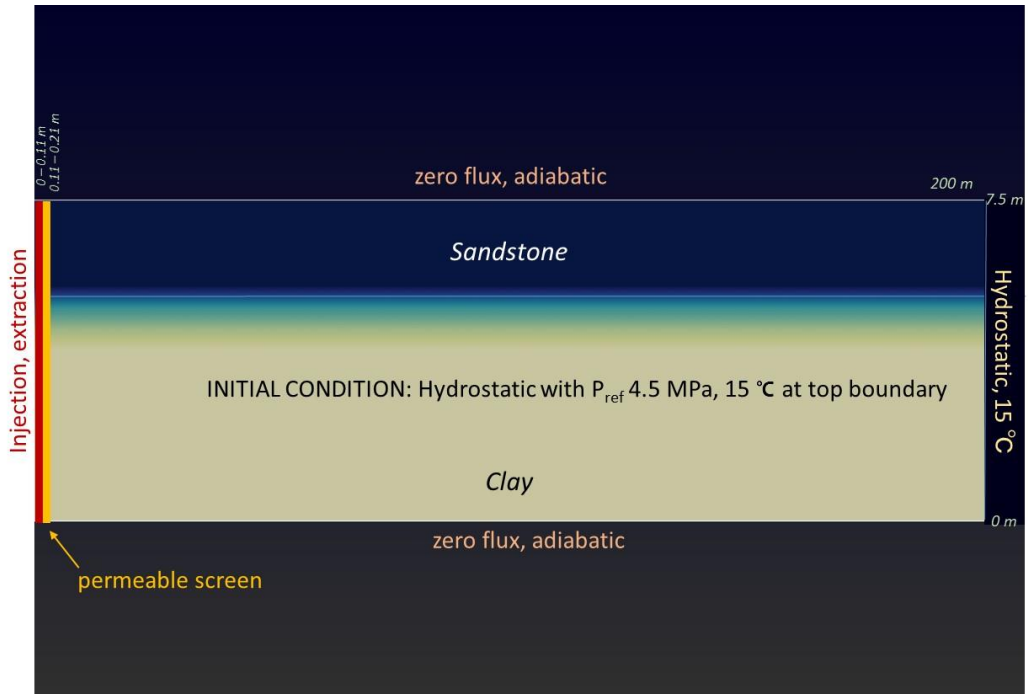


**Figure 4-3: Model dimensions (not to scale) and boundary and initial conditions for flow and heat transport.**

The discretization of the cylindrical domain is as follows:

Cell dimensions (m) in r (radial) direction are:
2*0.05 1*0.01 2*0.05 9*0.1 1*0.39 97*0.5 150*1.0

The dimensions of the material zones in the radial direction are:

| | |
|---|---|
| Borehole | (0 - 0.11 m) |
| Screen | (0.11 - 0.21 m) |
| Reservoir rock | (0.21 - 200m). |

Cell dimensions (m) in z (vertical) direction are:
5*1.0 5*0.5

Thus there are 262 and 10 cells in r and z, respectively, resulting in a total number of cells of 2620.

The maximum allowable time step is 2 days. Total simulation time is 3650 days (10 years).

**Table 4-2: Physical properties of the materials.**

| | Sandstone | Claystone | Screen | Borehole |
|---|---|---|---|---|
| **Porosity** | 0.1 | 0.05 | 0.5 | 1.0 |
| **Tortuosity** | 0.05 | 0.05 | 0.05 | 1.0 |
| **Permeability ($m^2$)** | 3.45e-13 | 2.6e-17 | 1e-10 | 1e-10 |
| **Dispersivity (transverse and longitudinal) (m)** | 1e-3 | 1e-3 | 0.0 | 0.0 |
| **Heat capacity (J $kg^{-1}$ $K^{-1}$)** | 750 | 750 | 750 | 818 |
| **Thermal conductivity (W $m^{-1}$ $K^{-1}$)** | 2.67 | 2.67 | 1e-5 | 1.6 |
| **Density ($kg/m^3$)** | 2743 | 2743 | 2780 | 2000 |

**Table 4-3: Annual schedule of injection/extraction cycles.**

| Time (d) | Q (l/s) | T (°C) | Inject | Extract |
|---|---|---|---|---|
| 0-216 | 25 | 90 | x | |
| 216-365 | 25 | 50 | | x |

### 4.4.3 Component problem 3

In component problem 3 the reaction network is implemented and fluid rock reactions are computed and evaluated using the same model design (domain, discretization and thermal-hydraulic initial and thermal-hydraulic boundary conditions and material properties) as in component problem 2. The mineralogy of the clayrocks and the sandstone are summarized in Table 4-4. Kinetic properties of the minerals are given in Table 4-5. The thermodynamic properties of all minerals at different temperature points are presented in Appendix F. The composition of the injected water the initial clay and sandstone pore waters are summarized in Table 4-6.

**Table 4-4: Mineral composition (volume fraction) of the clay and sandstone units in the USM.**

| | Clay | Sandstone |
|---|---|---|
| Quartz | 0.18 | 0.35 |
| Calcite | 0.15 | 0.12 |
| Dolomite | 0.05 | 0.02 |
| Albite | 0.10 | 0.18 |
| K-feldspar | 0.07 | 0.11 |
| Illite | 0.10 | 0.05 |
| Muscovite | 0.10 | 0.05 |
| Ca-Smectite | 0.10 | 0.05 |
| Na-Smectite | 0.10 | 0.05 |
| Kaolinite | 0.00 | 0.00 |
| Mg-chlorite | 0.05 | 0.02 |
| Gypsum | 0.00 | 0.00 |
| Anhydrite | 0.00 | 0.00 |
| $SiO_2$(am) | - | - |
| $CO_2$(s) | - | - |

All minerals are allowed to precipitate as secondary minerals. Amorphous silica and $CO_2$(s) are allowed to precipitate only in the well and in the screen in component problem 4. Note also that since the solubility of amorphous silica is higher than that of (crystalline) quartz, quartz is more likely to precipitate based on thermodynamic reasons. However, due to kinetic and other reasons, the precipitation of quartz is inhibited and in most geothermal systems amorphous silica is the most common polymorph found in mineral scales. In the principal problem, we assess if amorphous silica precipitates in the heat exchanger, if quartz precipitation is suppressed.

**Table 4-5: Mineral kinetic properties.**

| | Log rate constant (neutral) mol $m^{-2}$ $sec^{-1}$ | Activation energy (neutral) | Log rate constant (acid) mol $m^{-2}$ $sec^{-1}$ | Prefactor ($H^+$) | Activation energy (acid) | Reactive surface area $m^2/m^3_{bulk}$ |
|---|---|---|---|---|---|---|
| Quartz | -13.4 | 90 | - | - | - | 1 |
| Calcite | -5.81 | 14.4 | -0.3 | 1 | 23.5 | 1 |
| Dolomite | -7.53 | 52.2 | -3.19 | 0.5 | 36.1 | 1 |
| Albite | -12.56 | 70 | -10.16 | 0.457 | 14.4 | 1 |
| K-feldspar | -12.41 | 38 | -10.06 | 0.5 | 51.5 | 1 |
| Illite | -13.55 | 22 | -11.85 | 0.37 | 22 | 1 |
| Muscovite | -13.55 | 22 | -11.85 | 0.37 | 22 | 1 |
| Ca-Smectite | -12.78 | 35 | -10.98 | 0.34 | 12.6 | 1 |
| Na-Smectite | -12.78 | 35 | -10.98 | 0.34 | 12.6 | 1 |
| Kaolinite | -13.18 | 22.2 | -11.31 | 0.777 | 65.9 | 1 |
| Mg-chlorite | -12.52 | 88 | -11.11 | 0.5 | 88 | 1 |
| Gypsum | -2.79 | 0 | - | - | - | 1 |
| Anhydrite | -3.19 | 14.3 | - | - | - | 1 |
| $SiO_2$(am) | -9.42 | 49.8 | - | - | - | 100 |
| $CO_2$(s) | -6 | 50 | - | - | - | 100 |

**Table 4-6: Initial pore water composition as total concentrations or buffering mineral or gas phase. The composition of the injected water is extracted from component problem 1**

| | Clay (15 °C) | Sandstone (15 °C) | Injected (90 °C) |
|---|---|---|---|
| Tracer | 1e-5 | 1e-5 | 1.0 |
| $SiO_2$,aq | Quartz | Quartz | 6.04e-5 |
| pH | 7.6 | 7.6 | 7.014 |
| $Na^+$ | Charge | Charge | Charge |
| $Cl^-$ | 8.69e-4 | 8.69e-4 | 8.69e-4 |
| $Ca^{++}$ | Calcite | Calcite | Calcite |
| $Mg^{++}$ | Dolomite | Dolomite | Dolomite |
| $K^+$ | 7.16e-5 | 7.16e-5 | 7.16e-5 |
| $Al^{+++}$ | 1e-12 | 1e-12 | 1e-12 |
| log($pCO_2$) (bar) | -2.15 | -2.15 | -1.1236 |
| $SO_4$-- | 2.34e-4 | 2.34e-4 | 2.34e-4 |

### 4.4.4 Component problem 4

This problem includes a simplified “heat exchanger” used to cool the extracted water. The same model design (domain, discretization and thermal-hydraulic initial and boundary conditions and material properties) as in component problem 2 is used.

Simplifying the geometry of the system often comes at the expense of reality. Since the model includes only a short depth interval of the USM reservoir, it cannot account for processes taking place outside the aquifer, i.e. in the well or at the surface, in a rigorous manner. Instead, one can resort to modifying the simple model in such a way, that it mimics processes in other parts of the system. Here we modify the properties of the well and the screen in such a way that they mimic the well and the heat exchanger at the surface, respectively (Figure 4-4). Although strongly simplified this approach may still provide valuable insights into processes taking place in those parts of the system.

The heat exchanger (the red area in Figure 4-4) is implemented as follows:
Between each change from injection to extraction there is one day during which
1) the thermal conductivity of the well is increased to a high value (e.g. 10000 J kg-1 K-1)
2) the temperature along the section where the well hits the boundary is set to the desired lowest temperature in the heat exchanger, which is assumed to be 20 °C
3) the well attains the desired temperature of the heat exchanger throughout

4) the heat capacity is set to some high value (e.g. 1e6 W m-1 K-1)
5) Mineral precipitation reactions are turned on
6) Mineral precipitation rates are increased by a factor of 100 to achieve mineral equilibration within the short interval of the model heat exchanger

In addition, the well screen (the blue area in Figure 4-4) is used to mimic an extraction well. During extraction water enters the well where it is no longer buffered by the rock but undergoes pressure and temperature changes as it ascends to the surface, potentially leading to scale formation. In this simple model, the same process occurs only over the length scale of the screen. While passing through the screen the water moves from rock buffered conditions to unbuffered conditions. However, given the short interval of the screen, we cannot include in detail the pressure and temperature changes within a well. The short interval implies that the temperature remains essentially constant. Pressure changes are not accounted for. Furthermore:

1) Since there are no primary minerals in the screen, only mineral precipitation is allowed during extraction, representing the formation of scales.
2) Mineral precipitation rates are increased by a factor of 100 to achieve mineral equilibration within the short interval of the screen

Between each change from extraction to injection there is one day during which all properties of the well and heat exchanger are reset to those defined in the problem description. During injection minerals are no longer allowed to react in the well and heat exchanger to preserve those minerals that precipitated during extraction so that minerals that form during extraction can accumulate.

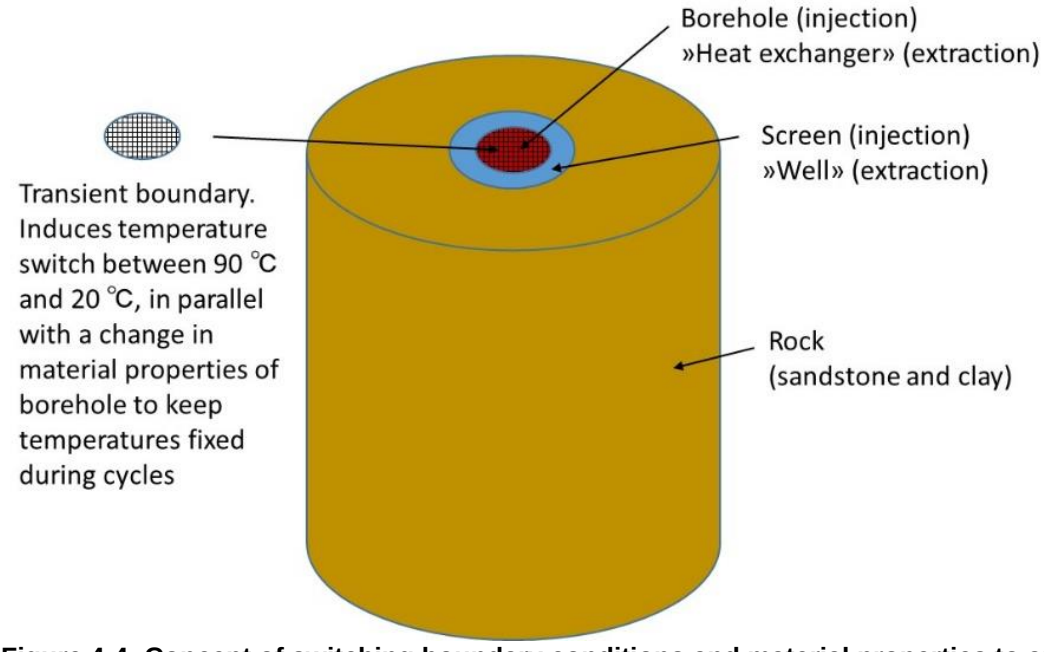


**Figure 4-4: Concept of switching boundary conditions and material properties to approximate conditions in the installations (well and heat exchanger) in the real system.**

## 4.5 Results and code comparison

### 4.5.1 Component problem 1

The injected USM groundwater (sandstine porewater) moves along a 1D flowpath at constant velocity undergoing a constant increase in temperature from 15 °C to 90 °C (Figure 4-5). The injected water is in equilibrium with calcite and dolomite.

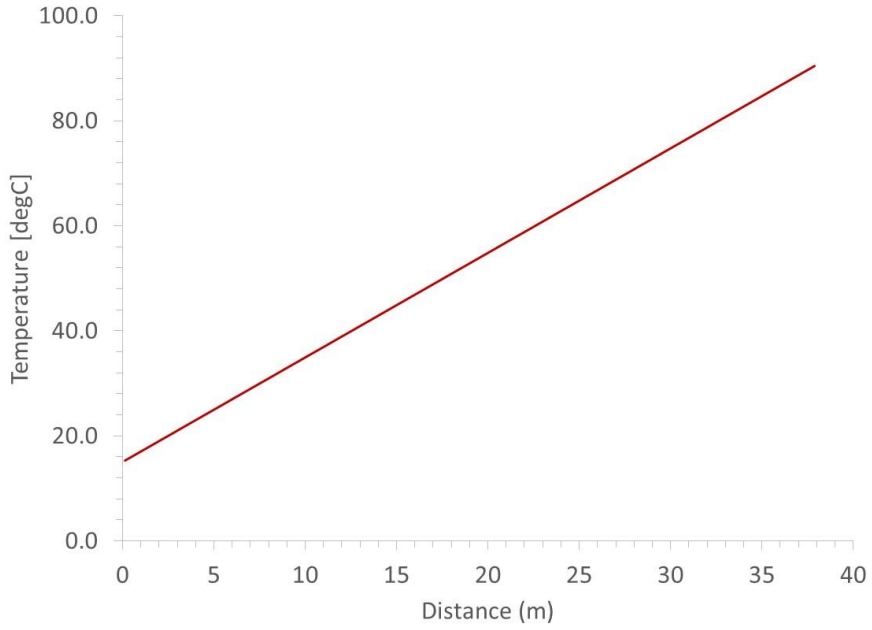


**Figure 4-5: Linear temperature profile along the flowpath.**

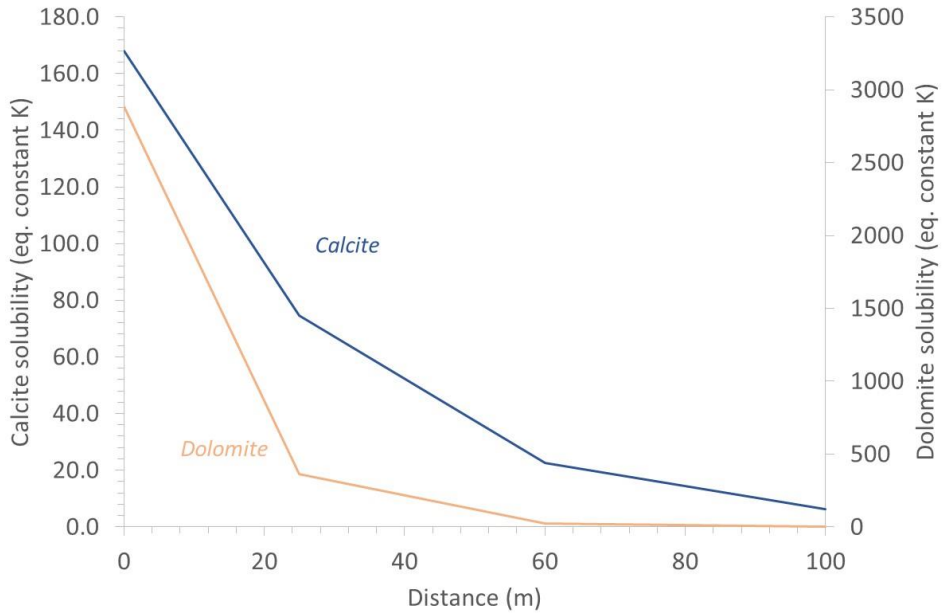


**Figure 4-6: Solubility (as equilibrium constant K) of calcite and dolomite as a function of temperature as given in the thermodynamic database. The solubility decreases exponentially over the temperature interval of interest.**

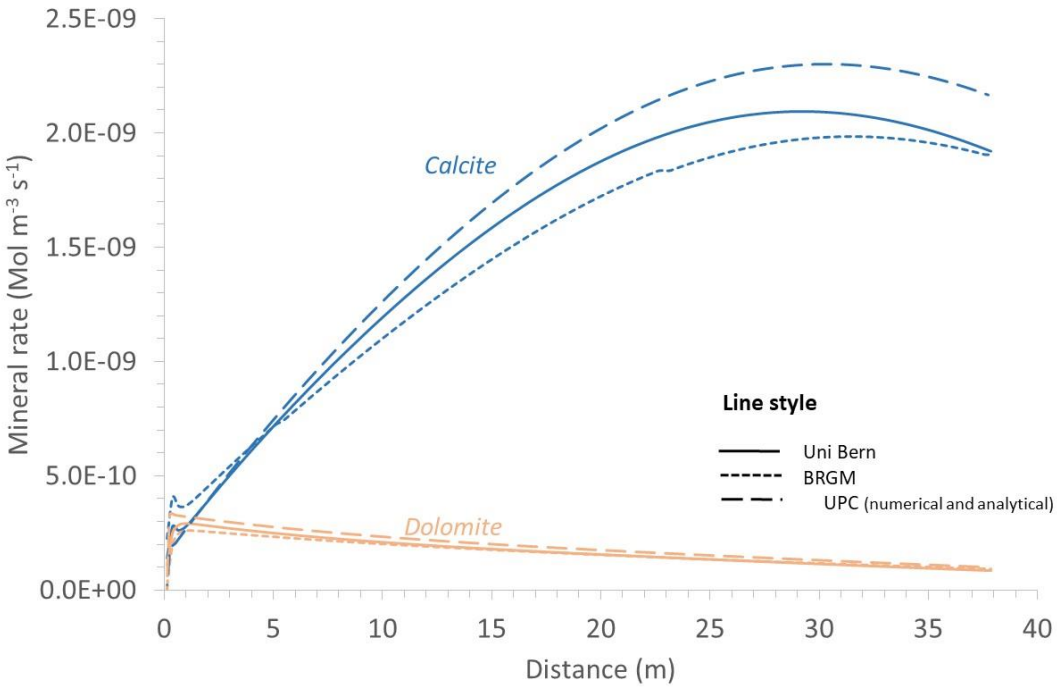


**Figure 4-7: Profiles of carbonate mineral reaction rates. Heating the USM groundwater leads to massive calcite precipitation. Comparison of results from simulations with PFLOTRAN (Uni Bern), RETRASO (UPC) and MARTHE-PHREEQC (BRGM).**

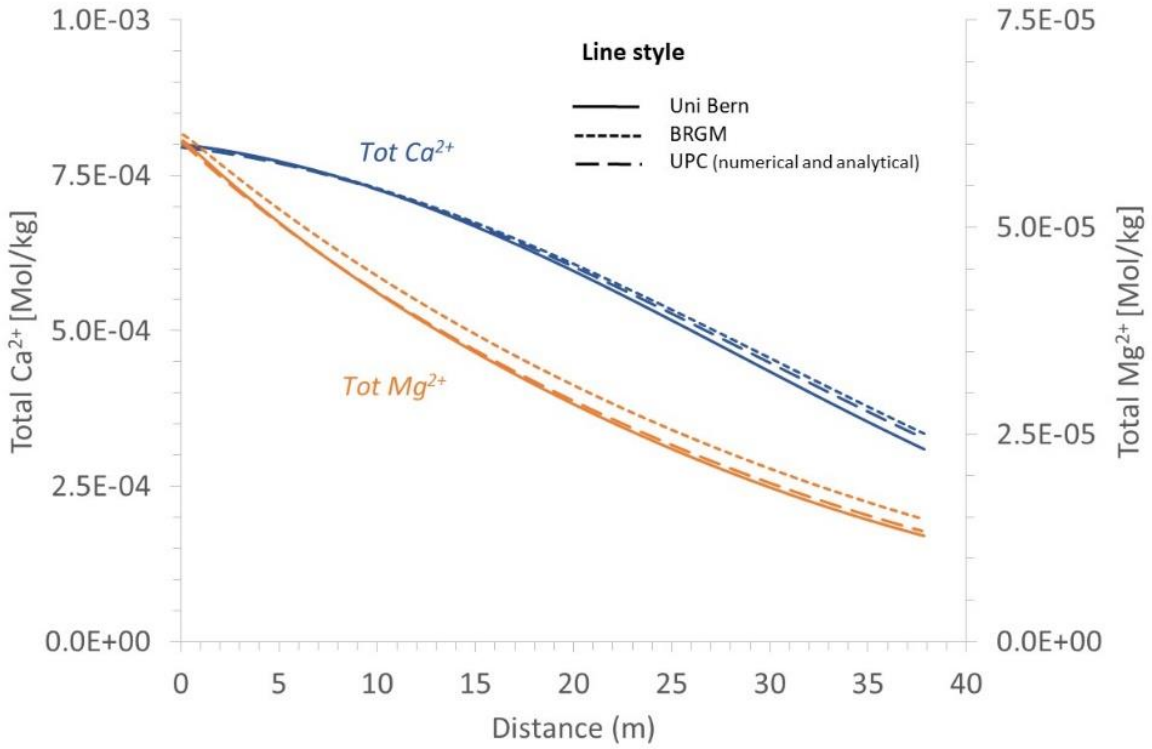


**Figure 4-8: Comparison of profiles of total Ca and total Mg computed with PFLOTRAN (Uni Bern), RETRASO (UPC) and MARTHE-PHREEQC (BRGM).**

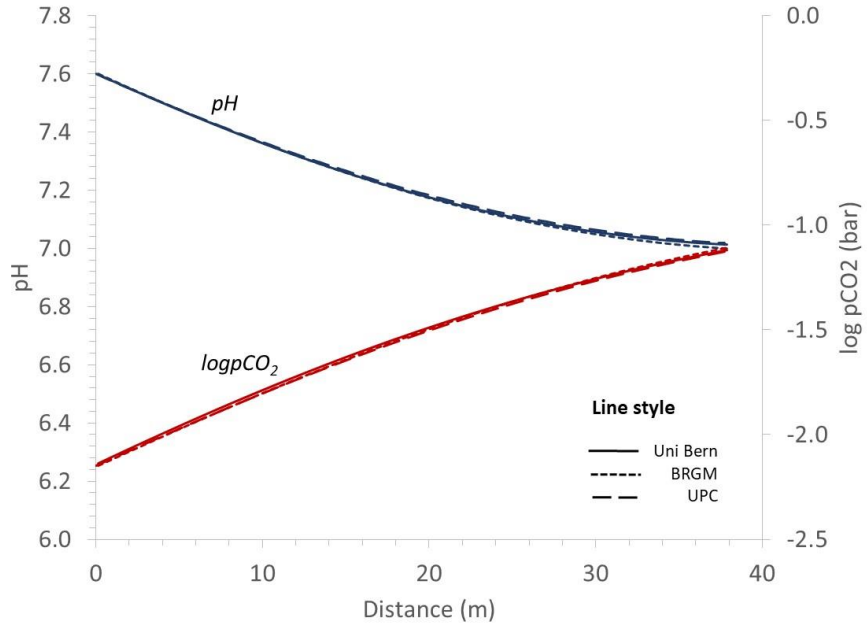


**Figure 4-9: Comparison of computed profiles of pH and log($pCO_2$) computed with PFLOTRAN (Uni Bern), RETRASO (UPC) and MARTHE-PHREEQC (BRGM).**

Upon heating, calcite and dolomite precipitate due to their retrograde solubility with temperature (Figure 4-6 and Figure 4-7). This decrease in solubility is exponential. Overall, the rate of calcite precipitation exceeds that of dolomite precipitation by roughly one order of magnitude. The precipitation of carbonate minerals removes Ca and Mg from the fluid (Figure 4-8) which are not replensished by mineral dissolution. Ultimately, this limits the rate at which these minerals form which is indicated by a decrease in their precipitation rate rate (Figure 4-7)

Such conditions are analogous to reactive flow within a borehole where the fluid is detached from (potentially) dissolving minerals and precipitation (or scaling) reactions are entirely due to temperature changes and changes in the internal fluid speciation. The precipitation reaction of calcite written as

$Ca^{2+} + HCO_3^- \rightarrow$ Calcite $+ H^+$

produces acidity (the pH decreases (Figure 4-9), which drives the following reactions entailing an increase in $pCO_2$(g) (Figure 4-9)

$HCO_3^- + H^+ \rightarrow CO_2$,aq $+ H_2O$

$CO_2$,aq $\leftrightarrow CO_2$(g)

Dolomite precipitation occurs analogously but involves both $Ca^{2+}$ and $Mg^{2+}$.

It is possible to carry out mass balance calculations based on the total volume of carbonate mineral precipitation. These calculations reveal that for a flow rate if 25 l/s or 7.89e8 kg/yr (using a density at 15 °C of 1001.21 kg/$m^3$_$H_2O$) the total volume of carbonate scales produced could be as high as 19 $m^3$ per year. Assuming that a volume equivalent of 216 days or 0.59 years of pumping at 25 l/s has to be extracted from the aquifer the total amount of carbonate scales is 11.2 $m^3$. These values represent the worst case scenarios as these imply local equilibrium within the well, which is an unlikely scenario given the high flow rates.

The comparison of results from the three codes (Figure 4-7 – Figure 4-9) shows very good agreement. Differencs between computed mineral rates amount to 13% and 10% at the most for dolomite and calcite, respectively.

### 4.5.2 Component problem 2

Component problem 2 simulates the annual injection and extraction schedule summarized in Table 4-3 over a period of 10 years. The injected water contains a tracer, no reactions are included in the simulation. The results of this simulation show the relationship between the spatial extent of the thermal and the geochemical plume around the injection well.

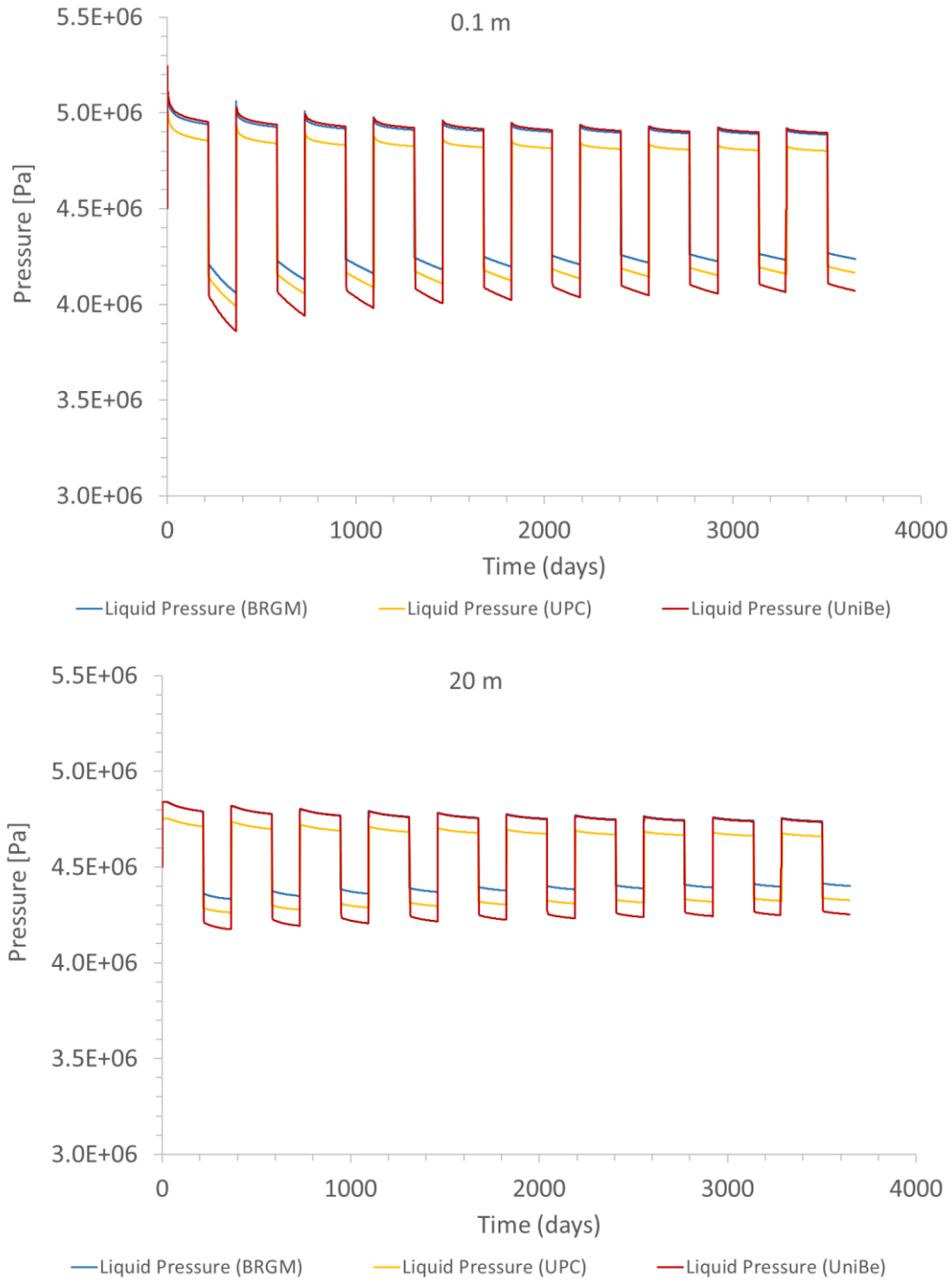


**Figure 4-10: Comparison of the pressure evolution within and 20 m away from the well (upper and lower panel, respectively). Pressures from all codes tend to deviate slightly during extraction cycles. The results from UPC show a slightly lower injection pressure.**

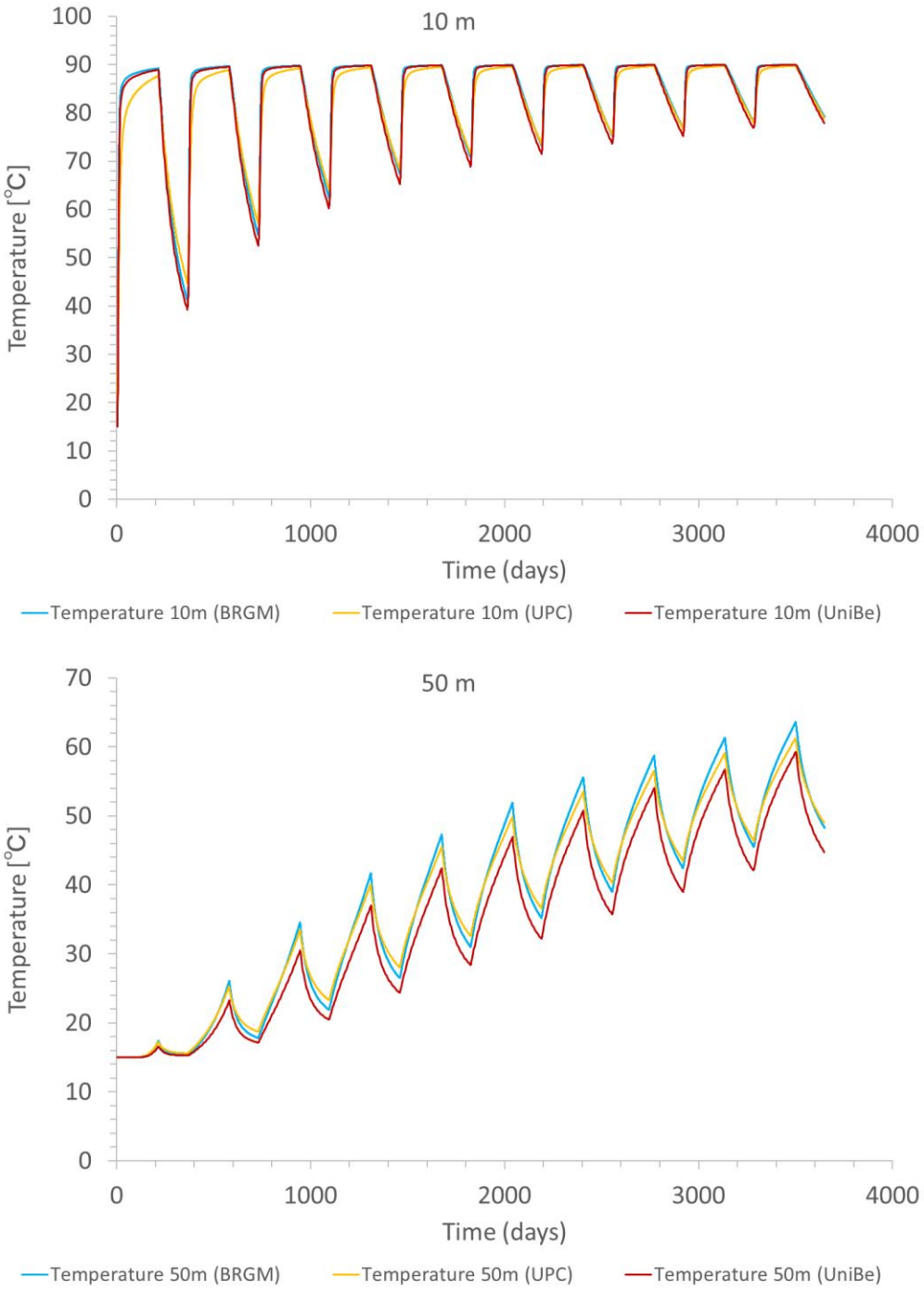


**Figure 4-11: Comparison of the temperature evolution 10 m and 50 m from the injection /extraction well (upper and lower panel, respectively). The agreement between the codes is excellent close to the well, stronger deviations in the range of 4-5 °C occur at greater distance from the well.**

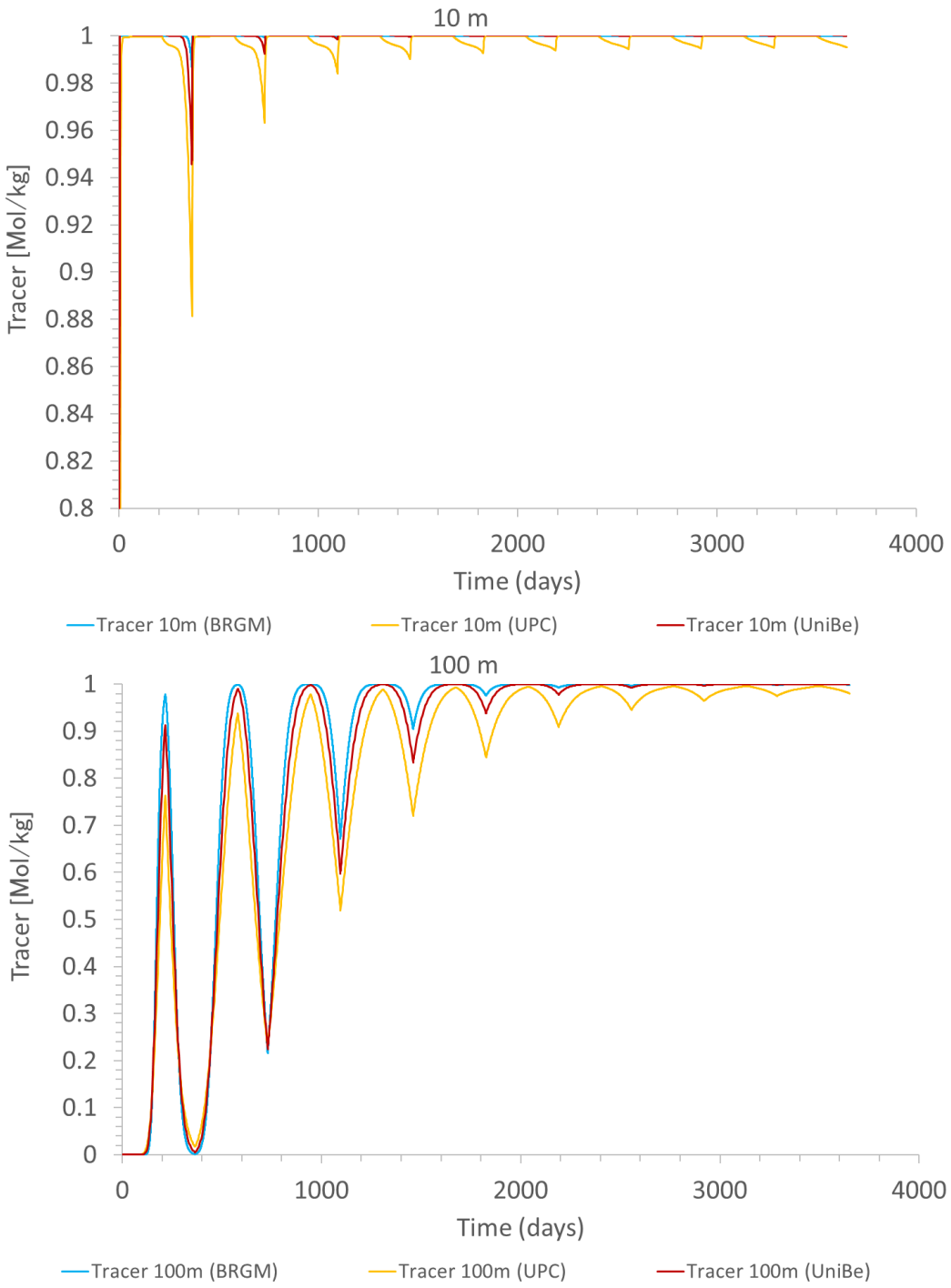


**Figure 4-12: Breakthrough of the injected tracer 10 and 100 m from the well (upper and lower panel, respectively). There tends to be a slight underprediction of the tracer concentration by UPC which is most likely related to a higher dispersivity used in their simulation (i.e. more tracer mass is dispersed into the low permeability clay unit).**

The output shows regular fluctuations of pressure according to injection/extraction cycles. The amplitude of these pressure fluctuations decreases with increasing distance from the injection well (Figure 4-10).
The temperature increases and decreases upon injection and extraction, respectively. While in close vicinity to the well the temperature of the solid aquifer material acquires and maintains the injection temperature rapidly, the temperature increases gradually over time away from the well (e.g. at 50 m, Figure 4-11),

indicating a slow heating of the reservoir rock. The thermal effect of injecting warm water becomes weaker with increasing distance from the injection site – there is no change in temperature at a distance of 100 m from the well.

In contrast, the breakthrough of the tracer concentration is faster than that of the temperature (it scales with the porosity). At observation points close to the well, the injection concentration is attained rapidly and maintained during the operation period. At a distance of 100 m, the first extraction cycle strongly impacts on the tracer concentration as dilute water is drawn from the more distal part of the aquifer (note, the observation point at 100 m is not affected by the influx of water across the right-hand boundary). With each injection cycle the tracer migrates deeper into the aquifer as the volume of injected water exceeds that of the extracted water. As a consequence, at r = 100 m dilution during extraction cylces only ceases after several cycles (Figure 4-12).

### 4.5.3 Component problem 3

Component problem 3 includes the full reaction network. Injection temperature is 90 °C. The composition of the injected water is that copouted in component problem 1 (Table 4-6). Note the minerals amorphous silica and $CO_2$,s are omitted here as these minerals are specifically used to assess processes in the heat exchanger which are addressed in component problem 4.

The results show that mineral reactions are strongest in the injection zone near the well (Figure 4-13 – Figure 4-15). During injection, primary feldspar, quartz and clinochlore are altered to an assemblage of clay minerals dominated by muscovite and minor kaolinite and smectites (Figure 4-13). Upon extraction, the same primary minerals dissolve as during injection but at lower rates as rock-buffered water is drawn from the distal parts of the aquifer towards the well. The alteration phases are the same as during injection but dominated by Ca-smectite (Figure 4-14).

The carbonate minerals, calcite in particular, show a higher reactivity than the silicate minerals (Figure 4-15). Strong calcite and minor dolomite dissolution is followed by calcite and dolomite precipitation during injection and extraction, respectively. This alternation between dissolution and precipitation also takes places at greater distance from the well, only at lower rates and with a certain time lag, as the injection zone (i.e. the zone affected by thermal or compositional changes due to injection) grows in size (Figure 4-15). Figure 4-16 shows that after a transient period with strong fluctuations of the reaction rates, the amplitude of the fluctuations decreases, indicating a slow change to more stable, rock buffered conditions. The same decrease in amplitude over time can be seen in variations of the pH following alternating injection and extraction cycles (Figure 4-17).

Comparing the behavior of calcite and quartz shows that quartz only dissolves but never precipitates (Figure 4-18). Quartz dissolution occurs as the aquifer heats up and quartz solubility increases. At a distance of 50 m away from the well, the onset of quartz dissolution lags behind the response of calcite. One possible explanation for this is that the reactivity of calcite is primarily controlled by changes in the composition of the water moving back and forth, whereas the response of quartz is controlled by local temperature changes as the thermal plume also moves back in forth. The lag in the response of quartz compared to calcite follows from the slower spread of the thermal front compared to the solute front.

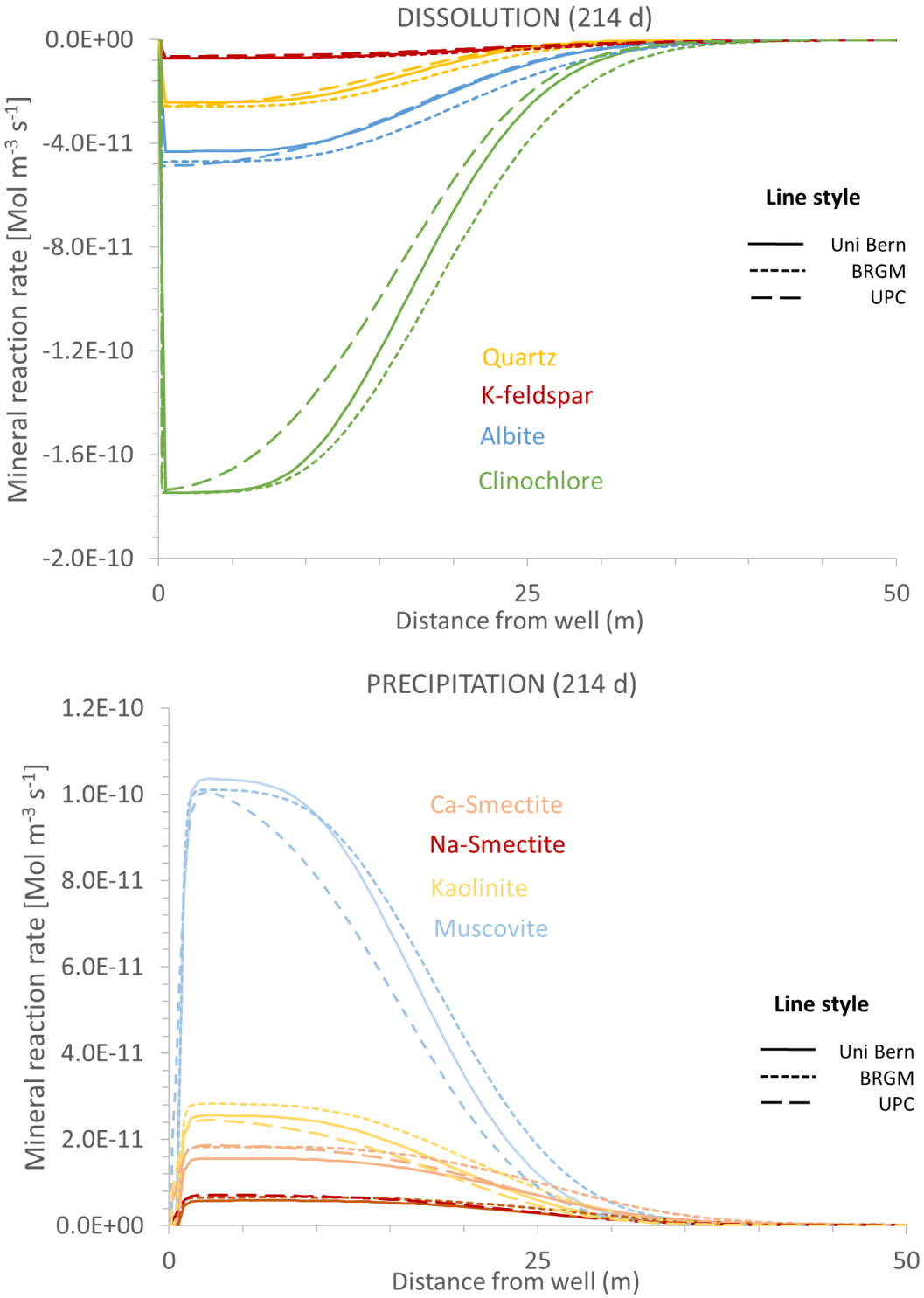


**Figure 4-13: Spatial profiles of dissolution- and precipitation rates of alumino-silicates after 214 days, that is at the end of first the first injection cycle. Chlorite, feldspars and quartz dissolve and form an assemblage of clay minerals including muscovite, smectites and kaolinite.**

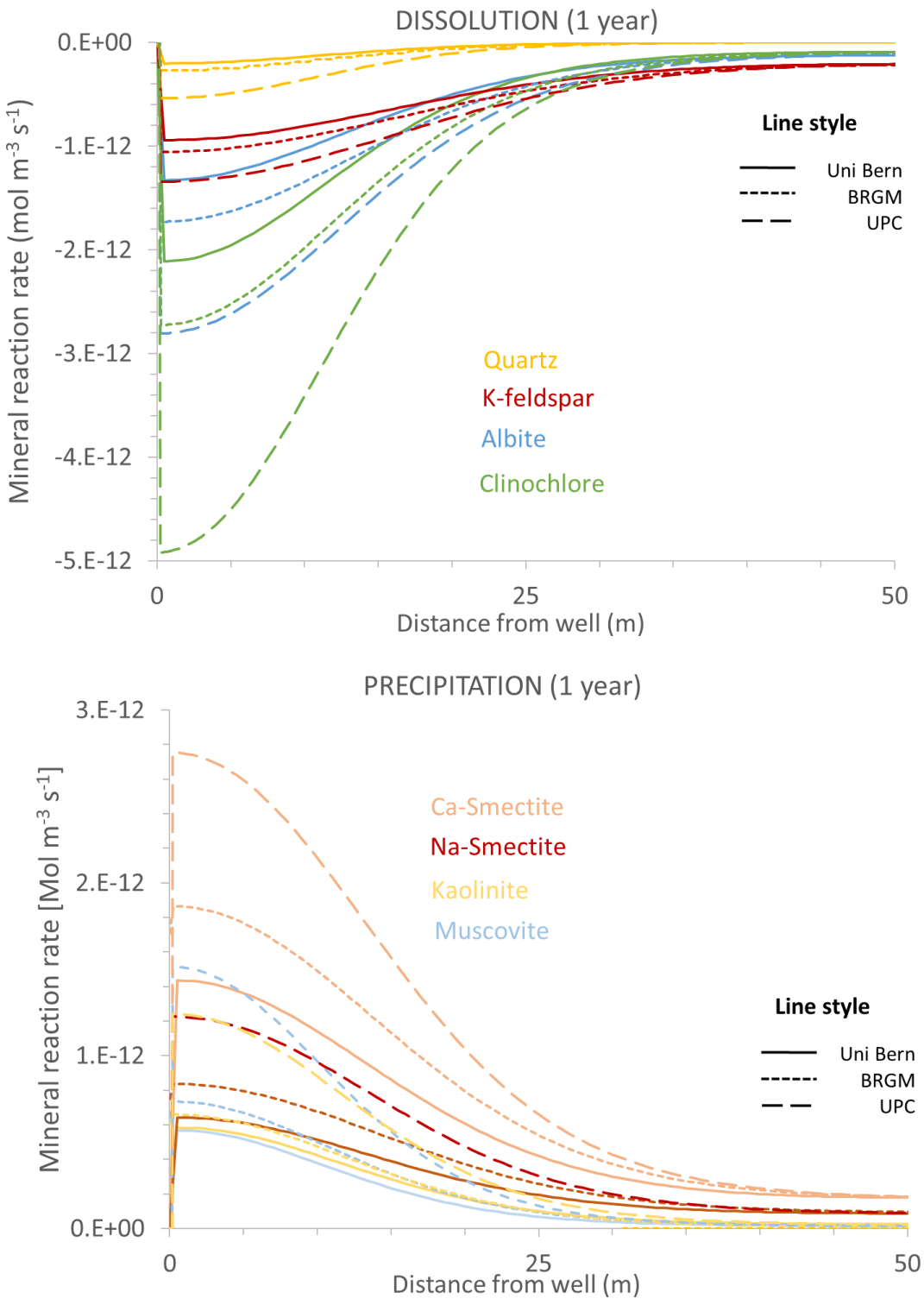


**Figure 4-14: Spatial profiles of reaction rates of alumino-silicates after 363 days (end of first injection cycle, upper panel) and 363 days (end of first extraction cycle, lower panel. Profiles show that Ca-smectite is the main alteration phase near the well, other clay minerals occur in smaller amounts.**

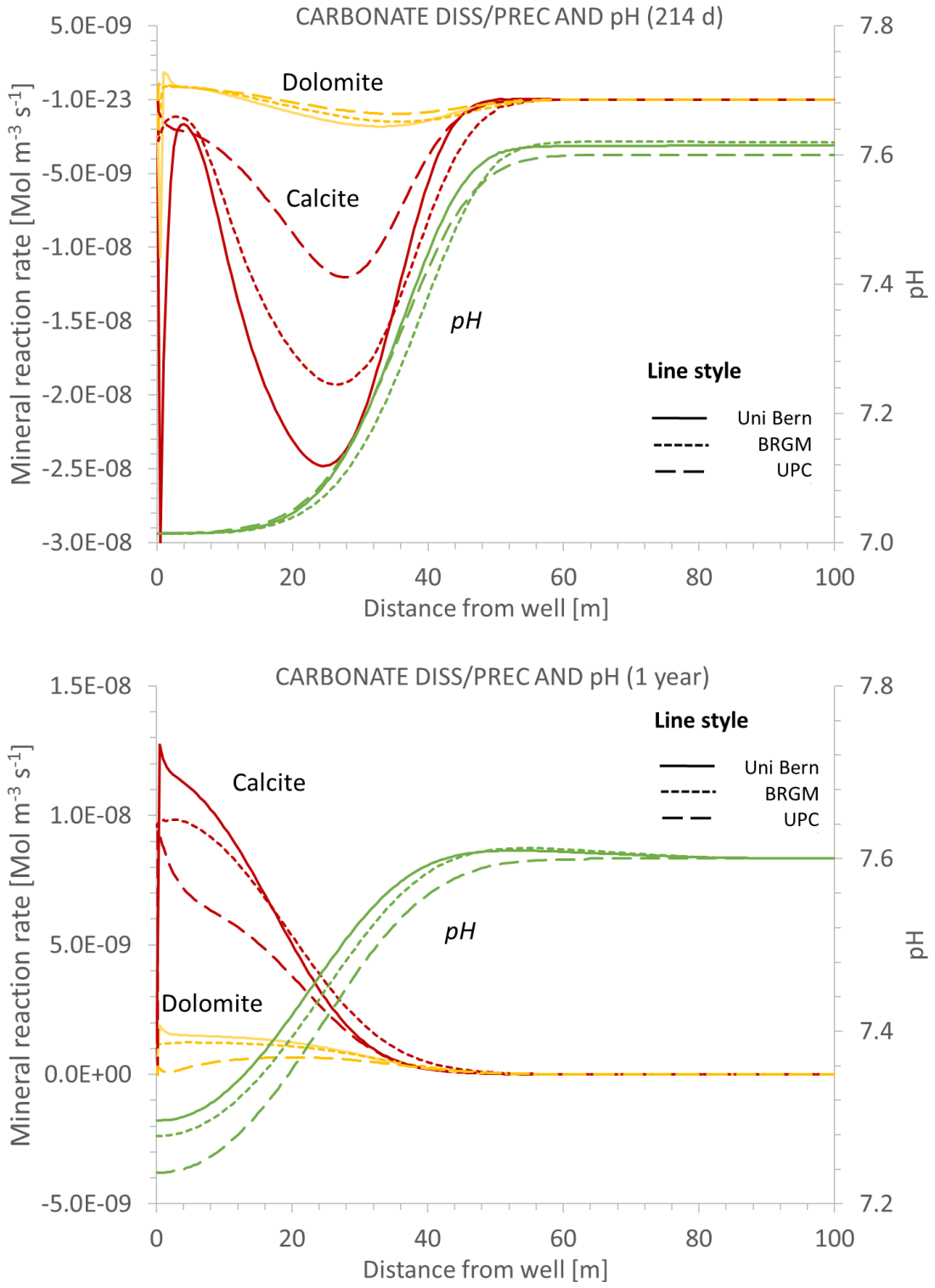


**Figure 4-15: Spatial profiles of carbonate mineral reaction rates after 214 days (end of first injection cycle , upper panel) and 363 days (end of first extraction cycle, lower panel. Both carbonate minerals dissolve and precipitate upon injection and extraction, respectively. The radius of influence after the first year of operation is about 50 m.**

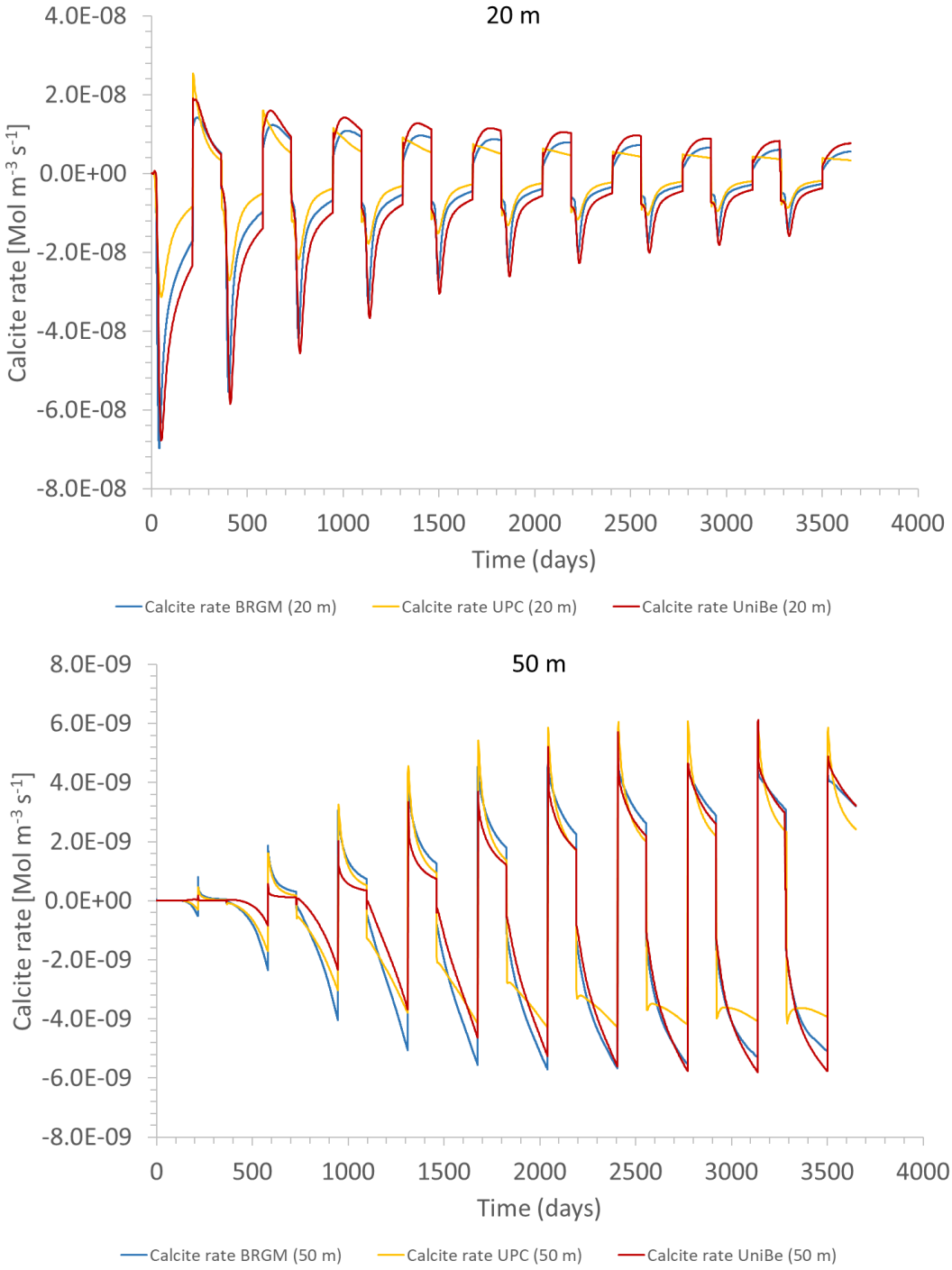


**Figure 4-16: The alternating dissolution and precipitation of calcite upon injection and extraction as in Figure 4-15 can be seen here as well.. There is a tendency that over time the reactivity of calcite decreases as indicated by a decreasing amplitude of the rate fluctuations in the upper panel. This is consistent a slow transition to more stable chemical conditions in the aquifer.**

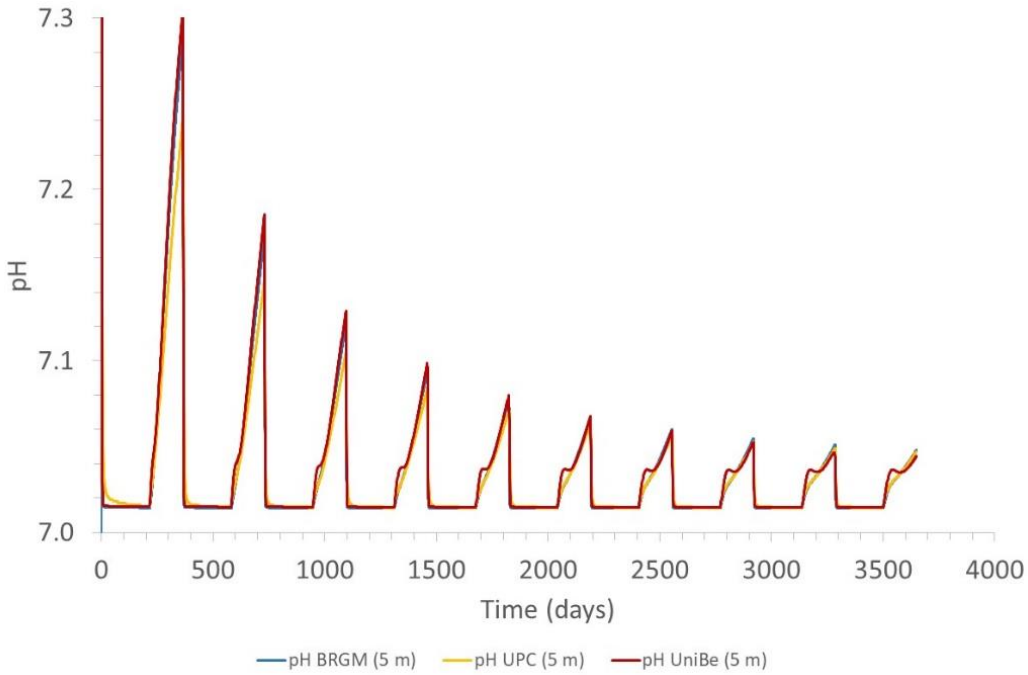


**Figure 4-17: The evolution of the pH 5 m from the well. The initial, undisturbed sandstone is set to 7.6. This value changes rapidly in the injection zone close to the well consistent with a lower pH of the injected water. The initial pH of the groundwater can be maintained (with slight fluctuations) in the distal parts of the domain (e.g. at 100 m, not shown) where conditions are more rock buffered.**

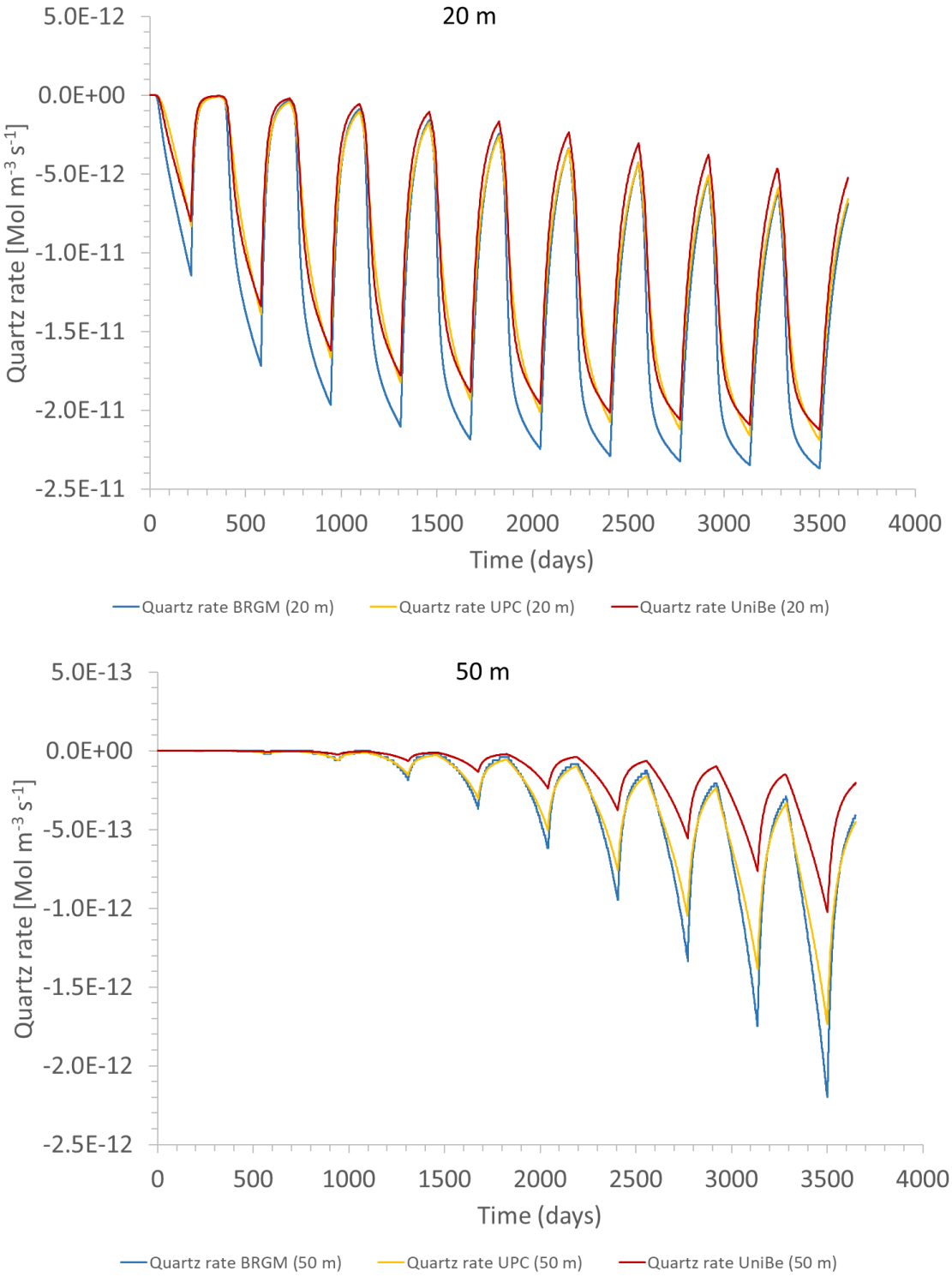


**Figure 4-18: Oscillations of the quartz reaction rate in response to injection and etraction cycles. Unlike calcite in Figure 4-16 quartz dissolves in the injection zone as the groundwater heats up. The ups and downs of the dissolution rate correlate with temperature: stronger dissolution occurs during injection. There is a notable time lag in the onset of quartz dissolution at 50 m away from the well compared to the early response of calcite in Figure 4-16, pointing to a temperature control of the solubility of quartz and a fluid composition control of the solubility of calcite .**

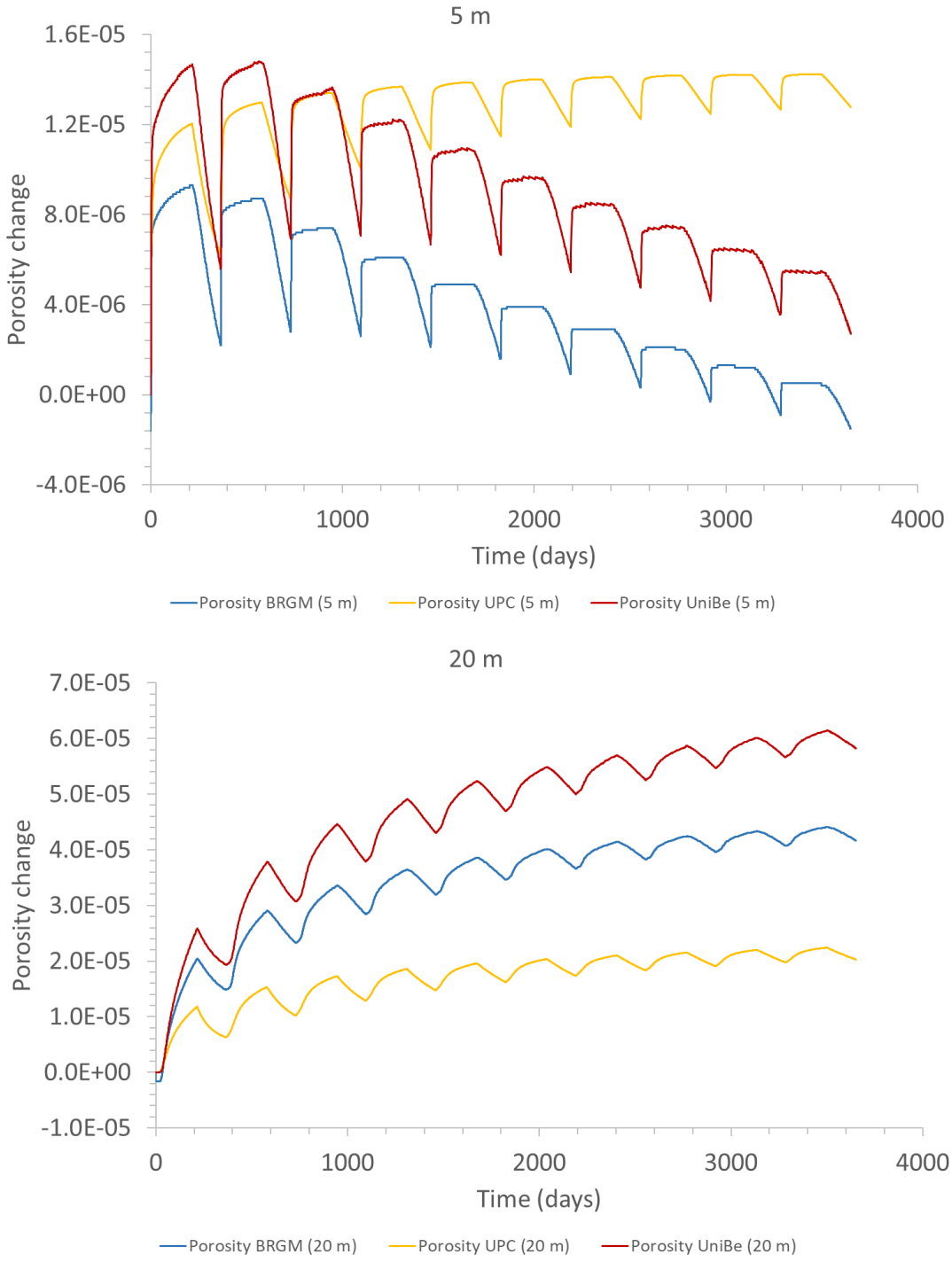


**Figure 4-19: Comparison of the porosity evolution at different observation points along the aquifer. Most of the porosity changes are due to carbonate dissolution/precipitation reactions. The porosity changes are very small and not likely to affect aquifer permeability and hence the operation of the system.**

The simulation of component problem 3 is a complex interplay of flow to and from the well combined with heat and solute transport and chemical reactions. Mineral reaction rates in particular are sensitive indicators

of the local thermal and chemical conditions as these depend on the water composition via the affinity term and the temperature via the Arrhenius term in the rate equation.

Given the complexity of the system the overall agreement between the results from different simulators is very good. The codes predict the same set of reactions and for most minerals the computed reaction rates show a good match. There tends to be a stronger discrepancy between the peaks or the maxima/minima in the timeseries, but there is no systematic over- or underprediction of one particular codes. There is a tendency for RETRASO (UPC) to deviate somewhat from the results computed with PFLOTRAN (UniBe) and MARTHE_PHREEQC (BRGM). The main reason for this is that RETRASO does not include the rates as an output parameter. The rates shown in the figures were calculated during post-processing based on the change in mineral quantities over a 30 day period.

The porosity changes in Figure 4-19 represent the cumulative effect of minerals dissolving and precipitating on the pore volume available for flow. At 5 m the porosity trend of UPC differs markedly from that of the other groups. UniBe and BRGM compute a decrease in porosity genratio over time. BRGM predicts a porosity reduction after 10 years. In contrast, UPC computes a general porosity increase with time. However, given that the mineral volumes dissolving and precipitating and thus the ensuing porosity changes are extremely small (there are 4 orders of magnitude between the total porosity and the computed porosity changes), these differences are tolerable. The conclusion drawn from these simulation results is that there are no hydraulic implications of injection/extraction in the aquifer and there is no expected loss of injectivity.

### 4.5.4 Component problem 4

Component problem 4 focuses on processes that take place in the borehole or in the heat exchanger on the surface. However, given the simplified geometry of the model it is necessary to resort to modifications of the model that mimic the fate of the thermal water during ascent and in the heat exchanger rather than trace the fluid's pathway in every detail. The implementation of this problem requires properties of the borehole to change to an injection well and to a heat exchanger at the beginning of each injection and extraction cycle, respectively, as discussed above.

We focus on processes in the immediate vicinity of the well which includes the interior of the well and the well screen. This region is internally discretized into 5 cells and is used to mimic in a condensed way the effect of temperature on the fluid composition during its ascend and descend through the borehole and processes in the heat exchanger. In this region the injected/extracted water undergoes temperature changes leading to mineral precipitation reactions (i.e. scaling). Mineral precipitation is turned off during injection but turned on during extraction. There are no primary minerals and mineral scales are prevented from redissolution. Mineral precipitation rates are increased to compensate for the short distance over which these processes take place.

The innermost observation point "BH" is located within the well and thus the region whose properties alternate between an injection well and a heat exchanger during injection and extraction cycles, respectively. The temperature time series illustrates this behavior (Figure 4-20): there is an instantaneous switch between 90 °C and 20 °C representing injection and extraction, respectively and constant temperature conditions inbetween. The temperature of 20 °C is assumed to be the lowest temperature of the water attained in the heat exchanger.

Outside the well, the temperature evolution is controlled by heat transport away and towards the well. The observation point "SN" is located in the "screen", outside the borehole/heat exchanger. The screen represents an interval in which the groundwater is no longer buffered by the rock. The composition of the water adjusts to local temperature conditions. Mineral precipitation is allowed only during extraction, all precipitated minerals are not allowed to dissolve and thus accumulate over time. These conditions are analogue to a water entering a well.

This benchmark problem was only carried out by the Uni Bern and BRGM teams, using PFLOTRAN and MARTHE-PHREEQC, respectively. The default version of PFLOTRAN can simulate changing material properties but the source code was adjusted to prevent mineral scales from redissolving, that is to simulate

the accumulation of mineral scales during extraction. In MARTHE-PHREEQC, these changing chemical conditions were programmed within the PHREEQC input file via BASIC scripts.

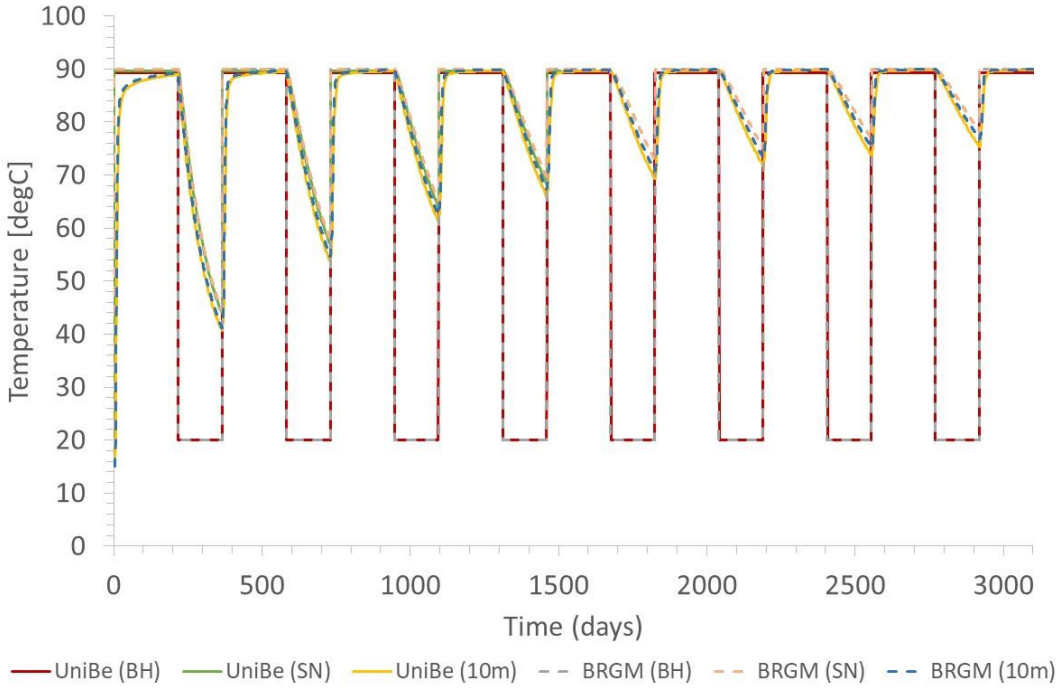


**Figure 4-20: Temperature evolution in the well/heat exchanger at the "well screen".**

The alteration of feldspars to clay minerals increases the pore water at pH values of around 7.6 in the distal parts of the aquifer (e.g. r = 100 m, Figure 4-21) and to somewhat lower values near the well. There is only a small difference between the pH in the borehole where the water is unbuffered by the rock and the pH at 10 m within the aquifer (Figure 4-21).

The most important minerals precipitating as scales are calcite (Figure 4-22) and dolomite (Figure 4-23). Significant dolomite precipiation occurs only during the first cycle. Both mineral precipitate rapidly and are confined to the "screen". No carbonate precipitation occurs within the well or the heat exchanger. Calcite precipitates because the water entering the screen is slightly oversaturated with respect to calcite. This is a consequence of high flow velocities in combination with a relatively small reactive surface areas of calcite in the aquifer leading to (relatively) slow dissolution and precipitation rates in the aquifer. Because the precipitation rates are a factor 100 higher in the screen, instantaneous calcite equilibrium is attained as calcite precipitates.

In addition to carbonate minerals, several clay minerals such as smectite muscobite or kaolinite precipitate in small quantities (Figure 4-23). Alumino-silicate mineals show a prograde solubility with temperature and hence precipitate upon cooling. This is why these clay mineral precipitate in the screen as well as in the heat exchanger. The precipitation of clay minerals leads to an increase in pH but no carbonate minerals precipitate as a consequence because the effect of pH is overwhelmed by the steep drop in temperature in the heat exchanger which increases the solubility of carbonate minerals. It is also interesting to note that quartz does not reach saturation. Quartz or amorphous silica do not attain saturation. There are two reason for this: 1) the extracted water was undersaturated with respect to quartz when it entered the well (recall that the water is heated as it moves from deeper parts of the aquifer towards the well) and 2) the precipitation of clay minerals consumes $SiO_2$,aq such that it is no longer available for the formation of quartz.

The computed amounts of minerals in the model screen and the borehole (i.e. the well and heat exchanger, respectively), need to scaled up to the dimension of the real system to have any quantitative meaning. That is, model volume fractions have to be scaled by the extraction rates and bulk volumes in the real system. For instance, a volume fraction of 2.5e-3 of calcite in the screen over a period of 10 years (Figure 4-22) implies

an absolute volume of about 0.052 $m^3$ for the 7.5 m vertical section. Scaled over the entire thickness of the real system (350 m) this yields a total volume of scales of 0.24 $m^3$ per year for the real system.

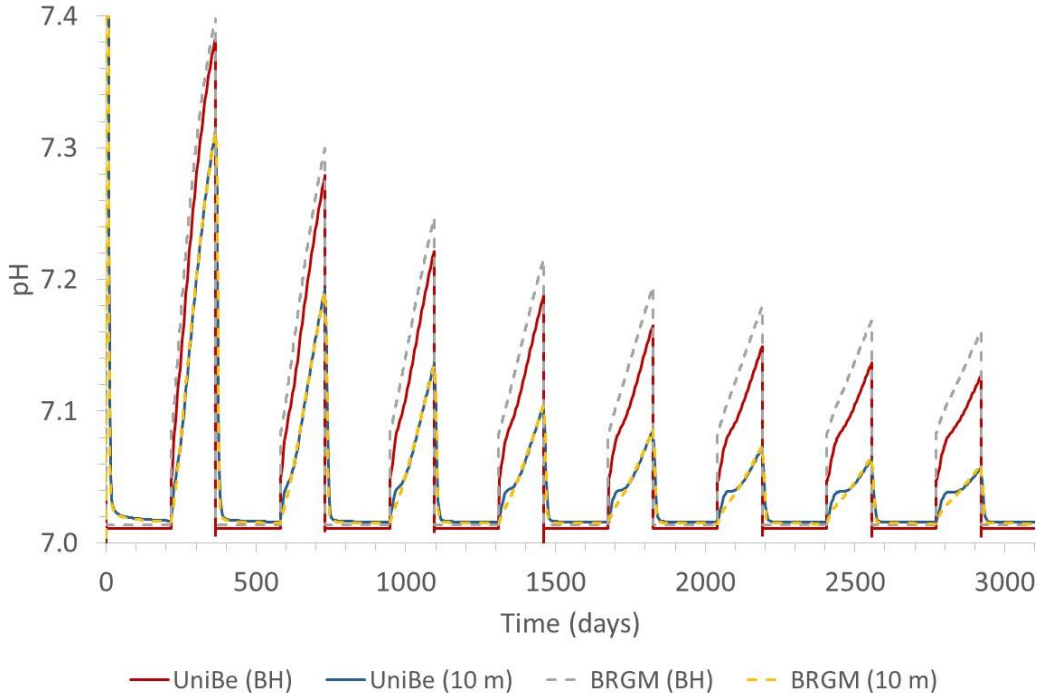


**Figure 4-21: The pH shows fluctuations between that of the injected water (pH = 7.01) and that of the rock buffered water during injection and extraction cycles respectively. The pH increases slightly in the "heat exchanger" as clay minerals precipitate.**

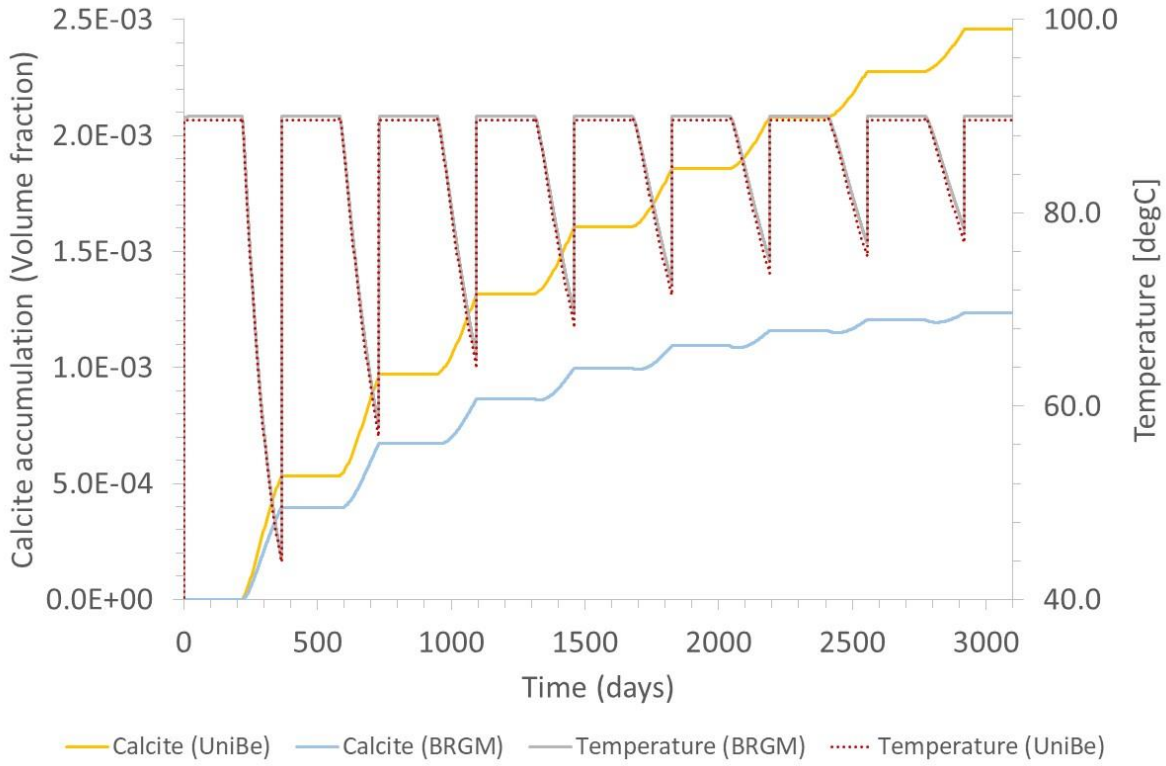


**Figure 4-22: Accumulation of calcite and the temperature evolution in the screen "SN".**

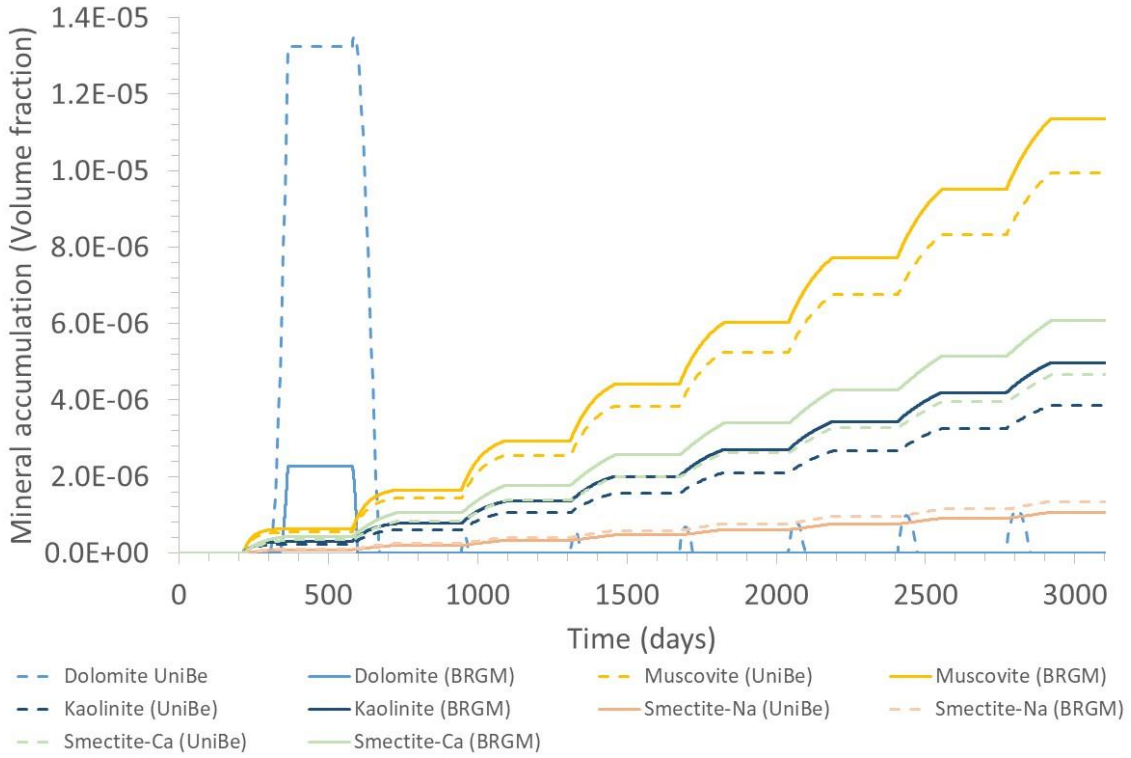


**Figure 4-23: Accumulation of minerals other than calcite in the screen ("SN").**

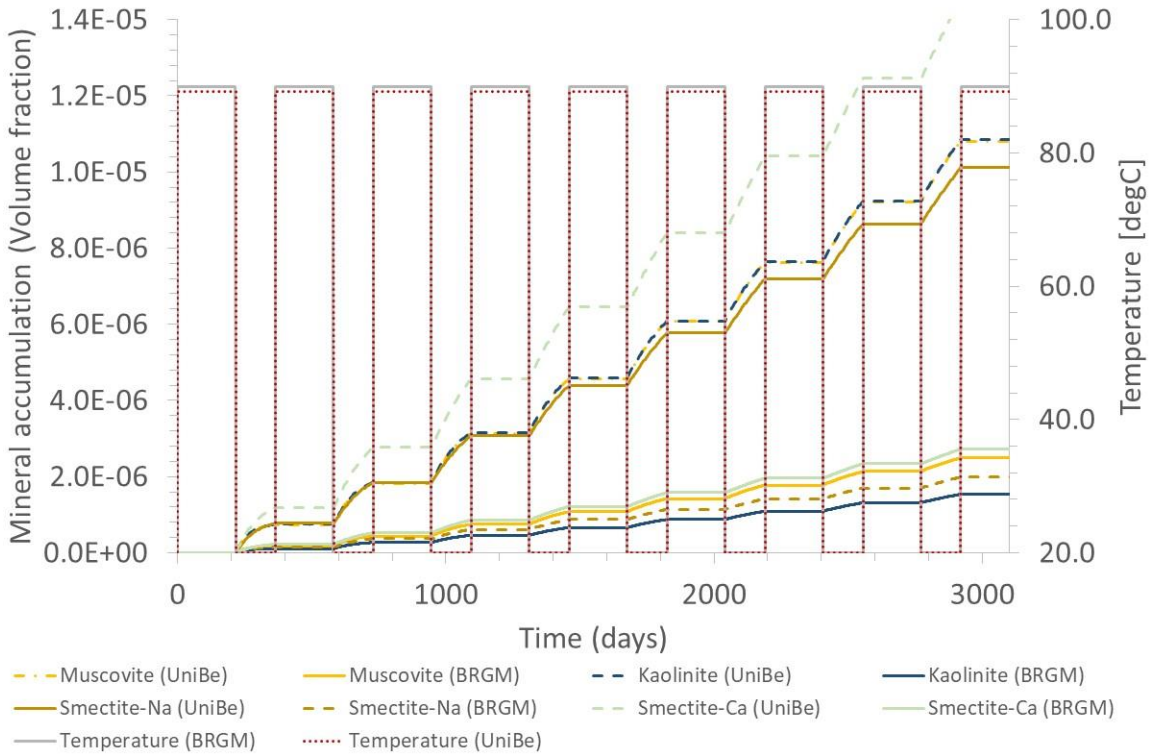


**Figure 4-24: Minerals forming in the heat exchanger. Consistent with their solubility behavior w.r.t temperature, alumino-silicate minerals are the dominant scale forming mineral phases.**

Both codes show good agreement in this very complex problem. The predicted amount of calcite and dolomite accumulating in the screen is about a factor two higher in the PFLOTRAN calculations. If this amount is upscaled to the size of the real system, the potential amount of calcite precipitating in the installation could be significant. In contrast, the clay mineral show excellent agreement in their cumulative amounts. This is remarkable given the similar thermodynamic properties of these clay minerals. The good agreement seen in the screen in absent in the heat exchanger. Although in terms of mineral quantities, there is reasonable agreement, the predicted composition of the mineral assemblage (i.e. the proportion of individual minerals in the scales) differs greatly. The reason for this discrepancy is the strong temperature drop from 90 °C to 20 °C in combination with similar thermodynamic properties of the secondary clay minerals. The latter leads to a situation where only small differences in the precipitation rate of individual minerals can lead to different mineral assemblages and/or different mineral amounts in these assemblages. Both codes predict the precipitation of clay mineral in the heat exchanger and they predict similar total quantities of these minerals. If the purpose of the simulation is to accurately predict the exact amounts of individual clay phases in the assemblage, the results shown in Figure 4-24 suggest that this cannot be resolved unambiguously with this kind of simple model. More constraints of PT conditions along the fluid pathway are needed to track the fate of the thermal water more accurately. Perhaps then the agreement would improve.

In none of the simulation cases did $CO_2$ degassing occur. The assumed reservoir $pCO_2$ and the pressure drop are too low to cause any significant changes in the $CO_2$,g saturation. In none of the simulation did amorphous silica precipitate.

## 4.6 Conclusions

Three modelling teams (UPC, BRGM, University of Bern) using three different reactive transport codes (Retraso, Marthe/Phreeqc, Pflotran) carried out a suite of benchmark problems of increasing complexity. The purpose of this benchmark was to test the codes capabilities and performance, to compare the accuracy of the simulations, find and remedy potential errors and strengthen confidence and reliability of the results. The benchmark project involved the following component benchmarks:

1) a simple 1D reactive transport problem using constant flow velocity and temperature fields
2) an axisymmetric model with heat and tracer transport
3) an axisymmetric model with heat and reactive transport
4) an axisymmetric model with changing material properties mimicking the heat exchanger

The last component benchmark was carried out by BRGM and UniBern only. All simulations were performed with the default versions of the code. Component problem 4 required minor modifications of the PFLOTRAN source code to prevent mineral scales in the borehole (or heat exchanger) from redissolving. All codes show very good agreement between the results. The agreement could have been further improved by iteratively tracking down the reason for those (minor) differences but because of the good agreement no effort was made to do so. Mineral reaction rates which are controlled by the effect of local temperature and fluid composition generally fall within a range of a factor two. The results obtained from PFLOTRAN and MARTHE-PHREEQC tend to show a slightly better agreement than those from REACTORO. The reason for this is that the rates from REACTORO were not part of the simulation output but were obtained during post-processing. The differences between codes are greatest where rates change rapidly and exhibit maxima or minima. Differences were also more prominent in the prediction of porosity changes which represent the cumulative effect of mineral rates. Again, the results from UPC deviated somewhat stronger from those of the other teams. However, computed porosity changes are very small so that these deviations are also small in absolute terms. Component problem 4 was challenging in that several secondary clay phases exhibiting similar thermodynamic properties were predicited to form in the heat exchanger when the temperature of the thermal water drops very rapidly from 90 °C to 20 °C.

Although UniBe and BRGM predicted the same mineral assemblage, the proportion of individual mineral phases differed substantially. Nevertheless, this is still a good result given the simplified representation of the heat exchanger. The agreement could have been improved, if the pathway of the fluid up the well and through the heat exchanger had been modelled in greater detail.

The code comparison did not include a rigorous performance benchmark because this would require the same computation platform as reference. Hence the following assessment is only qualitative. Component benchmark 2 was carried out within less than 1 hour by UPC and UniBern and 2.41 hours by BRGM. Component benchmark 3 was simulated within hours by UPC and UniBern and 27.6 days by BRGM. Component benchmark 4 was simulated within hours by UniBern and 36.5 days by BRGM. The main reason for the much longer simulation time of MARTHE-PHREEQC was the very small time steps used in the simulations to fulfill the Courant criterium. The Courant crierium has to be obeyed because of the sequential coupling and explicit time stepping scheme of the code. It should also be noted that PFLOTRAN is the only code that has been parallelized. The simluation times mentioned above refer to single processor times. Running component problems 3 and 4 with PFLOTRAN with four processors in parallel shortens the simulation time to 50 and 45 minutes, respectively.

Aside from differences in performance, all codes have shown that they are capable of simulating flow, transport and chemical reaction processes in ATES systems. There are advantages and disadvantages to each code. Both MARTHE and PHREEQC are well known, powerful stand-alone TH and C codes, respectively. Coupling the two provides a powerful tool that allows one to use the great flexibility of PHREEQC by writing BASIC scripts within the input file. However, the sequential coupling between the codes makes simulations slow. PFLOTRAN in contrast is built for high performance and can be run in parallel and laptops or supercomputers. PFLOTRAN is still under development but has a rapidly growing user base. PFLOTRAN does not have the same flexibility as PHREEQC in terms of customizing the input file but since PFLOTRAN is open-source it is possible to customize the source code. This however, requires some experience with the code and in code programming. RETRASO is a finite element code and as such offers great flexibility in terms of discretizing complex geometries. To obtain stable results using RETRASO, the Peclet condition has to be obeyed (dispersivity > 0.5*size of element). Thus simulating the high Peclet number conditions in this benchmark problem, the dispersivity had to be increased to 1 m to obtain stable results.

# 5 Task conclusions

The Heatstore Task 2.3 benchmarking initiative essentially showed that all participating teams are able to simulate basic TH and THC processes related to thermal underground storage using their code of choice. In the majority of cases, the results were reasonably similar. Some benchmark sub-tests involved more complexity, such as the modelling of a fault in radial coordinates and transient material properties, and could not be completed by all participants due to individual software and/or software-support/know-how limitations. Notably, “limitation” may not necessarily imply a lack of functionality, but could also be related to very basic properties of the native implemented formulation, such as the choice of spatial and time discretization schemes for solving the associated partial differential equations. For example, the choice between a finite element or a finite volume spatial discretization approach already determines certain strengths and weaknesses of a simulator. In essentially every benchmark case there are trade-offs between different approaches used by the different simulators. Ultimately, the choice typically depends on the problem that needs to be solved and if it is within the range of applicability of a particular simulator.

In particular, this benchmarking exercise revealed that the capability of simulating mechanical (M) processes is underrepresented within the HEATSTORE community. Although THM simulations were carried out by the modelling group at UPC, they unfortunately did not materialize into a proper benchmark as no other team was able to participate in it. Thus, strengthening the THM capabilities in the HEATSTORE code portfolio would be useful reflection out of this deliverable. The final simulation goal should ultimately remain in the coupling of hydrology and heat transport with geochemistry and mechanics (THMC).

# 6 References

Baghapour, B. et al., 2018. A pressure drop study for packed bed adsorption thermal energy storage. Applied Thermal Engineering, Volume 138, pp. 731-739.

Basha, H. A., 1999. Multidimensional linearized nonsteady infiltration with prescribed boundary conditions at the soil surface, , 35(1), 75–83.. Water Resour. Res., 35(1), pp. 75-83.

Battistelli A, Calore C, Preuss K (1997) The simulator TOUGH2/EWASG for modeling geothermal reservoirs with brines and non-condensible gas.Geothermics,26, 437–64

Beck, J. L., 1972. Convection in a Box of Porous Material Saturated with Fluid. The Physics of Fluids, Volume 15, p. 1377.

Carman, P., 1937. Fluid flow through granular beds. Transactions, Institution of Chemical Engineers, London, Volume 15, pp. 150-166.

Chen, Z., 2007. Reservoir Simulation: Mathematical Techniques in Oil Recovery (CBMS-NSF Regional Conference Series in Applied Mathematics). Philadelphia PA, USA: Society for Industrial and Applied Mathematics.

Edwards, A.L., 1972. “TRUMP: A Computer Program for Transient and Steady State Temperature Distributions in Multidimensional Systems.” National Technical Information Service, National Bureau of Standards, Springfield, VA.

Enos, P. & Sawatsky, L. H., 1981. Pore networks in Holocene carbonate sediments. J. of Sedimentary Petrology, 51(3), pp. 961-985.

Florio, 2017. Interacting convection modes in a saturated porous medium of nearly square.

Hammond, G.E., P. C. Lichtner, C. Lu, and R.T. Mills (2012) Pflotran: Reactive flow and transport code for use on laptops to leadership-class supercomputers. In Fan Zhang, G.T. Yeh, and Jack C. Parker, editors, Groundwater Reactive Transport Models, pages 141--159. Bentham Science Publishers, Sharjah, UAE, 2012

Horton, C. W. & Rogers, F. T., 1945. Convection currents in a porous medium. J. Appl. Phys., Volume 16, p. 367–370.

Johnson, J.W., Oelkers, E.H., Helgeson, H.C., 1992. SUPCRT92: a software package for calculating the standard molal thermodynamic properties of minerals, gases, aqueous species and reactions from 1 to 5000 bar and 0 to 1000□C, Comput. Geosci., v. 18, 899-947

Jung, Y., Shu Heng Pau, G., Finsterle, S., Doughty, C., 2018. TOUGH3 User’s Guide, , Energy Geosciences Division, Lawrence Berkerley National Laboratory, University of California, Bekerley, California 97720, January 2018.

Kozeny, J., 1927. Ueber kapillare Leitung des Wassers im Boden. Sitzungsber Akad. Wiss., Volume 136 (2a), pp. 271-306.

Lachenbruch, A.H., and J.H. Sass (1977) Heat flow in the United States and the thermal regime of the crust, in The Earth's Crust, Geophys. Monagr. Ser., vol. 20, edited by J.G. Heacock, pp. 626-675, AGU, Washington, D.C., 1977

Lapwood, E. R., 1948. Convection of a fluid in a porous medium. Proc. Camb. Phil. Soc., Volume 44, p. 508–521.

Lasaga, A.C., Soler, J.M., Ganor, J., Burch,T.E., Nagy, K.L., 1994. Chemical weathering rate laws and global geochemical cycles, Geochim. Cosmochim. Acta, 58, 2361–2386.

Lichtner, P.C. and G. E. Hammond (2012) Using high performance computing to understand roles of labile and nonlabile uranium(vi) on hanford 300 area plume longevity. VADOSE ZONE JOURNAL, 11(2), MAY 2012.

McCabe, W. L., Smith, J. C. & Harriot, P., 2005. Unit Operations of Chemical Engineering. 7 ed. New York: McGraw-Hill.

Narasimhan, T.N. and P.A. Witherspoon, 1976. “An Integrated Finite Differ-ence Method for Analyzing Fluid Flow in Porous Media.” Water Resour. Res., v. 12, p. 57-64

Palandri, J., Kharaka, Y.K., 2004. A compilation of rate parameters of water–mineral interaction kinetics for application to geochemical modeling. US Geol. Surv. Open File Report 2004-1068. 64 pp.

Parkhurst, C.A.J. Appelo (2013) Description of input and examples for PHREEQC version 3 - A computer program for speciation, batch-reaction, one-dimensional transport, and inverse geochemical calculations, in, U.S. Geological Survey Techniques and Methods, , book 6, chap. A43, 497 p., available only at http://pubs.usgs.gov/tm/06/a43.

Philips, J. R., 1969. Theory of Infiltration. Adv. Hydrosci., Volume 5, p. 215–296.

Phillips SL, Igbene A, Fair JA, Ozbek H, Tavana M (1981) ATechnical Databook for Geothermal Energy Utilization. LawrenceBerkeley Laboratory Report 12810.

Pullan, A. J., 1990. The quasilinear approximation for unsaturated porous media flow. Water Resour. Res., 26(6), p. 1219–1234.

Réveillère, A., Hamm, V., Cordier, E., Goblet, P., Lesueur, H., 2013. Geothermal contribution to the energy mix of a heating network when using Aquifer Thermal Energy Storage: Modeling and application to the Paris basin. Geothermics 47 (2013) 69-79

Saaltink, M.W., Batlle, F., Ayora, C., Carrera, J., Olivella, S. RETRASO, a code for modeling reactive transport in saturated and unsaturated porous media. Geologica Acta, 2004, 2(3), 235-251.

Singh, C., Tathgir, R. & Muralidhar, K. (. 4. 5., 2006. Experimental validation of heat transfer models for flow through a porous medium. Heat Mass Transfer, Volume 43, pp. 55-72.

Slotte, A. & Berg, C. F., 2017. Lecture notes in well-testing, Trondheim, Norway: Department of Geoscience and Petroleum NTNU.

Smith, L., and D.S. Chapman, On the thermal effects of groundwater flow, 1, Regional scale systems, J. Geophys. Res., 88, 593-608, 1983.

Steefel, C.I., C. A. J. Appelo, B. Arora, D. Jacques, T. Kalbacher, O. Kolditz, V. Lagneau, P. C. Lichtner, K. U. Mayer, J. C. L. Meeussen, S. Molins, D. Moulton, H. Shao · J. Simunek, N. Spycher, S. B. Yabusaki, G. T. Yeh (2015) Reactive transport codes for subsurface environmental simulation, Comput. Geosci., 19, 445–478

Thiéry D. (2004), Discretization and equations solved in the code MARTHE. Technical note, NT EAU 2004/10.

Thiéry D. (2012), Presentation of the MARTHE 7.5 code developed by BRGM. Technical note, NT EAU 2012/03. Updated October 2018.

Thiéry D. (2015), 3D modeling of mass transport and heat transfer with the code MARTHE – version 7.5 (updated in August 2019). Report BRGM/RP-64765-FR

Thiéry D (2015), Modélisation 3D du Transport Réactif avec le code de calcul MARTHE v7.5 couplé aux modules géochimiques de PHREEQC, in: R. BRGM/RP-65010-FR (Ed.), Orléans, France, 2015, pp. 164, available at http://infoterre.brgm.fr/rapports/RP-65010-FR.pdf .

Tseng, P.-H. & Lee, T.-C., 1998. Numerical evaluation of exponential integral: Theis well function approximation. Journal of Hydrology, 205(1-2), pp. 38-51.

Vinsome, P.K.W. and J. Westerveld (1980), A simple method for predicting cap and base rock heat losses in thermal reservoir simulators, J. Can. Pet. Tech., July-Sept., 19080, pp 87-90

Zimmerman, R. & S. Bodvarsson, G., 1996. Hydraulic conductivity of rock fractures. Transport in Porous Media, Volume 23, pp. 1-30.

# 7 Appendices

## 7.1 Appendix A: TH Benchmark 1 - Analytical solution

Maple code to reproduce the analytical solution

```
> restart;
```

```
> Digits:=50;
  Q:=0.001:# m^3/s no density needed in equation.
  h:=200:
  k:=10^(-15):
  mu:=0.00074:
  Pres:=1e6:
  phi:=0.2:
  ct:=4.45*10^(-10):
  kappa:=k/(mu*ct*phi):
```

$$Digits := 50 \tag{1}$$

```
> p1:=(r,t)-> Pres - Q/(4*Pi*k*h/mu)*Ei(-r^2/(4*kappa*t));
```

$$p1 := (r, t) \rightarrow Pres - \frac{1}{4}\,\frac{Q\,\mu\,\mathrm{Ei}\left(-\frac{1}{4}\,\frac{r^2}{\kappa\,t}\right)}{\pi\,k\,h} \tag{2}$$

```
> pp1:=plot(p1(r,1e8),r=0..1000);
```

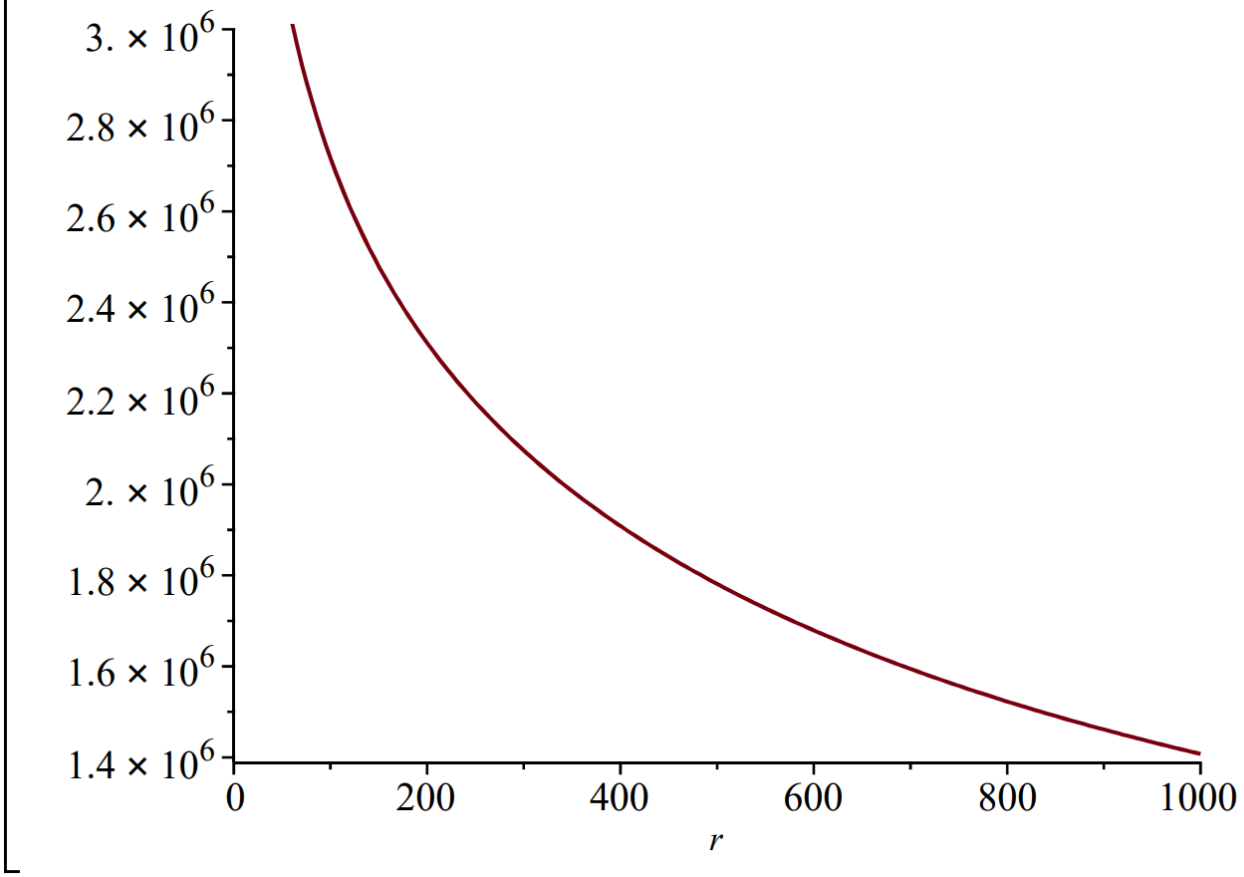

## 7.2 Appendix B: TH Benchmark 1 - Monitored output locations

The output locations for monitoring the two basic problems presented in section 2.5 (test3) are presented in the following table:

| x [m] (Glass spheres) | x [m] (Steel spheres) |
|---|---|
| 0.0 | 0.0 |
| 0.319 | 0.145 |
| 0.638 | 0.290 |

The following table provides a list of output times (i.e. for test3) necessary for error calculation. These values can be observed at the leftmost column in the file `test3_Glass_EXAMPLE.txt`.

| Output times [s] |
|---|
| 0 |
| 14.40068 |
| 28.80137 |
| 43.20205 |
| 57.60274 |
| 72.00342 |
| 86.40411 |
| 100.8048 |
| 115.2055 |
| 129.6062 |
| 144.0068 |
| 158.4075 |
| 172.8082 |
| 187.2089 |
| 201.6096 |
| 216.0103 |
| 230.411 |

## 7.3 Appendix C: TH Benchmark 1 - Test 1 results

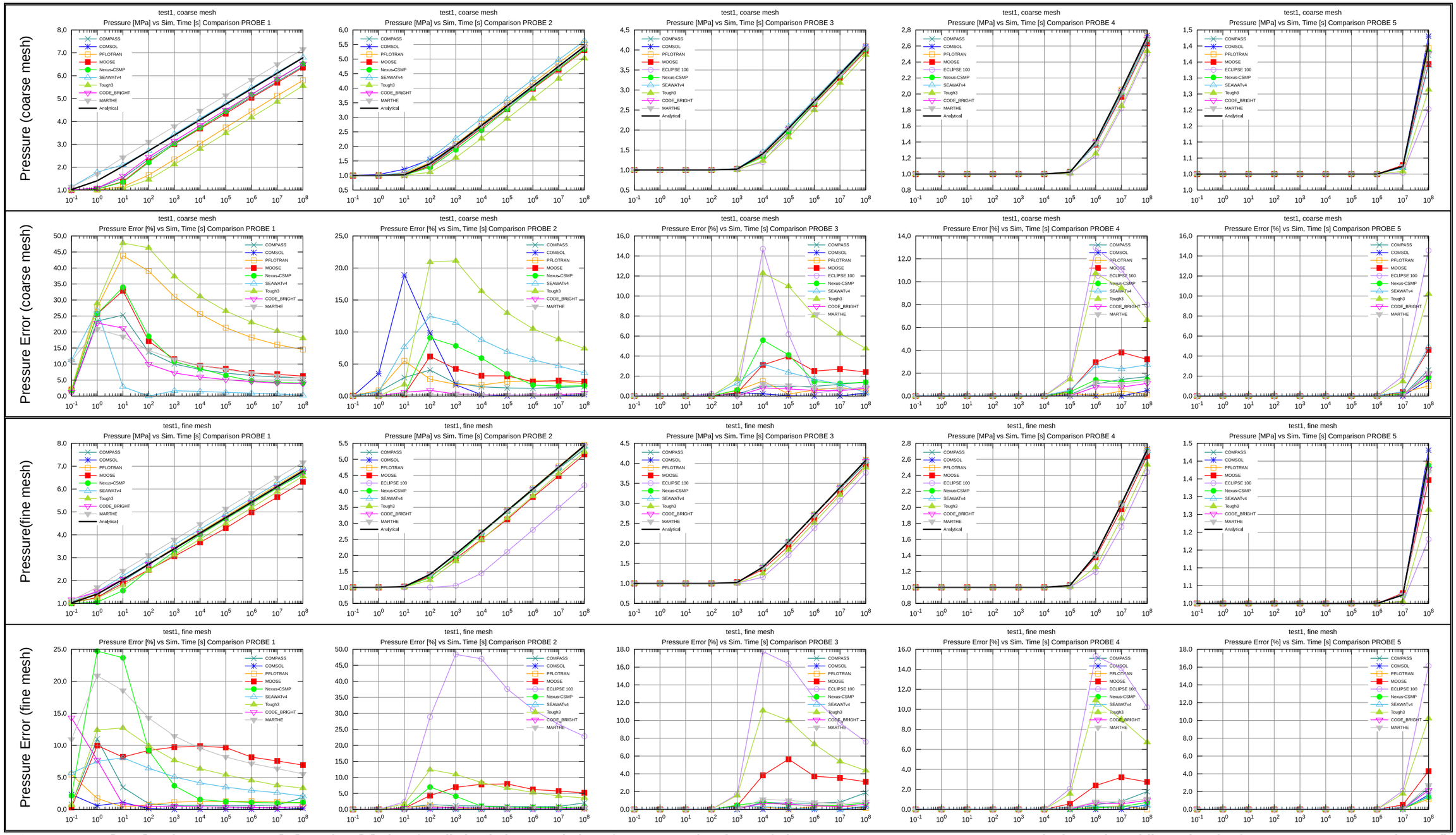


**Figure C-1: Pressure [MPa] and Pressure Error [%] vs Time [s] plots for all simulations carried out for test1. Each column of plots represents measurements at a particular probe, while each pair of rows represents a mesh type (i.e. coarse or fine).**

## 7.4 Appendix D: TH Benchmark 1 - Test 2 results

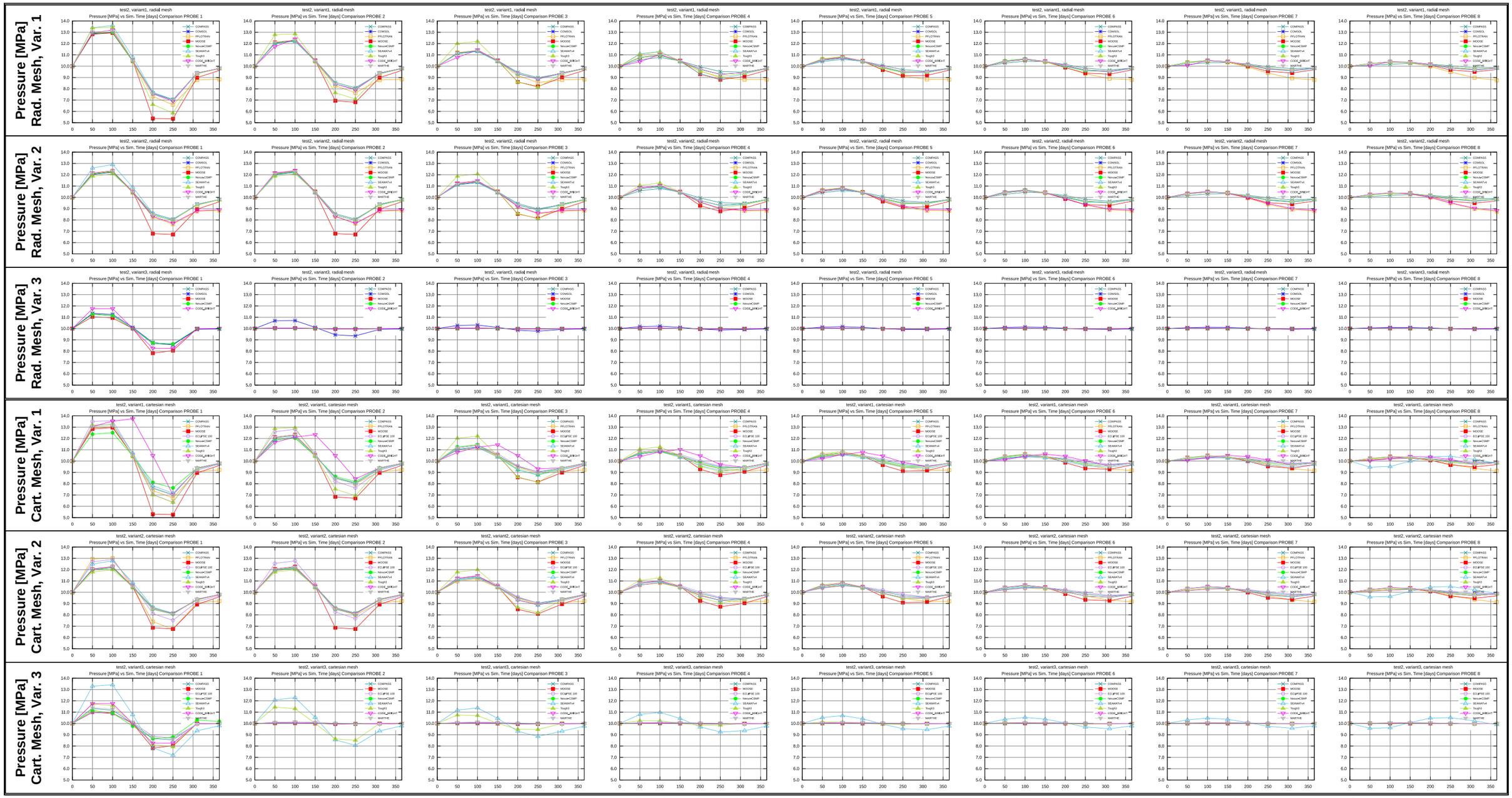


**Figure D-1: Pressure [MPa] vs Time [days] for all simulations carried out for test2. Each column of plots represents measurements at a particular probe (i.e. 8 probes In total), while each triplet of rows represents a mesh type (i.e. radial or cartesian).**

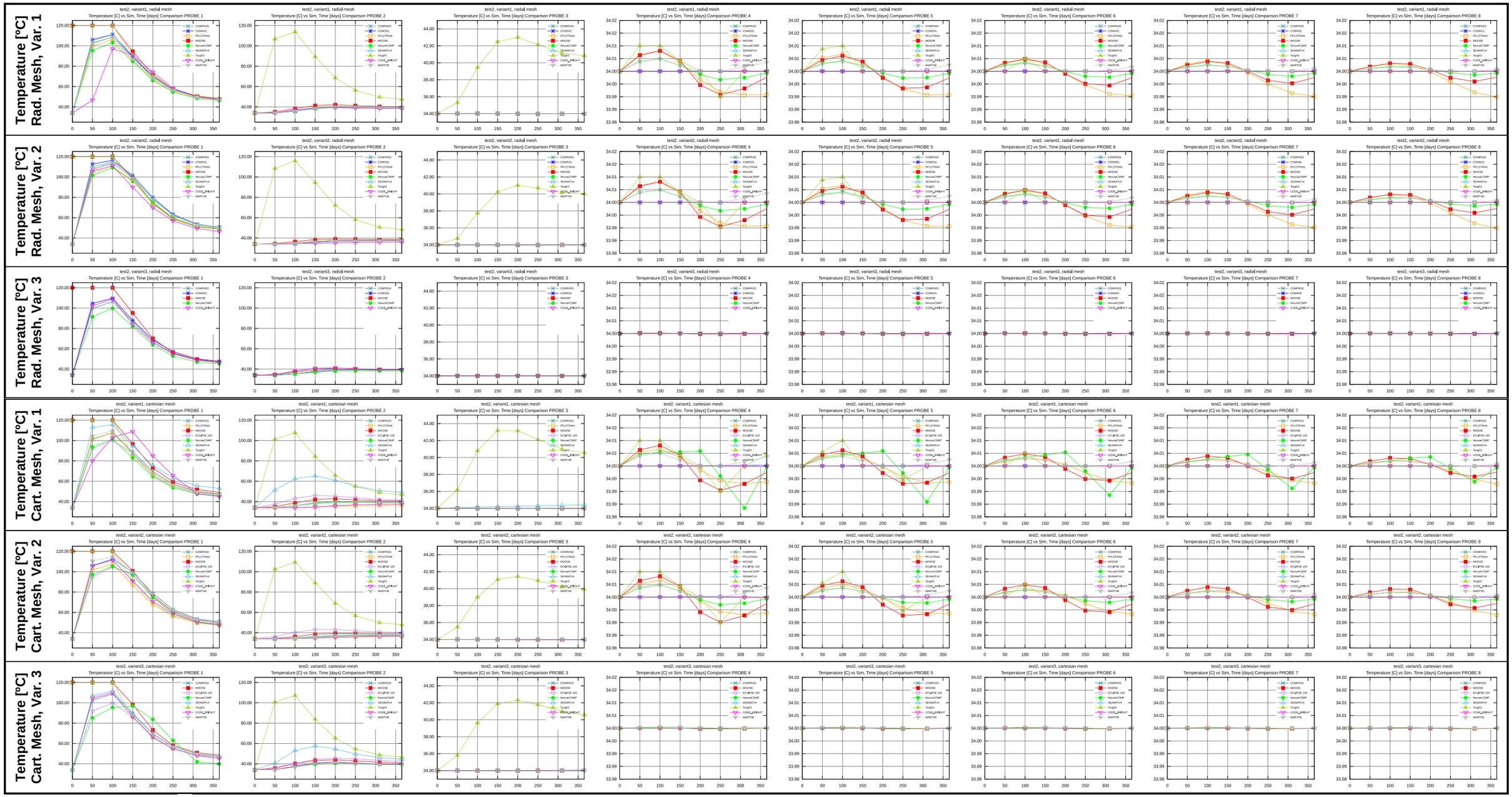


**Figure D-2: Temperature [ºC] vs Time [days] for all simulations carried out for test2. Each column of plots represents measurements at a particular probe (i.e. 8 probes In total), while each triplet of rows represents a mesh type (i.e. radial or cartesian).**

## 7.5 Appendix E: TH Benchmark 1 - Test 4 results

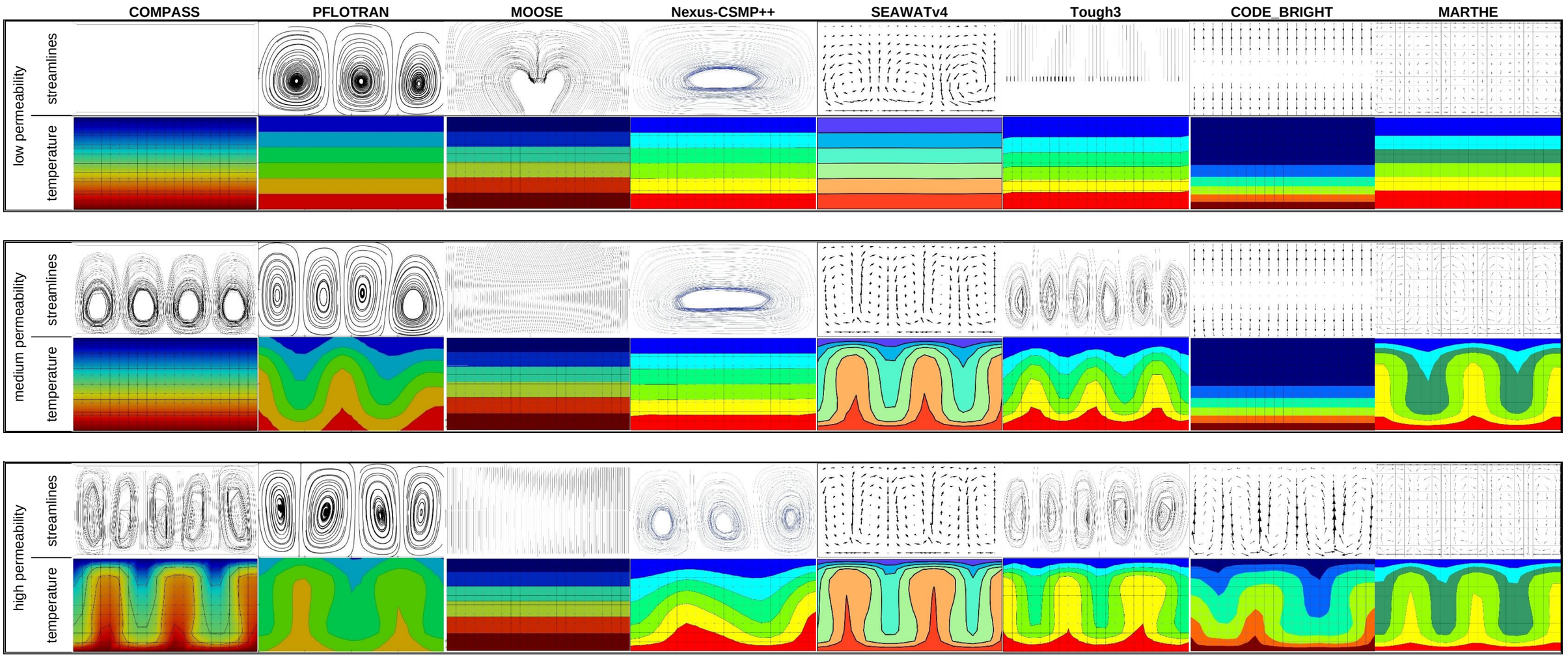


**Figure E-1: Cross-simulator comparison depicting coarse-mesh snapshots of streamlines and temperature contours at time level t=10 [yrs].**

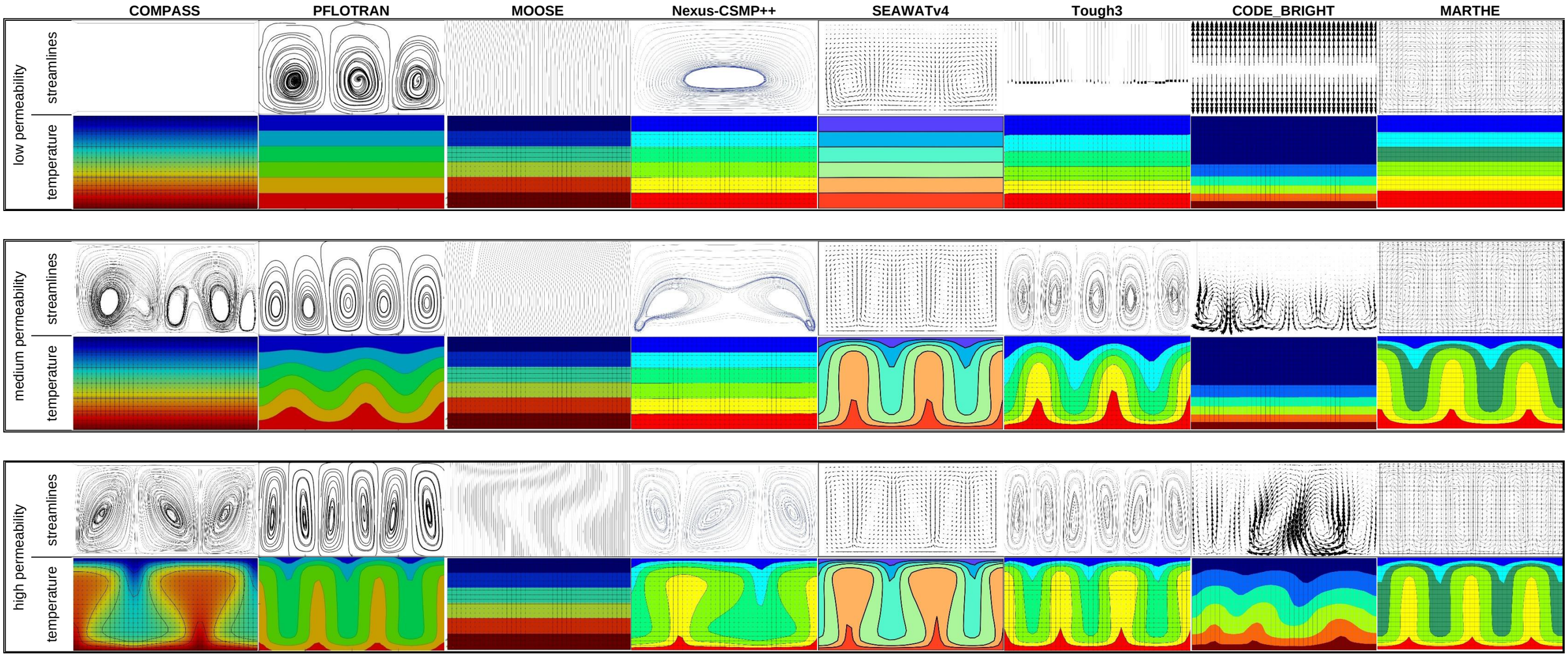


**Figure E-2: Cross-simulator comparison depicting fine-mesh snapshots of streamlines and temperature contours at time level t=10 [yrs].**

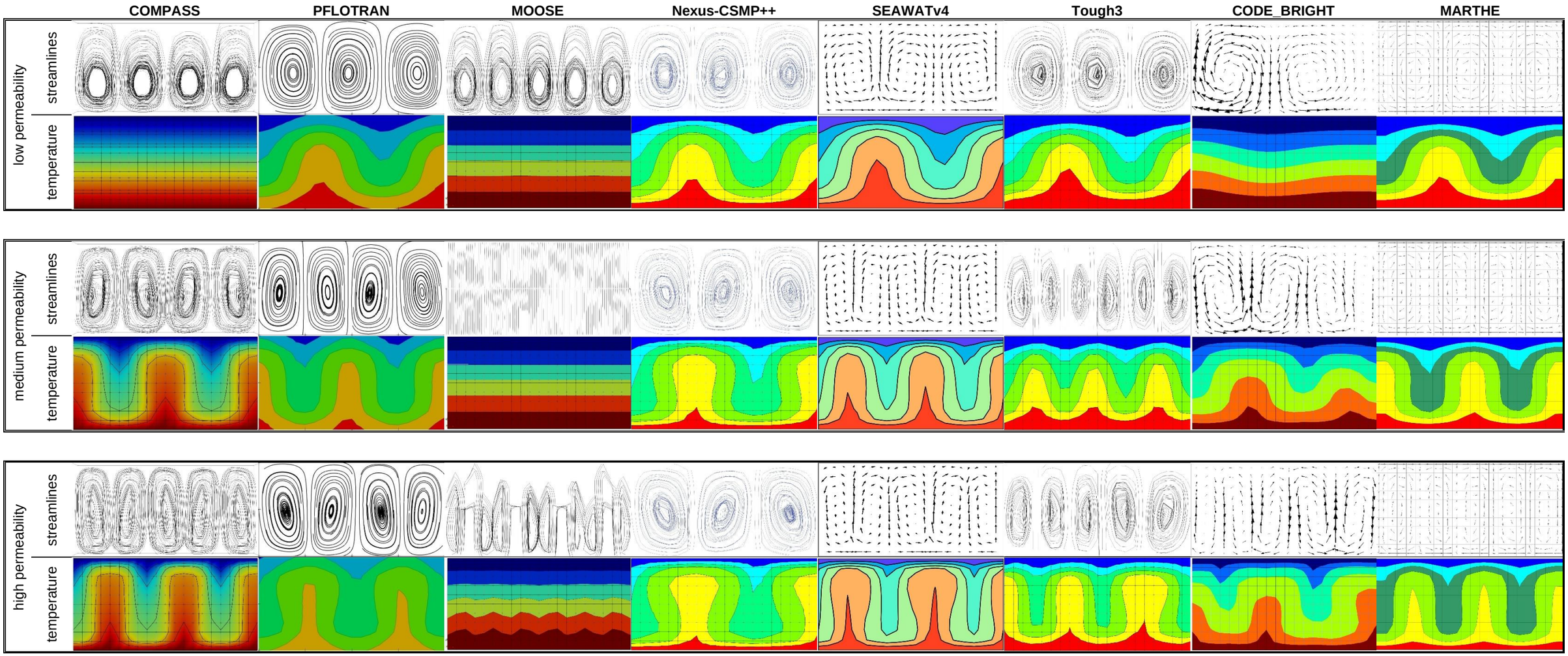


**Figure E-3: Cross-simulator comparison depicting coarse-mesh snapshots of streamlines and temperature contours at time level t=100 [yrs].**

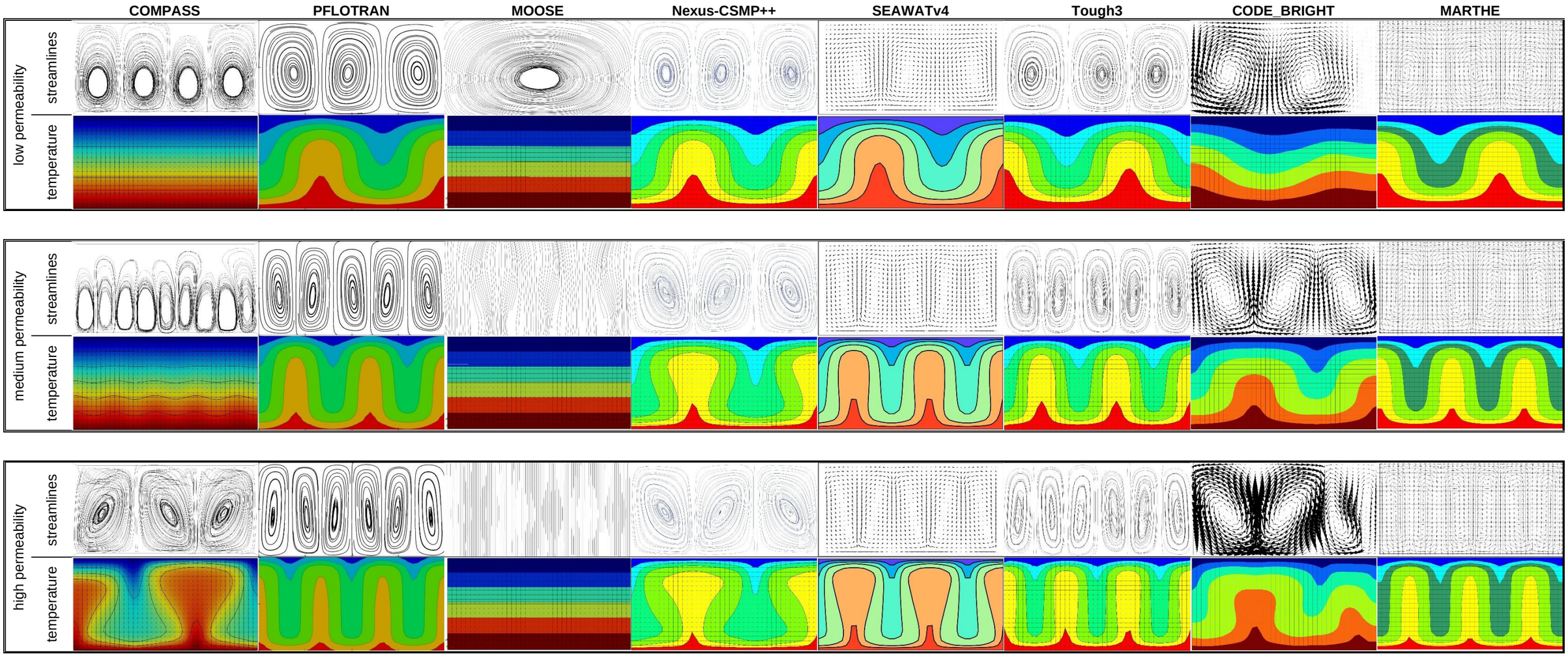


**Figure E-4: Cross-simulator comparison depicting fine-mesh snapshots of streamlines and temperature contours at time level t=100 [yrs].**

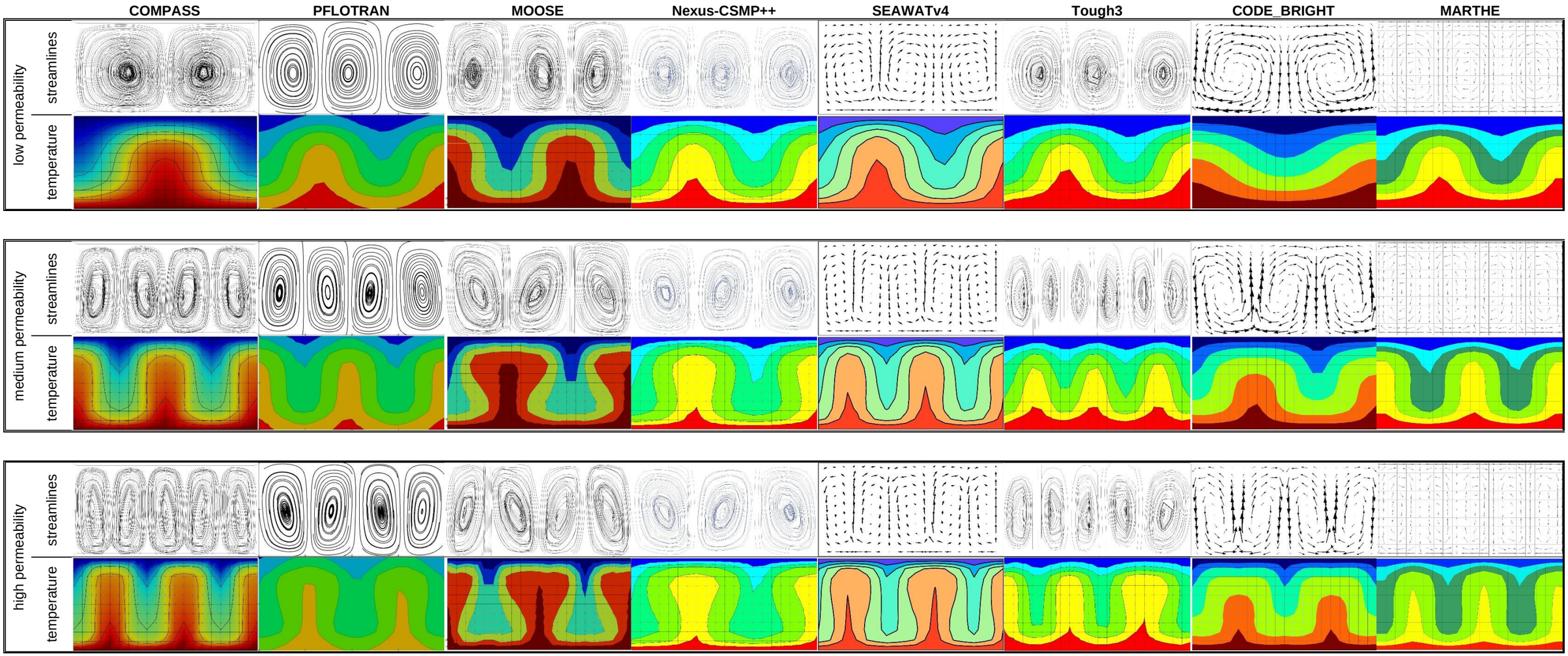


**Figure E-5: Cross-simulator comparison depicting coarse-mesh snapshots of streamlines and temperature contours at time level t=1000 [yrs].**

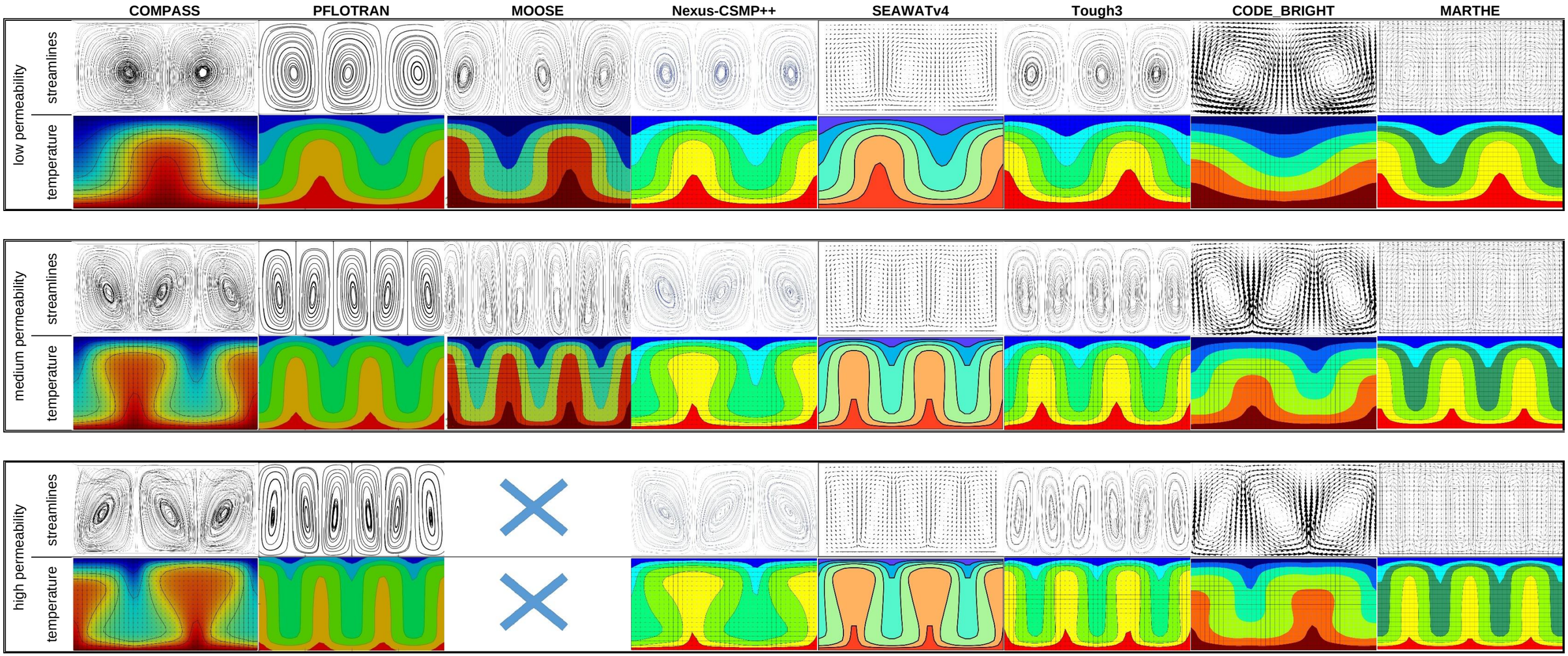


**Figure E-6: Cross-simulator comparison depicting fine-mesh snapshots of streamlines and temperature contours at time level t=1000 [yrs].**

## 7.6 Appendix F: THC Benchmark - Thermodynamic properties of species, minerals and gases

Compilation of reactions, the reaction stoichiometry and the equilibrium constants (logK) of these reactions at discrete temperatures used in the THC benchmark calculations. Equilibrium constants for intermediate temperatures were interpolated.

| **Temperature points** | | **0. 25. 60. 100. 150. 200. 250. 300.** |
|---|---|---|
| **Aqueous complexes** | | |
| CO2(aq)-45bar | 1.0000 'H2O' 1.0000 'H+' 1.0000 'HCO3-' | -6.558 -6.324 -6.249 -6.370 -6.706 -7.183 -7.783 -8.5280 |
| CO3---45bar | -1.0000 'H+' 1.0000 'HCO3-' | 10.601 10.306 10.108 10.061 10.179 10.447 10.866 11.4638 |
| CaCO3(aq)-45bar | -1.0000 'H+' 1.0000 'Ca++' 1.0000 'HCO3-' | 7.49 6.985 6.439 5.962 5.485 5.057 4.59 3.9118 |
| CaCl+ | 1.0000 'Ca++' 1.0000 'Cl-' | 0.6729 0.6956 0.5886 0.3566 -0.0399 -0.5332 -1.1352 -1.9071 |
| CaCl2(aq) | 1.0000 'Ca++' 2.0000 'Cl-' | 0.4520 0.6436 0.6288 0.3811 -0.1593 -0.9109 -1.8952 -3.2351 |
| CaSO4(aq) | 1.0000 'Ca++' 1.0000 'SO4--' | -2.0713 -2.1111 -2.2647 -2.5111 -2.9101 -3.4328 -4.1424 -5.1853 |
| KCl(aq) | 1.0000 'Cl-' 1.0000 'K+' | 1.7097 1.4946 1.2163 0.9240 0.5747 0.2148 -0.1957 -0.7347 |
| MgCO3(aq)-45bar | -1.0000 'H+' 1.0000 'HCO3-' 1.0000 'Mg++' | 7.728 7.334 6.915 6.563 6.223 5.913 5.545 4.9530 |
| MgCO3(aq) | -1.0000 'H+' 1.0000 'HCO3-' 1.0000 'Mg++' | 7.7399 7.3499 6.9262 6.5632 6.2045 5.8725 5.4900 4.9530 |
| MgCl+ | 1.0000 'Cl-' 1.0000 'Mg++' | 0.0494 0.1349 0.0548 -0.1820 -0.6068 -1.1389 -1.7843 -2.6016 |
| MgHCO3+-45bar | 1.0000 'HCO3-' 1.0000 'Mg++' | -1.07 -1.03 -1.155 -1.417 -1.844 -2.359 -2.981 -3.8424 |
| MgOH+ | 1.0000 'Mg++' 1.0000 'OH-' | -2.166 -2.210 -2.378 -2.631 -3.001 -3.430 -3.947 -4.625 |
| MgSO4(aq) | 1.0000 'Mg++' 1.0000 'SO4--' | -2.1387 -2.4117 -2.8370 -3.3473 -4.0727 -4.9554 -4.9554 -4.9554 |
| NaCO3- | -1.0000 'H+' 1.0000 'HCO3-' 1.0000 'Na+' | 9.8150 9.8144 10.0745 10.6485 11.5684 12.6320 13.7927 14.9187 |
| NaCl(aq) | 1.0000 'Cl-' 1.0000 'Na+' | 0.8286 0.7770 0.6509 0.4730 0.2140 -0.0933 -0.4778 -1.0125 |
| NaHCO3(aq) | 1.0000 'HCO3-' 1.0000 'Na+' | -0.3734 -0.1541 0.1098 0.4108 0.7926 1.2130 1.2130 1.2130 |
| NaOH(aq) | -1.0000 'H+' 1.0000 'H2O' 1.0000 'Na+' | 15.6450 14.7948 13.8004 12.8848 11.9708 11.2215 10.5573 9.8847 |
| OH- | -1.0000 'H+' 1.0000 'H2O' | 14.9398 13.9951 13.0272 12.2551 11.6308 11.2836 11.1675 11.3002 |
| AlOH++ | -1.0000 'H+' 1.0000 'Al+++' 1.0000 'H2O' | 5.7264 4.9571 4.0033 3.0626 2.0516 1.1673 0.3661 -0.3794 |
| Al(OH)2+ | -2.0000 'H+' 1.0000 'Al+++' 2.0000 'H2O' | 12.1394 10.5945 8.7455 6.9818 5.1460 3.5858 2.2019 0.9295 |
| HSiO3- | -1.0000 'H+' 1.0000 'H2O' 1.0000 'SiO2(aq)' | 10.3231 9.9525 9.4684 9.0844 8.8497 8.8394 9.0224 9.4141 |
| H3SiO4- | -1.0000 'H+' 2.0000 'H2O' 1.0000 'SiO2(aq)' | 10.3231 9.9525 9.4684 9.0844 8.8497 8.8394 9.0224 9.4141 |
| **Gases** | | |
| CO2(g)-45bar | -1.0000 'H2O' 1.0000 'H+' 1.0000 'HCO3-' | -7.679 -7.818 -8.058 -8.361 -8.77 -9.214 -9.719 -10.3393 |
| **Minerals** | | |
| Albite | 4.0000 'H+' 1.0000 'Al+++' 1.0000 'Na+' 2.0000 'H2O' 3.0000 'SiO2(aq)' | 3.2730 2.7645 1.5678 0.2236 -1.2042 -2.3888 -3.4304 -4.4408 |
| Anhydrite | 1.0000 'Ca++' 1.0000 'SO4—' | -4.1043 -4.3064 -4.7587 -5.3851 -6.2741 -7.2829 -8.4644 -9.9598 |
| Calcite-45bar | -1.0000 'H+' 1.0000 'Ca++' 1.0000 'HCO3-' | 2.225 1.872 1.354 0.794 0.119 -0.567 -1.322 -2.2154 |
| Clinochlore-14A | -16.0000 'H+' 2.0000 'Al+++' 3.0000 'SiO2(aq)' 5.0000 'Mg++' 12.0000 'H2O' | 76.7345 67.2391 55.7725 45.1520 34.6423 26.2016 19.0325 12.5384 |
| Dolomite-45bar | -2.0000 'H+' 1.0000 'Ca++' 1.0000 'Mg++' 2.0000 'HCO3-' | 3.46 2.557 1.369 0.131 -1.313 -2.741 -4.288 -6.1006 |
| Gypsum | 1.0000 'Ca++' 1.0000 'SO4--' 2.0000 'H2O' | -4.5331 -4.4823 -4.6094 -4.9035 -5.4299 -6.1266 -7.0386 -8.3003 |
| Illite | -8.0000 'H+' 0.2500 'Mg++' 0.6000 'K+' 2.3000 'Al+++' 3.5000 'SiO2(aq)' 5.0000 'H2O' | 11.3860 9.0260 5.5551 2.0473 -1.5896 -4.6120 -7.2534 -9.7110 |
| K-Feldspar | -4.0000 'H+' 1.0000 'Al+++' 1.0000 'K+' 2.0000 'H2O' 3.0000 'SiO2(aq)' | -0.2168 -0.2753 -0.9610 -1.8555 -2.8681 -3.7528 -4.5737 -5.4136 |
| Kaolinite | -6.0000 'H+' 2.0000 'Al+++' 2.0000 'SiO2(aq)' 5.0000 'H2O' | 9.0182 6.8101 3.8468 0.9541 -2.0187 -4.5022 -6.7083 -8.8022 |
| Muscovite | -10.0000 'H+' 1.0000 'K+' 3.0000 'Al+++' 3.0000 'SiO2(aq)' 6.0000 'H2O' | 17.1295 13.5858 8.8387 4.1918 -0.6018 -4.6169 -8.1836 -11.5635 |
| Quartz | 1.0000 'SiO2(aq)' | -4.6319 -3.9993 -3.4734 -3.0782 -2.7191 -2.4378 -2.2057 -2.0168 |
| SiO2(am) | 1.0000 'SiO2(aq)' | -3.1240 -2.7136 -2.4067 -2.1843 -1.9796 -1.8190 -1.6928 -1.6042 |
| Smectite-Na | -6.12 'H+' 0.29 'Na+' 0.26 'Mg++' 1.77 'Al+++' 3.97 'SiO2(aq)' 4.06 'H2O' | 3.029 0.975 -1.408 -3.587 -5.749 -7.567 -9.567 -11.567 |
| Smectite-Ca | -6.12 'H+' 0.145 'Ca++' 0.26 'Mg++' 1.77 'Al+++' 3.97 'SiO2(aq)' 4.06 'H2O' | 3.134 0.984 -1.515 -3.809 -6.096 -8.025 -10.025 -12.025 |
| CO2(s) | 1.0000 'CO2(aq)-45bar' | -1.097 -1.470 -1.785 -1.970 -1.970 -1.970 -1.970 -1.970 |